University of Amsterdam
VU Vrije Universiteit Amsterdam
Nikhef
LHCb

Physics and Astronomy

Track: Gravitation and Astroparticle Physics Amsterdam

Master Project

60 EC

Branching fraction measurement of $B^0 \to D_s^+ \pi^-$

Author:
Jordy Butter
10527095

Supervisors:
Niels Tuning
Lennaert Bel

Second examiner:
Patrick Decowski

22 June 2018

Abstract

This analysis presents a new measurement of $\mathcal{B}(B^0 \to D_s^+ \pi^-)$, using LHCb data taken in 2011, 2012, 2015, and 2016. The $B^0 \to D_s^+ \pi^-$ decay is described by a single tree diagram and probes the $u \to b$ quark transition $|V_{ub}|$ and non-factorisable effects $|a_{\mathrm{NF}}|$. Measuring the $B^0 \to D_s^+ \pi^-$ signal yield is challenging, due to a large number of background events and the tail of the $B_s^0 \to D_s^- \pi^+$ signal around the $B^0 \to D_s^+ \pi^-$ signal peak. Therefore, the $B_s^0 \to D_s^- \pi^+$ signal shape and the backgrounds are studied in detail. The branching fraction of $B^0 \to D_s^+ \pi^-$ is found to be $\mathcal{B}(B^0 \to D_s^+ \pi^-) = (23.1 \pm 1.7\,(\mathrm{stat}) \pm 1.6\,(\mathcal{B})) \cdot 10^{-6}$, which is the single world's best measurement and in agreement with the current world average. The non-factorisable effects are found to be compatible with $|a_{\mathrm{NF}}| = 1.0$, *i.e.* naive factorisation. On top of this, the parameter $r_{D\pi}$ and the dependence of the hadronisation fraction f_s/f_d on collision energy are measured with high precision.

CERN-THESIS-2018-137
//2018

Contents

1 Introduction

1.1 Motivation

The weak interaction is one of the three fundamental forces in the Standard Model of particle physics (SM). It is the only fundamental force that couples quarks from different flavours. The weak interaction can manifest itself under exchange of a $W^{\pm}$ boson. The coupling strength of this flavour-changing interaction is given by the Cabibbo-Kobayashi-Maskawa (CKM) matrix,

$$V_{CKM} = \begin{pmatrix} V_{ud} & V_{us} & V_{ub} \\ V_{cd} & V_{cs} & V_{cb} \\ V_{td} & V_{ts} & V_{tb} \end{pmatrix}. \tag{1}$$

To verify the CKM paradigm, it is crucial to perform accurate measurements of the CKM-matrix elements. Any discrepancy or inconsistency among the numerous measurements of the CKM matrix can reveal effects from new particles or forces in the SM. Of the CKM-matrix elements, the value of V_{ub} has the biggest uncertainty. V_{ub} gives the coupling strength of the $b \to u$ quark transition and can be measured through so-called *inclusive* and *exclusive* measurements. The inclusive measurements are done by analysing $B \to X_u l \bar{\nu}_l$ decays, in which X_u can be any hadron, or system of hadrons, containing an up-quark resulting from a $b \to u$ transition. Exclusive measurements look at specific decays, such as $B^0 \to \pi^- \ell^+ \nu$ [1].
The values of V_{ub} from inclusive and exclusive measurements and the average, as found in the 2018 edition of the Particle Data Group (PDG), are as follows [2]:

$$|V_{ub}| = (4.49 \pm 0.28) \times 10^{-3} \quad \text{(inclusive)}, \tag{2}$$
$$|V_{ub}| = (3.70 \pm 0.16) \times 10^{-3} \quad \text{(exclusive)}, \tag{3}$$
$$|V_{ub}| = (3.94 \pm 0.36) \times 10^{-3} \quad \text{(average)}. \tag{4}$$

The inclusive and exclusive measurements clearly show a discrepancy, for which no explanation has been found yet. To take this discrepancy into account, the uncertainty on the average value of V_{ub} is scaled by a factor of 2.6. In order to solve this discrepancy, new measurements of V_{ub} are necessary.

Therefore, the goal of this project is to establish a new exclusive measurement of $|V_{ub}|$ by determining the branching fraction of $B^0 \to D_s^+ \pi^-$. The $B^0 \to D_s^+ \pi^-$ decay is a hadronic B decay, in which a B^0 meson decays through the $b \to u$ transition to a charged pion and a D_s^+ meson. Fig. 1 shows the tree diagram of the $B^0 \to D_s^+ \pi^-$ decay.

1.1.1 Probing V_{ub} and the non-factorisable effects

The tree diagram in Fig. 1 shows the single first-order tree diagram contributing to the $B^0 \to D_s^+ \pi^-$ decay. Therefore, the $B^0 \to D_s^+ \pi^-$ branching fraction scales with $|V_{ub}|^2$ and can be used to probe $|V_{ub}|$.
However, the branching fraction can be affected by non-factorisable effects,

$$\mathcal{B}(B^0 \to D_s^+ \pi^-) \propto |V_{ub}|^2 |F(B^0 \to \pi^-)|^2 f_{D_s}^2 |a_{\mathrm{NF}}|^2, \tag{5}$$

where $F(B^0 \to \pi^-)$ is the form factor, f_{D_s} is the D_s^+ decay constant and $|a_{\mathrm{NF}}|$ quantifies the non-factorisable effects. Because of this dependence on V_{ub} and a_{NF}, the branching

fraction of $B^0 \to D_s^+\pi^-$ is used to probe the product $|V_{ub}||a_{\rm NF}|$. Probing $|V_{ub}|$ and $|a_{\rm NF}|$ separately can only be done using external input for either.

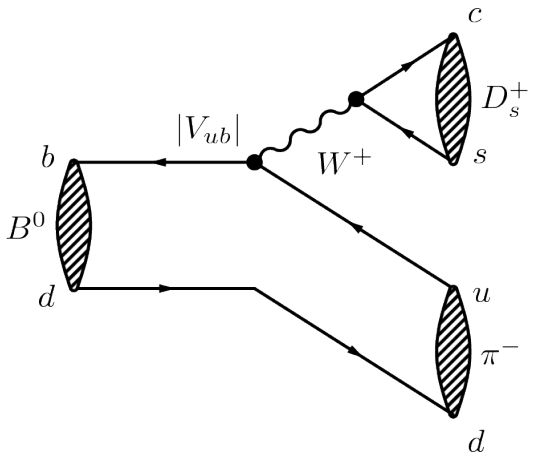

Figure 1: Tree diagram of $B^0 \to D_s^+\pi^-$, in which a B^0 meson decays through the weak interaction to a D_s^+ meson and a charged pion.

Thus, besides probing $|V_{ub}|$, another reason to perform this analysis is to determine the non-factorisation constant $|a_{\rm NF}|$. This quantity indicates how much the D_s^+ meson and pion interact through the strong force. Measuring $|a_{\rm NF}|$ is very important, since there is no good theoretical prediction for it. The value has to be obtained by experiment. If $|a_{\rm NF}|$ is equal to one, this means that there is (approximately) no exchange of gluons between the D_s^+ meson and the pion, which is also called *naive factorisation*. Naive factorisation is in particular valid if the meson created from the $W^\pm$ boson is light (*e.g.* a pion) [3].

Other QCD effects also bring uncertainties to the branching fraction. The form factor $F(B^0 \to \pi^-)$ describes the transition of the B^0 meson to a charged pion in the lower half of the tree diagram, as can be seen in Fig. 1. The decay constant f_{D_s} represents the QCD interactions within the 'ejected' D_s^+ meson.

1.1.2 Determining $r_{D\pi}$

Besides probing $|V_{ub}|$ and $|a_{\rm NF}|$, another important quantity that can be determined using $\mathcal{B}(B^0 \to D_s^+\pi^-)$ is $r_{D\pi}$. This is the ratio between the decay amplitude of the Cabibbo suppressed decay $B^0 \to D^+\pi^-$ and Cabibbo favoured decay $B^0 \to D^-\pi^+$,

$$r_{D\pi} = \left| \frac{A(B^0 \to D^+\pi^-)}{A(B^0 \to D^-\pi^+)} \right|. \tag{6}$$

This ratio is required for studying charge parity (CP) asymmetries in $B^0 \to D^\mp\pi^\pm$ decays [4]. However, measuring this ratio is experimentally very difficult, since $B^0 \to D^+\pi^-$ has the same final state as the charge-conjugated and Cabibbo favoured $\overline{B}^0 \to D^+\pi^-$. To solve this, a similar decay can be used to quantify $r_{D\pi}$, *i.e.* $B^0 \to D_s^+\pi^-$. The Cabibbo suppressed $B^0 \to D^+\pi^-$ decay is very similar to $B^0 \to D_s^+\pi^-$, since in both a B^0 meson decays to a charged pion and a meson containing a c quark, undergoing a $b \to u$ transition. Assuming SU(3) flavour symmetry, which is the symmetry upon the exchange of the

s and d quarks, Eq. (6) can be written as [5, 6]

$$r_{D\pi} = \tan\theta_c \frac{f_{D^+}}{f_{D_s}} \sqrt{\frac{\mathcal{B}(B^0 \to D_s^+\pi^-)}{\mathcal{B}(B^0 \to D^-\pi^+)}}, \tag{7}$$

where θ_c is the Cabibbo angle and $f_{D_{(s)}}$ is the decay constant of $D^\pm_{(s)}$. Thus, measuring $\mathcal{B}(B^0 \to D_s^+\pi^-)$ also helps to improve sensitivity to *CP* asymmetries in $B^0 \to D^\pm\pi^\mp$ decays.

1.1.3 Determining f_s/f_d dependence on collision energy

Finally, the results of this analysis can also be used to study the difference in the production rate ratio of B_s^0 and B^0 mesons, also called f_s/f_d, between data taken with the centre-of-mass energies $\sqrt{s} = 7\,\text{TeV}$ and $\sqrt{s} = 8\,\text{TeV}$, and $\sqrt{s} = 13\,\text{TeV}$. The value of f_s/f_d is crucial for *any* B_s^0 branching fraction determination at LHCb. The most important example is the measurement of $\mathcal{B}(B_s^0 \to \mu^+\mu^-)$, which is sensitive to contributions from new particles or forces, and which is a flagship measurement of LHCb. As explained in Section 1.2, the yields and efficiencies of the $B_s^0 \to D_s^-\pi^+$ and $B^0 \to D^-\pi^+$ decays are determined with high precision in this analysis. This enables us to determine the ratio of f_s/f_d between data taken with a centre-of-mass energy of $\sqrt{s} = 7\,\text{TeV}$ and $\sqrt{s} = 8\,\text{TeV}$, and $\sqrt{s} = 13\,\text{TeV}$,

$$\frac{f_s/f_d|_{\sqrt{s}=13\,\text{TeV}}}{f_s/f_d|_{\sqrt{s}=7/8\,\text{TeV}}} = \frac{(N_{B_s^0\to D_s^-\pi^+}\epsilon_{B^0\to D^-\pi^+})/(N_{B^0\to D^-\pi^+}\epsilon_{B_s^0\to D_s^-\pi^+})|_{\sqrt{s}=13\,\text{TeV}}}{(N_{B_s^0\to D_s^-\pi^+}\epsilon_{B^0\to D^-\pi^+})/(N_{B^0\to D^-\pi^+}\epsilon_{B_s^0\to D_s^-\pi^+})|_{\sqrt{s}=7/8\,\text{TeV}}}. \tag{8}$$

In Ref. [7] this ratio is calculated using the ratio of the efficiency corrected $B_s^0 \to J/\psi\,\phi$ and $B^+ \to J/\psi\,K^+$ decays:

$$\frac{f_s/f_d|_{\sqrt{s}=13\,\text{TeV}}}{f_s/f_d|_{\sqrt{s}=7\,\text{TeV}}} = 1.068 \pm 0.046. \tag{9}$$

This value is both compatible with and higher than 1.0, but due to large uncertainties, it is not possible to claim a dependence on collision energy. This analysis is able to deliver a new high-precision measurement of this quantity.

1.2 Analysis strategy

In this analysis, data from *pp* collisions at LHCb is used. An amount of $1.0\,\text{fb}^{-1}$ is obtained at a centre-of-mass energy $\sqrt{s} = 7\,\text{TeV}$ (2011), $2.0\,\text{fb}^{-1}$ at $\sqrt{s} = 8\,\text{TeV}$ (2012) and $2.0\,\text{fb}^{-1}$ at $\sqrt{s} = 13\,\text{TeV}$ (2015,2016). To be able to measure the branching fraction of $B^0 \to D_s^+\pi^-$, the final-state particles of this decay have to be reconstructed and combined into a decay. The final-state particles consist of a pion and three other hadrons coming from the decay $D_s^+ \to K^+K^-\pi^+$, as can be seen in Fig. 2.

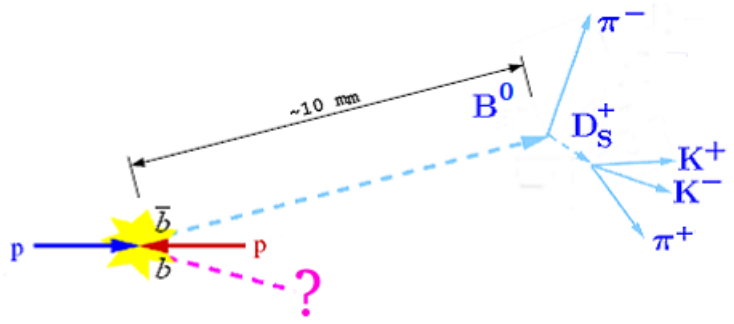

Figure 2: Simplified view of the $B^0 \to D_s^+ \pi^-$ decay. At pp collisions a B^0 meson is formed, that decays to a π^- and a D_s^+ meson after travelling about 10 mm. Finally, the D_s^+ meson decays to $K^+K^-\pi^+$ after a few millimetres.

Combining these four final-state particles leads to an invariant mass peaking around the B^0 meson mass, $(5279.63 \pm 0.15)\,\text{MeV}/c^2$ [2]. Since $B^0 \to D_s^+ \pi^-$ is not the only decay producing these final states, several background decays need to be modelled, which will be explained in full detail in Section 4. Calculating the invariant mass of the final-state particles in data will result in a histogram like the one in Fig. 3. This histogram clearly shows the peak of the $B_s^0 \to D_s^- \pi^+$ decay, while the $B^0 \to D_s^+ \pi^-$ signal is located underneath the arrow. The yield of the $B^0 \to D_s^+ \pi^-$ signal is highly sensitive to the backgrounds events located both underneath and left of $B^0 \to D_s^+ \pi^-$, as well as the left tail of the $B_s^0 \to D_s^- \pi^+$ signal. Therefore, it is crucial in this analysis to understand and model these backgrounds, along with the $B_s^0 \to D_s^- \pi^+$ decay.

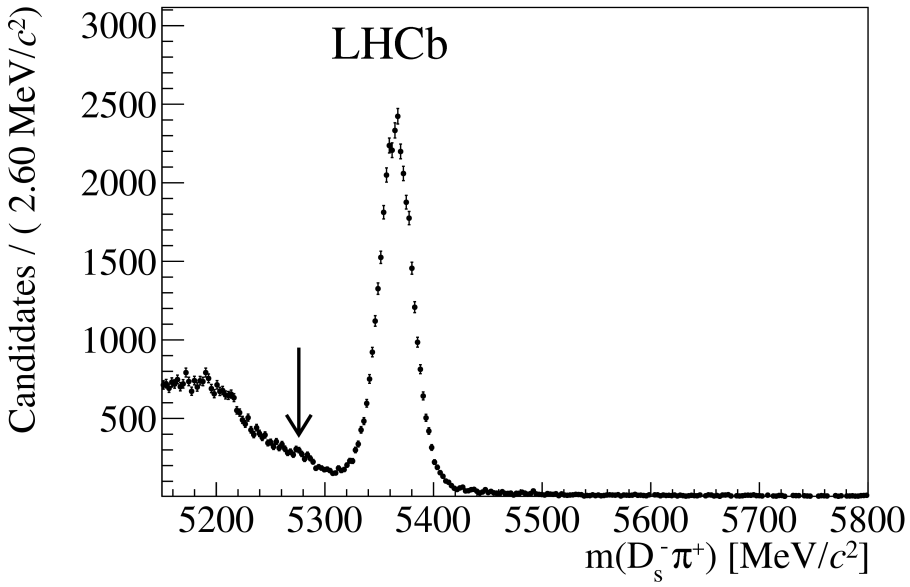

Figure 3: The $D_s^- \pi^+$ invariant mass data. The clear peak in this histogram is the $B_s^0 \to D_s^- \pi^+$ decay, while the $B^0 \to D_s^+ \pi^-$ signal is located underneath the arrow around $5280\,\text{MeV}/c^2$.

By fitting background and signal shapes to Fig. 3, the yield belonging to $B^0 \to D_s^+ \pi^-$ is determined. However, this is not sufficient information to determine the branching

fraction. In addition, the efficiency of selecting these signal events as well as the branching fraction $\mathcal{B}(D_s^- \to K^-K^+\pi^-)$ are required. Since we do not know how many B mesons are produced in LHCb, a normalisation channel is used. In this analysis, the $B^0 \to D^-\pi^+$ decay is used as the normalisation channel, because of its topological similarity to $B^0 \to D_s^+\pi^-$ and the relatively small uncertainty on its branching fraction. With the addition of this normalisation channel, the yield and efficiency of $B^0 \to D^-\pi^+$, and the branching fractions $\mathcal{B}(B^0 \to D^-\pi^+)$ and $\mathcal{B}(D^- \to K^+\pi^-\pi^-)$ are also required for the branching fraction calculation of $B^0 \to D_s^+\pi^-$. Combining these branching fractions, yields and efficiencies gives

$$\mathcal{B}(B^0 \to D_s^+\pi^-) = \mathcal{B}(B^0 \to D^-\pi^+)\frac{\epsilon_{B^0\to D^-\pi^+}}{\epsilon_{B^0\to D_s^+\pi^-}}\frac{N_{B^0\to D_s^+\pi^-}}{N_{B^0\to D^-\pi^+}}\frac{\mathcal{B}(D^- \to K^+\pi^-\pi^-)}{\mathcal{B}(D_s^- \to K^-K^+\pi^-)}. \tag{10}$$

The branching fractions on the right-hand side of Eq. (10) are measured with high precision in so-called B-Factories. At B-Factories, electrons are collided with positrons at centre-of-mass energies corresponding to resonances of the Υ meson, in particular the $\Upsilon(4S)$ resonance [8]. This is a resonance consisting of a $b\bar{b}$-quark pair that has a rest mass just above threshold to produce two B mesons, resulting more than 96% of the times in $B\overline{B}$ decays. The measured branching fractions are [2]

$$\mathcal{B}(B^0 \to D^-\pi^+) = (2.52 \pm 0.13) \times 10^{-3}, \tag{11}$$
$$\mathcal{B}(D^- \to K^+\pi^-\pi^-) = (8.98 \pm 0.28) \times 10^{-2}, \tag{12}$$
$$\mathcal{B}(D_s^- \to K^-K^+\pi^-) = (5.45 \pm 0.17) \times 10^{-2}. \tag{13}$$

Using these branching fractions, the total relative uncertainty from external inputs is 6.8%.

The current measurements of the branching fraction of $B^0 \to D_s^+\pi^-$ from the B-Factories show a slight tension [5, 6],

$$\mathcal{B}(B^0 \to D_s^+\pi^-) = (25 \pm 4 \pm 2) \times 10^{-6} \quad \text{(BaBar)}, \tag{14}$$
$$\mathcal{B}(B^0 \to D_s^+\pi^-) = (19.9 \pm 2.6 \pm 1.8) \times 10^{-6} \quad \text{(Belle)}. \tag{15}$$

The goal of this analysis is to measure the yields and efficiencies of $B^0 \to D_s^+\pi^-$ and the normalisation channel $B^0 \to D^-\pi^+$ and to use these to improve the measurement of the branching fraction of $B^0 \to D_s^+\pi^-$. This branching fraction can be used to quantify non-factorisable effects in this decay and to probe $|V_{ub}|$, as well as the parameter $r_{D\pi}$.

The rest of this thesis is as follows: Section 2 describes the Large Hadron Collider (LHC) and the LHCb experiment. The event selection and determination of the corresponding efficiencies are described in Section 3. The modelling of backgrounds is specified in Section 4, while the study on the signal shape can be found in Section 5. Section 6 shows the resulting $D_s^-\pi^+$ data fits together with the corresponding yields. Sources of systematic uncertainties and consistency checks are described in Section 7. The resulting branching fraction and its implications will be shown and explained in Section 8. Finally, Section 9 gives a conclusion on this analysis and an outlook on future work. Appendices containing fitted parameters, definitions of probability density functions, particle identity reweighting histograms, and background templates can be found in Appendices A, B, C, and D, respectively.

2 LHC and the LHCb detector

2.1 LHC

With a circumference of 27 kilometres, the Large Hadron Collider (LHC) is the largest particle accelerator in the world. The LHC is located on the border of Switzerland and France, near Geneva, and is designed to collide proton beams at a centre-of-mass energy of 14 TeV [9]. It has four main experiments, located at the four crossing points of the two beams. These experiments are ATLAS (A Toroidal LHC ApparatuS), CMS (Compact Muon Solenoid), ALICE (A Large Ion Collider Experiment), and LHCb (Large Hadron Collider beauty). ATLAS and CMS are general purpose detectors, designed to cover a wide range of physics. In 2012 ATLAS and CMS announced that they found a new particle, the Higgs boson [10, 11]. ALICE is specialised in studying lead-ion collisions. In these collisions a quark-gluon plasma can be created, which is used to study the properties of the Universe a fraction of a second after the Big Bang. The LHCb detector is specialised in studying hadrons with a bottom or charm quark. The next section discusses this detector in detail.

Before entering the LHC, protons or lead-ions go through a series of pre-accelerators which accelerate them before entering the next accelerator. Two of these accelerators are the Proton Synchrotron (PS) and the Super Proton Synchrotron (SPS). Fig. 4 provides a schematic overview of the LHC with its four main experiments, the PS, and the SPS.

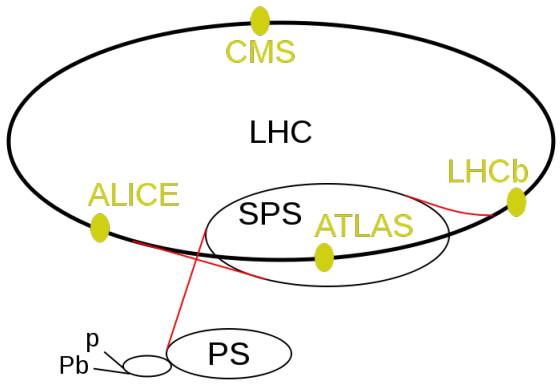

Figure 4: Overview of the LHC. In green are the main LHC experiments: ATLAS, CMS, LHCb, and ALICE.

2.2 LHCb

LHCb is one of the four main experiments at the LHC and is in particular specialised in studying *CP* violation in b and c hadrons. With these measurements LHCb can help to explain the matter-antimatter asymmetry in the universe, one of the big open questions in physics.

In pp collisions at the LHC, b (and $\bar{b}$) hadrons are usually formed close to the beam in the forward or backward direction [12]. The LHCb detector uses this by having a geometry oriented to the forward direction of the beam pipe. To be able to locate the vertices belonging to b-hadron decays, which typically decay after about 1 cm, LHCb has

a Vertex Locator, located close to the interaction point.

LHCb consists of multiple layers of subdetectors, which are used to acquire information such as the track, identity, momentum, and energy of particles. A cross-section of the LHCb and its subdetectors is shown in Fig. 5.

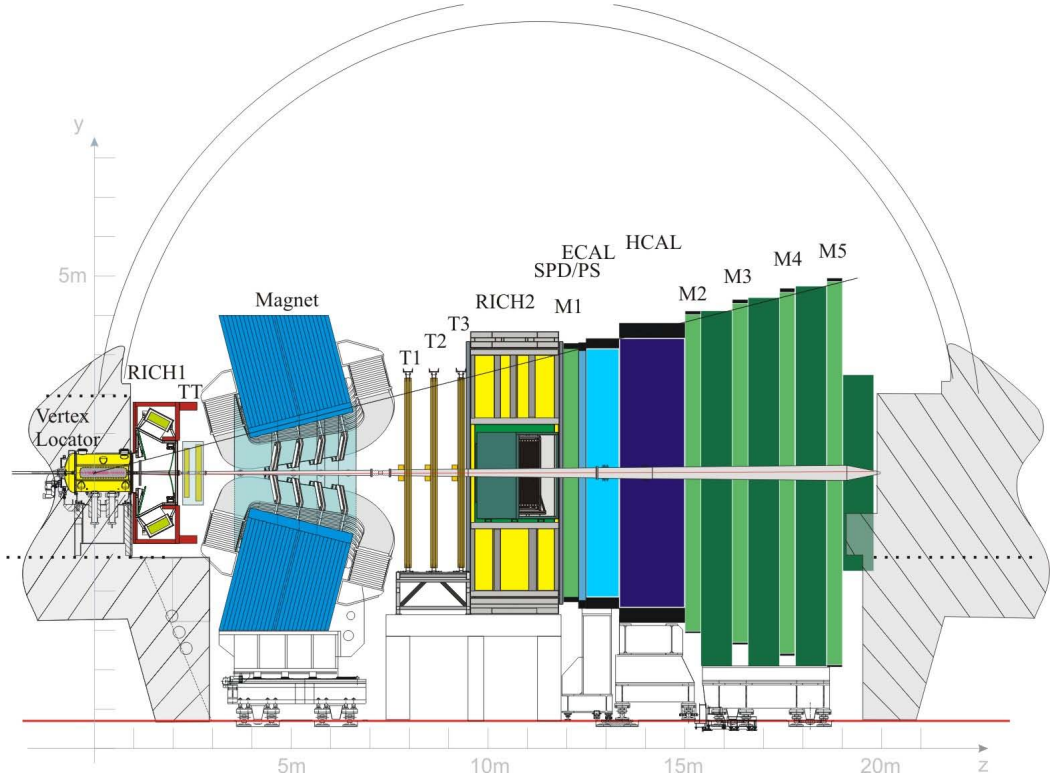

Figure 5: A cross-section of the LHCb detector and its subdetectors.

The LHCb detector can be divided in five parts: the tracking system, the magnet, the Cherenkov detectors, the calorimeter system, and the muon stations.

- The tracking system of LHCb consists of the Vertex Locator (**VELO**), the Tracker Turicensis (**TT**), and three planar tracking stations **T1**, **T2** and **T3**. The tracking stations T1, T2 and T3 consist of the Inner Tracker (**IT**) and the Outer Tracker (**OT**), with the IT closer to the beam pipe than the OT.
  The VELO [13] is the subdetector closest to the interaction point. This enables it to very precisely measure the location of secondary vertices of b- and c- hadron decays. The VELO consists of a series of silicon modules placed only 8 mm from the interaction point and is built in a way that it can be opened with respect to the beam pipe when the beam is unfocused.
  The TT and IT [14] are silicon subdetectors, designed to track charged particles. The TT is located upstream of the magnet while the IT is located downstream of the magnet, as can be seen in Fig. 5. The OT [15] is a gaseous drift time detector consisting of 12 layers of straw tubes.

- To calculate the momentum of a charged particle, a **magnet** [16] is used. This magnet has an integrated magnetic field of 4 Tm. The resulting curvature of charged particles is used to determine their momentum and charge. The polarity of the

magnet is inverted about two times a month (during Run 1 [17]) to cancel detector asymmetries. Consequently, the recorded data is split between magnet polarities, labelled as *MagDown* and *MagUp* in the rest of this thesis.

- The Ring-Imaging CHerenkov (**RICH**) [18] detectors are designed to identify charged particles using Cherenkov radiation. This radiation is produced when the velocity of a charged particle exceeds the speed of light in the radiator medium. Cherenkov radiation is emitted in a cone with an angle that is dependent on the radiator medium and the velocity of the particle. By calculating the velocity of a particle with this Cherenkov angle and by combining this velocity with the momentum of corresponding track, the mass of the particle is calculated. With this information, RICH discriminates between the pions, kaons and protons. The two RICH detectors are RICH1, located between the VELO and the TT, and RICH2, located downstream of T3.

- The calorimeter system [19] of LHCb consists of multiple layers: the Scintillating Pad Detector (**SPD**), the Pre-Shower (**PS**) detector, the Electromagnetic Calorimeter (**ECAL**), and the Hadronic Calorimeter (**HCAL**).
  The SPD distinguishes neutral and charged particles entering the calorimeter system. The PS Detector can distinguish particles based on their electromagnetic character, for example whether a particle is an electron or a hadron. Both the SPD and the PS are scintillating planes separated by a lead sheet.
  The ECAL measures energies and positions of particles that interact through the electromagnetic interaction. It consists of alternating layers of scintillator and lead.
  The HCAL is able to measure energies and positions of hadrons. This subdetector consists of tiles of scintillator material and iron orientated parallel to the beam.

- Finally, the muon system [20] is used to identify muons. The muon system consists of five stations (**M1**-**M5**), which cover a combined area of $435\,\mathrm{m}^2$. The muon stations use multi-wire proportional chambers (MWPCs), to detect passing muons. A MWPC is a chamber with high voltage anode wires and cathode plates as walls, which is filled with a gas that can be ionised by the passage of charged particles.

3 Data Flow: event selection

At the LHC, 40 million bunches of protons cross per second at interaction points such as at LHCb. Storing information about all the resulting collisions would require about 1 TB/s. As this is too much to store, only selecting the most important information is necessary. This is done in multiple steps, as is showed in Fig. 6. The first selection step is the trigger, which is explained in Section 3.1. Afterwards, the reconstruction of tracks and clusters takes place on triggered raw data. Then the data goes through the stripping, which builds candidate particles from the reconstructed tracks and selects events based on kinematics and geometric properties. After stripping, more analysis-specific selections are applied, the offline selection. The selected data is stored in nTuples and can be used in analyses. An nTuple is a data format commonly used in high energy physics to store information of particle interactions.

This analysis uses LHCb data taken in the years 2011 and 2012 (Run 1), and in 2015 and 2016 (Run 2), at centre-of-mass energies of $\sqrt{s} = 7\,\text{TeV}$ (2011), $\sqrt{s} = 8\,\text{TeV}$ (2012), and $\sqrt{s} = 13\,\text{TeV}$ (Run 2).

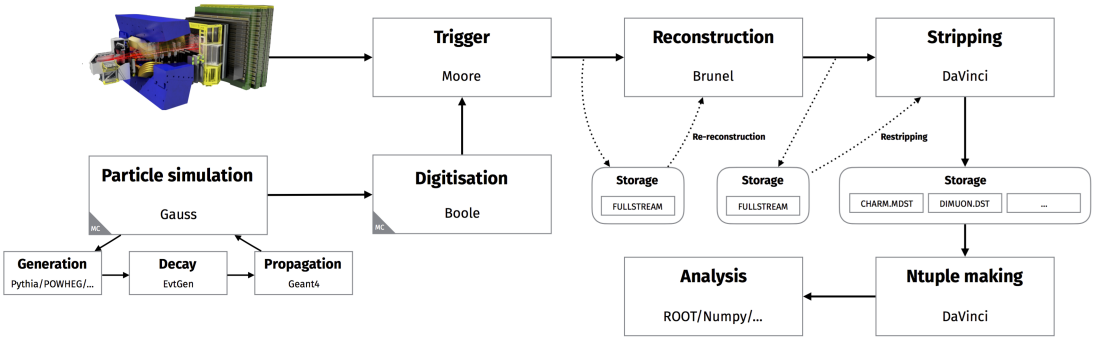

Figure 6: A schematic overview of the steps of data selection at LHCb.

3.1 Trigger selection

The trigger [21] is the first step in selecting LHCb data. The trigger consists of a hardware trigger (also called Level 0, or L0) and a software trigger (also called High Level Trigger, or HLT).

The hardware trigger of LHCb receives about 40 million events per second and has to decide very quickly what events to keep. The decision of the hardware trigger is based on information from the calorimeters and the muon stations, which are described in Section 2.2. With the information of these subdetectors, events with a high transverse momentum or with large transverse energy are selected. For hadrons, the studied type of particles in this analysis, a transverse energy of more than 3.68 GeV deposited in the calorimeter is required [22]. Around one million events per second pass the selection of the L0 trigger.

The remaining events go to the software trigger, which consists of two stages, HLT1 and HLT2.

In HLT1 [23], only a partial event reconstruction takes place, since computing power is limited. First, track segments are reconstructed with information from the VELO. If the impact parameter (IP) of these track segments is large or if the track segments can be

matched with hits in the muon chambers, the track segments are selected and extended to the tracking stations. Afterwards, each event is required to have a track segment with a large enough transverse momentum, $p_{\mathrm{T}} > 1.6\,\mathrm{GeV}/c$. An event rate of about 100 kHz remains after HLT1.

HLT2 [24, 25] reconstructs tracks with $p_{\mathrm{T}} > 300\,\mathrm{MeV}/c$ for Run 1 data and all tracks for Run 2 data. The reconstructed events are required to form two-, three- and four-track vertices. On top of this, events are selected, if they are likely to contain a $\phi \to K^-K^+$ resonance in the signal. This is based on transverse momentum, invariant mass, IP and particle identity of K^-K^+ candidates. The events selected by HLT2 are stored on disk.

The final event rate after the trigger system is about 5 kHz in 2012 (12.5 kHz in Run 2). The trigger selection is done online, which means that the measured data is immediately passed to the trigger system for selection. During the trigger process of 2012 data, however, 20% of data selected by the L0 trigger was stored temporarily offline, before being processed by the HLT trigger [26].

3.2 Stripping selection

Stripping is an offline selection done after the trigger, based on kinematic and topological properties of events. For each year of data taking, a different stripping version is used. The stripping versions used in this analysis are 21r1, 21, 24, and 28 for the years 2011, 2012, 2015, and 2016, respectively. Each stripping version has stripping lines, which can contain some differences. Stripping lines are sets of cuts used for a certain type of decays. In this analysis the stripping line `B02DPiD2HHHBeauty2CharmLine` is used, which can be used for decays of a beauty meson to a charmed meson and a bachelor particle. The bachelor particle is the daughter particle of the beauty meson that is observed directly, rather than by its decay products. In the $B^0 \to D_s^+\pi^-$ signal, this is a pion, but a kaon can also be the bachelor particle. Table 1 shows a summary of the cuts used in this stripping line and the differences between the versions.

First of all, each event is required to have less than 500 long tracks. Long tracks are tracks that have passed through both the VELO and the tracking stations. Afterwards, all particle candidates need to have a transverse momentum p_{T} of at least $100\,\mathrm{MeV}/c$ and a momentum p of at least $1000\,\mathrm{MeV}/c$. On top of that are requirements with respect to the track quality. The track χ^2/ndf gives the χ^2 of the track fit per degree of freedom. The cut on track χ^2_{IP} requires the track to be inconsistent with originating from a primary vertex (PV). Finally, a cut on ghost probability is used to select high-quality tracks.

Afterwards, a $D^\pm_{(s)}$ candidate is formed from three charged pion or kaon candidates. To be able to successfully form a $D^\pm_{(s)}$ candidate extra requirements are imposed. At least one of the $D^\pm_{(s)}$ daughters, to which a $D^\pm_{(s)}$ decays, is required to have a transverse momentum p_{T} of more than $500\,\mathrm{MeV}/c$, a momentum p of at least $5000\,\mathrm{MeV}/c$, and a low track χ^2 per degree of freedom. On top of that, the distance of closest approach (DOCA) between any of two tracks of the $D^\pm_{(s)}$ daughters needs to be less than 0.5 mm. Furthermore, the sum of transverse momenta of the $D^\pm_{(s)}$ daughters needs to be at least $1800\,\mathrm{MeV}/c$, while the invariant mass of the $D^\pm_{(s)}$ candidate has to be between 1769.62 and $2068.49\,\mathrm{MeV}/c^2$.

The bachelor pion has the same requirements on p_{T}, p and track χ^2/ndf, as imposed on at least one of the $D^\pm_{(s)}$ daughters.

Finally, a $B^0_{(s)}$ candidate is constructed from a $D^\pm_{(s)}$ candidate and a bachelor pion.

The resulting $B^0_{(s)}$ is required to have a invariant mass between 4750 and 7000 MeV/c^2 and a lifetime of at least 0.2 ps. This $B^0_{(s)}$ candidate has to be compatible with originating from the PV, by requiring the χ^2_{IP} w.r.t. the PV to be smaller than 25. Additionally, the $B^0_{(s)}$ is also required to have a child with a minimum vertex distance from the the PV of 0.1 mm, a p_{T} of more than 1700 MeV/c, a p of more than 10 GeV/c, and a track χ^2_{IP} of more than 16, meaning that the fit of the track is inconsistent with the fit of the track including the PV.

After stripping, the remaining events are stored and can be used to make nTuples.

Variable	Stripping 21r1	Stripping 21	Stripping 24	Stripping 28
Each event				
# long tracks	< 500	< 500	< 500	< 500
Each particle				
Track χ^2/ndf	**< 3.0**	**< 3.0**	**–**	**< 4.0**
Track χ^2_{IP}	> 4.0	> 4.0	> 4.0	> 4.0
Track ghost probability	< 0.4	< 0.4	< 0.4	< 0.4
p_{T}	> 100 MeV/c	> 100 MeV/c	> 100 MeV/c	> 100 MeV/c
p	> 1000 MeV/c	> 1000 MeV/c	> 1000 MeV/c	> 1000 MeV/c
Bachelor particle				
Track χ^2/ndf	**< 2.5**	**< 2.5**	**< 2.5**	**< 4.0**
p_{T}	> 500 MeV/c	> 500 MeV/c	> 500 MeV/c	> 500 MeV/c
p	> 5000 MeV/c	> 5000 MeV/c	> 5000 MeV/c	> 5000 MeV/c
$D^{\pm}_{(s)}$ candidate				
invariant mass	$[1769.62, 2068.49]$ MeV/c	$[1769.62, 2068.49]$ MeV/c	$[1769.62, 2068.49]$ MeV/c	$[1769.62, 2068.49]$ MeV/c
p_{T}	> 1800 MeV/c	> 1800 MeV/c	> 1800 MeV/c	> 1800 MeV/c
DOCA cut	< 0.5 mm	< 0.5 mm	< 0.5 mm	< 0.5 mm
$D^{\pm}_{(s)}$ has daughter with				
Track χ^2/ndf	**< 2.5**	**< 2.5**	**< 2.5**	**< 4.0**
p_{T}	> 500 MeV/c	> 500 MeV/c	> 500 MeV/c	> 500 MeV/c
p	> 5000 MeV/c	> 5000 MeV/c	> 5000 MeV/c	> 5000 MeV/c
$B^0_{(s)}$ candidate				
invariant mass	$[4750, 7000]$ MeV/c	$[4750, 7000]$ MeV/c	$[4750, 7000]$ MeV/c	$[4750, 7000]$ MeV/c
proper lifetime	> 0.2 ps	> 0.2 ps	> 0.2 ps	> 0.2 ps
χ^2_{IP} w.r.t. PV	< 25	< 25	< 25	< 25
$B^0_{(s)}$ has a child with				
Track χ^2_{IP}	> 16	> 16	> 16	> 16
Minimum distance of track from PV	> 0.1 mm	> 0.1 mm	> 0.1 mm	> 0.1 mm
p_{T}	> 1700 MeV/c	> 1700 MeV/c	> 1700 MeV/c	> 1700 MeV/c
p	> 10 GeV/c	> 10 GeV/c	> 10 GeV/c	> 10 GeV/c

Table 1: Summary of the cuts of stripping line `B02DPiD2HHHBeauty2CharmLine` in the stripping versions 21r1, 21, 24, and 28, corresponding to the years 2011, 2012, 2015, and 2016, respectively. Highlighted in bold are the cuts that differ between stripping versions. A dash indicates that the corresponding cut is not applied.

3.3 Offline selection

After applying this general pre-selection, more cuts are placed to further reduce the amount of background events. This selection after stripping is also called the offline selection. These cuts are tighter than the cuts in stripping, as offline selection is less general.

Two different types of cuts are present in the offline selection: kinematic cuts and particle identification (PID) cuts. Kinematic cuts select events based on kinematic variables like invariant mass, while PID cuts select events, based on particle identity using information from the RICH subdetectors.

The invariant mass is also called the rest mass of a particle. If the particle is not

directly detected, this can be calculated by its decay products,

$$M_{inv} = \sqrt{(\sum_{i}^{N} E_i)^2 - ||\sum_{i}^{N} \boldsymbol{p}_i||^2}, \tag{16}$$

where N is the amount of final-state particles, three in case of a $D^-_{(s)}$ meson, E_i is the energy per particle and $\boldsymbol{p}_i$ is the three-momentum per particle. In case of $B^0_{(s)}$, a different method is used. Instead of calculating the invariant mass with Eq. (16) using all of the final-state particles, *i.e.* the bachelor pion and the $D^-_{(s)}$ daughters, the $D^-_{(s)}$ meson is constrained to its nominal value, which is used together with the bachelor pion to compute a constrained invariant $B^0_{(s)}$ mass.

The first kinematic cuts that are used are the invariant mass range cuts. The B^0_s (B^0) invariant mass has to be between 5150 and 5800 MeV/c^2 (5000 and 5800 MeV/c^2). The mass of the $D^\pm_s$ ($D^\pm$) candidate is required to be between 1930 and 2065 MeV/c^2 (1830 and 1920 MeV/c^2). To ensure that the decays happen through an intermediate $D^\pm_{(s)}$ rather than prompt decays, cuts are done on the $D^\pm_{(s)}$ lifetime and vertex separation χ^2 with respect to the $B^0_{(s)}$ candidate. A $D^\pm_s$ ($D^\pm$) candidate is required to have a nonzero positive lifetime and a vertex separation χ^2 of at least 2 (9).

On top of these kinematical cuts, cuts based on PID are applied. This is mostly done with information from the RICH subdetectors, which are described in Section 2.2. Using this information, the variables $\mathrm{DLL}_{K\pi}$, $\mathrm{DLL}_{p\pi}$ and $\mathrm{DLL}_{\mu\pi}$ are assigned to every charged hadron ($\pi^\pm$, $K^\pm$, $^{(}\overline{p}^{)}$). These variables represent the difference in the log-likelihood between two particle hypotheses. A negative value means that the candidate is likely to be a pion, while a positive value means that the candidate is likely to be a kaon, proton, or muon. To be certain that the bachelor particle is a pion, two different PID cuts are used, $\mathrm{DLL}_{\mu\pi} < 2$ and $\mathrm{DLL}_{K\pi} < 0$, to distinguish the bachelor pion from a muon and a kaon, respectively.

In $D^-_s\pi^+$ decays, D^-_s candidates are reconstructed under the $K^-K^+\pi^-$ hypothesis. Three modes are separated in which a D^-_s candidate can decay to $K^-K^+\pi^-$: the $D^-_s \to \phi(1020)\pi^-$ ($\phi(1020) \to K^-K^+$) resonance, the $D^-_s \to K^*(892)^0K^-$ ($K^*(892)^0 \to K^+\pi^-$) resonance and the non-resonant mode. These three decay modes are visualised with a Dalitz plot in Fig. 7 using simulated $B^0_s \to D^-_s\pi^+$ events.

First of all, events corresponding to the $\phi\pi^-$ resonance are selected. This is done by selecting events with $m(K^-K^+)$ between 1000 and 1040 MeV/c^2 and by requiring the $\mathrm{DLL}_{K\pi}$ of both kaons to be higher than -2. A selection corresponding to the $K^{*0}K^-$ resonance is imposed on the remaining events. The $m(K^+\pi^-)$ has to be between 842 and 942 MeV/c^2, while a stronger PID cut is imposed on the kaon with the same charge as the D^-_s candidate, $\mathrm{DLL}_{K\pi} > 5$, than on the opposite-charge kaon, $\mathrm{DLL}_{K\pi} > -2$. The remaining events are only cut on PID variables. Both kaons are required to have $\mathrm{DLL}_{K\pi}$ greater than 5, while the pion needs to have a $\mathrm{DLL}_{K\pi}$ smaller than 10. All the cuts corresponding to the D^-_s modes can be found in Table 2.

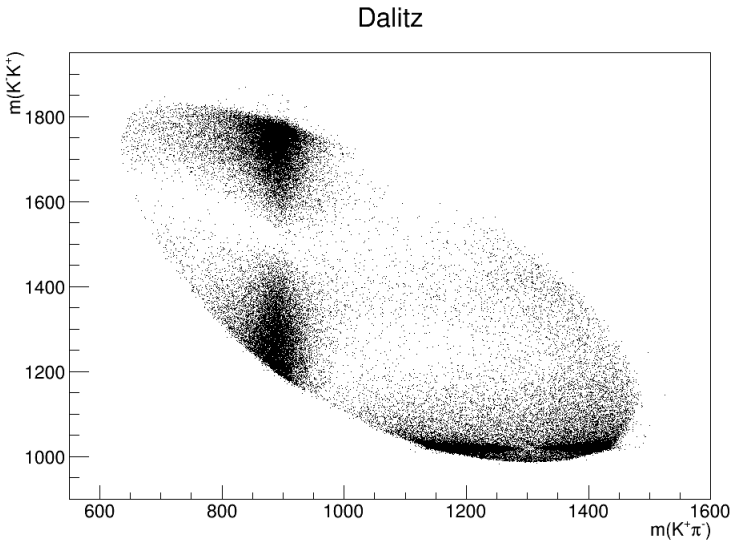

Figure 7: Dalitz plot of the $\phi\pi^-$ and $K^{*0}K^-$ resonances in $B_s^0 \to D_s^-\pi^+$ Monte Carlo. The horizontal axis shows the invariant mass of $K^+\pi^+$, the decay products of $K^*(892)^0$. A great number of events can be seen around $892\,\mathrm{MeV}/c^2$, the rest mass of $K^*(892)^0$. The vertical axis shows the invariant mass of K^-K^+, the decay products of $\phi(1020)$. The concentration of events around $1020\,\mathrm{MeV}/c^2$ is caused by the $\phi(1020) \to K^-K^+$ decay.

Mode of $D_s^- \to K^-K^+\pi^-$	Parameter	Requirement
$D_s^- \to \phi\pi^-$ $(\phi \to K^-K^+)$	$m(K^-K^+)$	$\in [1000, 1040]\,\mathrm{MeV}/c^2$
	$\mathrm{DLL}_{K\pi}$ of kaons	> -2
$D_s^- \to K^{*0}K^-$ $(K^{*0} \to K^+\pi^-)$		$\notin D_s^- \to \phi\pi^-$
	$m(K^+\pi^-)$	$\in [842, 942]\,\mathrm{MeV}/c^2$
	$\mathrm{DLL}_{K\pi}$ of K^-	> 5
	$\mathrm{DLL}_{K\pi}$ of K^+	> -2
$D_s^- \to (K^-K^+\pi^-)_{\text{non-resonant}}$		$\notin D_s^- \to \phi\pi^-$
		$\notin D_s^- \to K^{*0}K^-$
	$\mathrm{DLL}_{K\pi}$ of kaons	> 5
	$\mathrm{DLL}_{K\pi}$ of pion	< 10

Table 2: The $D_s^- \to K^-K^+\pi^-$ decay can be divided into three modes. This table lists the requirements for each mode.

In this analysis a Boosted Decision Tree (BDT) is used to separate signal from background [27, 28]. A BDT is a multivariate algorithm that uses kinematic and topological variables to assign a number between -1 and 1 to each event. The lower this number the more the event looks like background, while a higher number means that the event looks like signal. The BDT used in this analysis is the same as in Ref. [29]. The BDT is trained using the Run 1 data of $B_s^0 \to D_s^-\pi^+$. Because of the kinematic similarities, the BDT is used for both $B_s^0 \to D_s^-\pi^+$ and $B^0 \to D^-\pi^+$ data. To be able to separate background and signal, all events with an $D_s^-\pi^+$ invariant mass above $5445\,\mathrm{MeV}/c^2$ are labelled as background. Events between 5310 and $5430\,\mathrm{MeV}/c^2$ are

labelled as signal, if they are labelled as signal by the so-called *sPlot* technique [30], which gives weights to events based on their likelihood to be a signal event. In this analysis, events with BDT values above 0.1 are selected.

A few cuts are used in order to specifically cut away certain backgrounds. These cuts are called vetoes. The first veto used in the $D_s^-\pi^+$ sample is the D^0 veto, which requires m(K^+K^-) to be smaller than 1840 MeV/c^2. To remove most of the $B^0 \to D^-\pi^+$ background in the $D_s^-\pi^+$ sample, a D^- veto is used. Since a D^- decays to $K^+\pi^-\pi^-$, one of the pions can be misidentified as a kaon. To reduce the number of these events, the D_s^- candidate is reconstructed under the $K^+\pi^-\pi^-$ mass hypothesis. If the resulting invariant mass is between 1840 and 1900 MeV/c^2, close to the known D^- mass of (1869.59 ± 0.09) MeV/c^2 [2], a strong PID cut, $\mathrm{DLL}_{K\pi} > 10$, is imposed on the kaon with the same charge as the D_s^- candidate. Similarly, a Λ_c^+ veto is imposed to reduce the number of $\Lambda_b^0 \to \Lambda_c^+\pi^-$ ($\Lambda_c^+ \to pK^-\pi^+$) background events in the $D_s^-\pi^+$ sample. To check whether the D_s^- candidate could have been a Λ_c^+, the D_s^- candidate is reconstructed under the $pK^-\pi^+$ mass hypothesis. If the resulting invariant mass is between 2255 and 2315 MeV/c^2, close to the known Λ_c^+ mass of (2286.46 ± 0.14) MeV/c^2 [2], a strong veto is imposed on the same-charge kaon, $\mathrm{DLL}_{K\pi} - \mathrm{DLL}_{p\pi} > 5$, to reduce the amount of protons identified as kaons to a minimum.

The $D^-\pi^+$ sample also has a Λ_c^+ veto, which cuts away most protons misidentified as pions. To do this, the D^- candidates are reconstructed under $pK^-\pi^+$ mass hypothesis. As the Λ_c^+ veto for the $D_s^-\pi^+$ sample, a PID cut is applied to veto the proton, in this case $\mathrm{DLL}_{p\pi} < 0$, if the invariant mass, after changing the mass hypothesis, is between 2255 and 2315 MeV/c^2. To prevent $B^0_{(s)} \to D_s^-\pi^+$ from entering the $D^-\pi^+$ sample, a D_s^- veto is used, in which the D^- candidate is reconstructed under the $K^-K^+\pi^-$ mass hypothesis. Afterwards, a PID cut, $\mathrm{DLL}_{K\pi} < 0$, is imposed on one of the pions, if the D^- candidate has, after changing mass hypothesis, an invariant mass between 1950 and 2030 MeV/c^2, close to the known D_s^- mass of (1968.28 ± 0.10) MeV/c^2 [2].

All the cuts used in the offline selection for the $D_s^-\pi^+$ fit and the $D^-\pi^+$ fit are listed in Tables 3 and 4, respectively.

Description	Requirement
BDT value	> 0.1
$m(D_s^-\pi^+)$	$[5150, 5800]\,\text{MeV}/c^2$
$m(K^-K^+\pi^-)$	$[1930, 2065]\,\text{MeV}/c^2$
$\text{DLL}_{\mu\pi}$ of bachelor pion	< 2
$\text{DLL}_{K\pi}$ of bachelor pion	< 0
D_s^- vertex separation χ^2 w.r.t. B_s^0	> 2
D_s^- lifetime w.r.t. B_s^0	> 0 ps
D^0 veto:	
$m(K^-K^+)$	$< 1840\,\text{MeV}/c^2$
D^- veto:	
pion veto, same-charge kaon	$\text{DLL}_{K\pi} > 10$
or	
D_s^- under $K^+\pi^-\pi^-$ hypothesis	$\notin [1840, 1900]\,\text{MeV}/c^2$
Λ_c^+ veto:	
proton veto, same-charge kaon	$\text{DLL}_{K\pi} - \text{DLL}_{p\pi} > 5$
or	
D_s^- under $pK^-\pi^+$ hypothesis	$\notin [2255, 2315]\,\text{MeV}/c^2$

Table 3: Requirements on the events in the $D_s^-\pi^+$ fit.

Description	Requirement
BDT value	> 0.1
$m(D^-\pi^+)$	$[5000, 5800]\,\text{MeV}/c^2$
$m(K^+\pi^-\pi^-)$	$[1830, 1920]\,\text{MeV}/c^2$
$\text{DLL}_{\mu\pi}$ of bachelor pion	< 2
$\text{DLL}_{K\pi}$ of bachelor pion	< 0
D^- vertex separation χ^2 w.r.t. B^0	> 9
D^- lifetime w.r.t. B^0	> 0 ps
Λ_c^+ veto:	
proton veto, pions	$\text{DLL}_{p\pi} < 0$
or	
D^- under $pK^-\pi^+$ hypothesis	$\notin [2255, 2315]\,\text{MeV}/c^2$
D_s^- veto:	
kaon veto, pions	$\text{DLL}_{K\pi} < 0$
or	
D^- under $K^-K^+\pi^-$ hypothesis	$\notin [1950, 2030]\,\text{MeV}/c^2$

Table 4: Requirements on the events in the $D^-\pi^+$ fit.

3.4 Simulation of data

To be able to compare the data with theory, simulations are made, also called Monte Carlo (MC) data. MC is used in various ways in this analysis. First of all, it is used to make background templates, as explained in Section 4.2. These templates are used to fit

the data. Secondly, MC is used to fit analytical probability density functions (PDFs) to the $B_s^0 \to D_s^- \pi^+$ and $B^0 \to D^- \pi^+$ signals, which is explained in Section 5. Finally, MC is used to compute selection efficiencies, which are used for background yield estimation and for computing the final branching fraction (see Section 1.2).

The first step in generating simulated events is simulating pp collisions. This is done by the program PYTHIA [31] with a specific LHCb configuration [32]. Decays of hadronic particles are described by EVTGEN [33], in which final-state radiation is generated using PHOTOS [34]. The interaction of the generated particles with the detector, and its response, are implemented using the GEANT4 toolkit [35] as described in Ref. [36]. Afterwards, the generated events go through the same selection steps as data. A schematic overview of the resulting production and selection of simulated data can be found in Fig. 6.

3.5 Efficiencies

In the previous sections, all the main steps of the event selection in LHCb are discussed. As discussed in Section 1.2, calculating efficiencies of the event selection for $B^0 \to D_s^+ \pi^-$ and $B^0 \to D^- \pi^+$ is required for calculating the branching fraction of $B^0 \to D_s^+ \pi^-$. Calculating signal efficiencies from data is very challenging, because it is unknown from what decay an event originates. In events from simulation on the other hand, particles are labelled by their true identity. This makes it possible to calculate efficiencies from specific signal decays and compare them.

The efficiencies of all kinematic cuts are determined from simulated signal events, by comparing the number of event before and after applying each cut. The uncertainty on this efficiency is obtained by assuming a normal distribution for the error, while taking the efficiency as a binomially-distributed observation.

The efficiency from the cuts on PID variables, however, is not necessarily well described by MC and can therefore only be used as an approximate evaluation [37]. Therefore, a data-driven tool, `PIDCalib` [37], is used to determine the efficiency of the PID selection. The `PIDCalib` package, widely used within the LHCb Collaboration, provides calibration samples of pions, kaons, protons, electrons, and muons, which are used to make performance histograms for specific PID cuts. These performance histograms are one-, two- or three-dimensional histograms, dependent on particle momentum, pseudorapidity, or the number of tracks in the event (nTracks). These histograms are made for each PID cut and contain weights that indicate the probability of a certain particle to pass this PID cut. In this analysis, two-dimensional performance histograms, dependent on particle momentum and nTracks, are used to calculate the signal efficiency, to reweight the background shapes, and to estimate background yields. An example of these histograms is showed in Fig. 8, while the reweighting histograms for all the PID cuts listed in Tables 3 and 4 are showed in Appendix C. Using these reweighting histograms, and the particle momentum and nTracks variables from MC samples, an efficiency of the PID selection is determined. In order to include the PID cuts from vetoes, described in Section 3.3, the signal MC samples are split according to the PID cuts applied to each event, such that each event in a sample has the same PID selection.

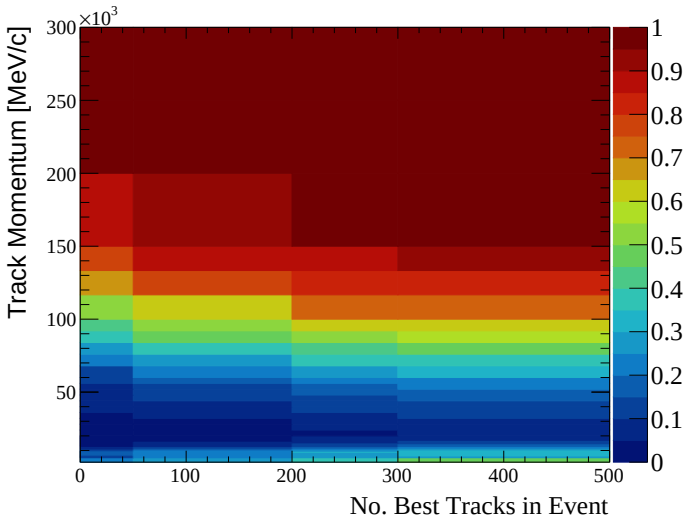

Figure 8: PID reweighting histogram for $\mathrm{DLL}_{K\pi} < -2$ cut on pions, based on the 2012 *MagDown* data. The z-scale of the histogram represents the PID efficiency for this selection criterion.

The efficiencies of the $B^0 \to D_s^+\pi^-$ and $B^0 \to D^-\pi^+$ signals are listed in Tables 5 and 6, respectively. At generator level, cuts are applied to remove events far outside of the LHCb acceptance. When simulating events, this efficiency is reported. The reconstruction and stripping efficiency is determined by comparing the number of events before stripping with the number of true signal events in MC samples. The trigger cuts indicate the efficiency from selecting so-called trigger lines, which are sets of criteria that can select an event in the online trigger selection. Only HLT1 and HLT2 trigger lines are selected to further select events in this analysis. These lines are explained in the description of the HLT1 and HLT2 trigger in Section 3.1. The $D_s^- \to \phi\pi^-$ selection efficiency in Table 5 takes into account the kinematic cuts made to select the $\phi\pi^-$ decay mode. As explained in Section 4.5, the $\phi\pi^-$ decay mode is used in this analysis.

	Run 1		Run2	
Cut	ϵ_{rel} (%)	ϵ_{cum} (%)	ϵ_{rel} (%)	ϵ_{cum} (%)
Generator level efficiency	17.405 ± 0.021	17.405 ± 0.021	18.02 ± 0.04	18.02 ± 0.04
Reconstruction and stripping	3.768 ± 0.006	0.6558 ± 0.0013	4.506 ± 0.006	0.8120 ± 0.0021
Trigger cuts	94.26 ± 0.09	0.6182 ± 0.0014	98.23 ± 0.05	0.7976 ± 0.0021
B^0 mass window cuts	98.04 ± 0.06	0.6060 ± 0.0014	98.03 ± 0.05	0.7819 ± 0.0021
$D_s^\pm$ mass window cuts	99.26 ± 0.04	0.6016 ± 0.0014	99.229 ± 0.034	0.7758 ± 0.0021
Vertex separation cuts	88.03 ± 0.14	0.5296 ± 0.0015	86.10 ± 0.14	0.6680 ± 0.0021
Lifetime cut	98.38 ± 0.06	0.5210 ± 0.0015	98.61 ± 0.05	0.6587 ± 0.0021
BDT cuts	96.03 ± 0.09	0.5003 ± 0.0015	97.49 ± 0.07	0.6422 ± 0.0021
$D_s^\pm \to \phi\pi^\pm$ selection	41.24 ± 0.23	0.2063 ± 0.0013	41.52 ± 0.21	0.2666 ± 0.0016
PID cuts	74.3541 ± 0.0019	0.1534 ± 0.0010	75.5458 ± 0.0008	0.2014 ± 0.0012

Table 5: Efficiencies of the $B^0 \to D_s^+\pi^-$ signal.

	Run 1		Run2	
Cut	ϵ_{rel} (%)	ϵ_{cum} (%)	ϵ_{rel} (%)	ϵ_{cum} (%)
Generator level efficiency	16.56 ± 0.09	16.56 ± 0.09	17.233 ± 0.033	17.233 ± 0.033
Reconstruction and stripping	3.7343 ± 0.0034	0.6184 ± 0.0034	4.2599 ± 0.0025	0.7341 ± 0.0015
Trigger cuts	94.14 ± 0.05	0.5821 ± 0.0032	96.602 ± 0.029	0.7092 ± 0.0014
B^0 mass window cuts	99.355 ± 0.019	0.5784 ± 0.0032	99.276 ± 0.014	0.7040 ± 0.0014
$D^{\pm}$ mass window cuts	98.518 ± 0.029	0.5698 ± 0.0032	98.266 ± 0.021	0.6918 ± 0.0014
Vertex separation cuts	86.79 ± 0.08	0.4946 ± 0.0028	84.04 ± 0.06	0.5814 ± 0.0013
Lifetime cut	99.927 ± 0.007	0.4942 ± 0.0028	99.939 ± 0.004	0.5810 ± 0.0013
BDT cuts	95.98 ± 0.05	0.4743 ± 0.0027	97.448 ± 0.029	0.5662 ± 0.0012
PID cuts	75.23348 ± 0.00035	0.3569 ± 0.0020	77.14862 ± 0.00016	0.4368 ± 0.0010

Table 6: Efficiencies of the $B^0 \to D^- \pi^+$ signal.

4 Backgrounds in the mass distribution

In the invariant mass fits of both $D_s^-\pi^+$ and $D^-\pi^+$ candidates, common types of backgrounds can be distinguished. Three types of backgrounds are separated:

Partially reconstructed backgrounds These backgrounds arise if $B^0_{(s)}$ mesons decay to excited states of $D^\pm_{(s)}$ mesons or pions. These excited mesons immediately eject photons or neutral pions, which are not reconstructed in the $D^-_{(s)}\pi^+$ data. These unreconstructed particles cause the partially reconstructed background events to have a lower invariant mass than the $B^0_{(s)} \to D^-_{(s)}\pi^+$ signal. This is visible in Fig. 9, where the partially reconstructed backgrounds $B^0 \to D^-\rho^+$ ($\rho^+ \to \pi^+\pi^0$) and $B^0 \to D^{*-}\pi^+$ ($D^{*-} \to D^-\pi^0$) are fitted to the data.

Misidentified backgrounds If one of the final-state particles in certain decays gets misidentified, the event ends up being reconstructed under an incorrect mass hypothesis as $D^-_{(s)}\pi^+$ candidate. These backgrounds are called misidentified backgrounds. An example of a misidentified background is $B^0 \to D^-K^+$, in which the kaon is identified as a pion.

Combinatorial background This background consists of random combinations of the final-state particles, resulting in $D^-_{(s)}\pi^+$ candidates. This can happen in two ways. The D^- (D_s^-) candidate can be reconstructed from random combinations of its final-state particles $K^+\pi^-\pi^-$ ($K^-K^+\pi^-$), but can also be a true D^- (D_s^-) meson that decayed to $K^+\pi^-\pi^-$ ($K^-K^+\pi^-$), combined randomly with a pion. In this analysis, these events are called "true $D^-_{(s)}$ combinatorial background" events. Another possibility is that a D^- (D_s^-) candidate is reconstructed from a random combination of $K^+\pi^-\pi^-$ ($K^-K^+\pi^-$) and is randomly combined with a pion. Throughout this analysis, these events are called "random $D^-_{(s)}$ combinatorial background". In this analysis, only in the $D_s^-\pi^+$ mass fits, the combinatorial background is split between true and random $D^-_{(s)}$ combinatorial, as described in Section 4.4.

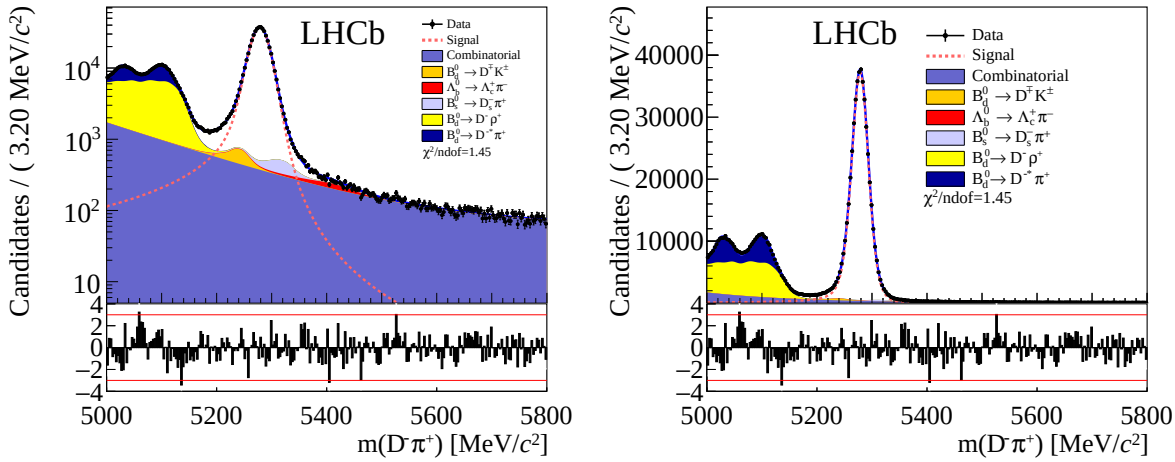

(a) logarithmic vertical axis

(b) linear vertical axis

Figure 9: The $B^0 \to D^-\pi^+$ signal with corresponding backgrounds using Run 1 data. The $B^0 \to D^{*-}\pi^+$ and $B^0 \to D^-\rho^+$ decays are partially reconstructed backgrounds and the $B^0 \to D^-K^+$, $B^0_s \to D^-_s\pi^+$, and $\Lambda^0_b \to \Lambda^+_c\pi^-$ decays are misidentified backgrounds.

4.1 Likelihood fit

In order to determine the yields of the $B^0 \to D^+_s\pi^-$ and $B^0 \to D^-\pi^+$ signals, shapes of both signals and backgrounds are fitted to data, using a likelihood fit to the invariant mass distributions.

Since a lot of free parameters are involved in these invariant mass fits, using a dedicated framework is sensible. The framework used in this analysis is called `B2DXFitters`. The `B2DXFitters` package contains scripts written in Python and C++, which enable multidimensional fits, *i.e.* fits in multiple variables, to be used. The fitting process itself is performed by RooFit [38], which estimates all the free parameters in the fit by maximising the likelihood function. The likelihood is defined as

$$L(\vec{\theta}|\vec{x}) = \prod_{i=1}^{n} P(x_i|\vec{\theta}), \tag{17}$$

where $\vec{\theta}$ are the free parameters in the fit, $\vec{x}$ represents the data and P is a probability density function (PDF). This function is maximised to in order to find values for the free parameters that describe data the best.

It is possible to constrain a parameter to be around a certain value, *e.g.* a theory prediction. This is done by adding a Gaussian term to the likelihood function. Consequently, the maximum of the likelihood function, including the Gaussian term, is shifted towards the mean of this Gaussian term. This extra term that is added to the likelihood function is called a Gaussian Constraint (GC) and the parameter that is constrained by this term is called a Gaussian-constrained parameter.

4.2 Background templates

The backgrounds in the invariant mass fits are described by shapes obtained from simulation. These non-parametric templates are called RooKeys PDFs [39]. Firstly, all kinematic

cuts are applied to the MC sample, as described in Section 3.3. Afterwards, the MC is corrected for the differences in particle momentum and nTracks distributions relative to data, using the same correction as Ref. [29]. Since PID variables are not well described in MC, as explained in Section 3.5, the MC samples are reweighted by histograms made using `PIDCalib`. Appendix C shows the PID reweighting histograms corresponding to the PID cuts from Section 3.3. Using the remaining weighted events, a RooKeys PDF is made. To make a RooKeys PDF, each event is described by a Gaussian distribution and summed to form a distribution. To smoothen this distribution, the parameter ρ is defined. A high value of ρ will make the distribution smooth, while a low value of ρ preserves sharper and more detailed structures. An example of a background template is showed in Figure 10, while all the templates are showed in Appendix D.

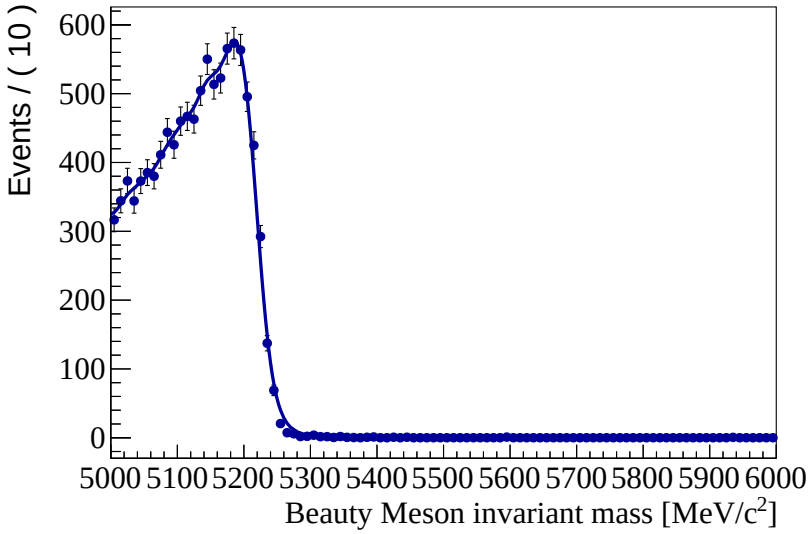

Figure 10: Background template of $B_s^0 \to D_s^- \rho^+$ decay, which is used for $D_s^- \pi^+$ mass fit. The data points represent weighted 2012 MC, while the line represents the RooKeys PDF.

4.3 Background yields

The misidentified backgrounds are backgrounds in which one of the final-state particles gets misidentified. These events will end up around the signal peak, *i.e.* $B_s^0 \to D_s^- \pi^+$ or $B^0 \to D^- \pi^+$, as shown in Figure 9. To prevent the misidentified backgrounds from changing the signal shape, a GC is used to constrain the relative yield in the fit to an expected value. The $B^0 \to D^- \pi^+$ background in the $D_s^- \pi^+$ fit, on the other hand, is fixed to its expected relative yield, due to the low number of expected events.

Table 7 shows the yields of all be misidentified backgrounds relative to either the $B_s^0 \to D_s^- \pi^+$ or $B^0 \to D^- \pi^+$ signal. These relative yields are calculated using MC samples and PID reweighting histograms.

Firstly, the kinematic cuts, as described in Section 3.3, are applied to the MC of the backgrounds, to calculate the relative offline selection efficiency. Afterwards, all the remaining events are weighted using PID reweighting histograms for the corresponding PID cuts, including vetoes. Finally, the relative yield is calculated,

$$\text{Relative Yield} = \frac{N_{\text{background}}}{N_{\text{signal}}} = \frac{\mathcal{B}(\text{signal})}{\mathcal{B}(\text{background})} \frac{\epsilon_{\text{signal}}}{\epsilon_{\text{background}}} f_{\text{Hadronisation}}, \tag{18}$$

where $\mathcal{B}$ stands for the branching fraction of the signal or background, also including branching fractions of child decays, *e.g.* $\mathcal{B}(D_s^- \to K^-K^+\pi^+)$, ϵ_{signal} and $\epsilon_{\text{background}}$ are the total efficiency of the signal and background, respectively, and $f_{\text{Hadronisation}}$ is the hadronisation fraction. This hadronisation fraction takes into account the different production rates of B^0, B_s^0 and Λ_b^0 hadrons [40, 41].

Fit	Decay	Data	$\mathcal{B}/10^{-4}$	Had. frac.	Gen. level	Rec. and strip.	Rel. offline sel.	PID	Rel. yield
$D_s^-\pi^+$	$B_s^0 \to D_s^-\pi^+$	Run 1	30 ± 2	0.25 ± 0.02	0.1739 ± 0.0003	0.03855 ± 0.00004	1.000	0.7408	1.0
		Run 2			0.1800 ± 0.0004	0.04631 ± 0.00004	1.000	0.7505	1.0
	$B_s^0 \to D_s^-K^+$	Run 1	2.3 ± 0.2	0.25 ± 0.02	0.1773 ± 0.0006	0.03786 ± 0.00004	0.953	0.1020	0.0090 ± 0.0010
		Run 2			0.1836 ± 0.0004	0.04990 ± 0.00009	0.941	0.1125	0.0096 ± 0.0011
	$\Lambda_b^0 \to \Lambda_c^+\pi^-$	Run 1	49 ± 4	0.36 ± 0.02	0.1746 ± 0.0004	0.02612 ± 0.00005	0.023	0.0342	0.0020 ± 0.0003
		Run 2			0.1819 ± 0.0005	0.03064 ± 0.00007	0.018	0.0073	0.0003 ± 0.0001
	$B^0 \to D^-\pi^+$	Run 1	25 ± 1	1.0	0.1656 ± 0.0007	0.03734 ± 0.00003	0.031	0.0078	0.0017 ± 0.0002
		Run 2			0.1723 ± 0.0004	0.04328 ± 0.00003	0.032	0.0054	0.0011 ± 0.0001
$D^-\pi^+$	$B^0 \to D^-\pi^+$	Run 1	25 ± 1	1.0	0.1656 ± 0.0007	0.03734 ± 0.00003	1.000	0.7416	1.0
		Run 2			0.1723 ± 0.0004	0.04328 ± 0.00003	1.000	0.7572	1.0
	$B^0 \to D^-K^+$	Run 1	1.9 ± 0.2	1.0	0.1688 ± 0.0002	0.03661 ± 0.00007	0.975	0.102	0.0091 ± 0.0011
		Run 2			0.1756 ± 0.0004	0.04137 ± 0.00003	0.978	0.1121	0.0096 ± 0.0012
	$\Lambda_b^0 \to \Lambda_c^+\pi^-$	Run 1	49 ± 4	0.36 ± 0.02	0.1746 ± 0.0004	0.02612 ± 0.00005	0.307	0.0596	0.0090 ± 0.0012
		Run 2			0.1819 ± 0.0005	0.03064 ± 0.00007	0.292	0.0219	0.0033 ± 0.0004
	$B_s^0 \to D_s^-\pi^+$	Run 1	30 ± 2	0.25 ± 0.02	0.1739 ± 0.0003	0.03856 ± 0.00004	0.491	0.0635	0.0084 ± 0.0010
		Run 2			0.1800 ± 0.0004	0.04631 ± 0.00004	0.491	0.0668	0.0088 ± 0.0011

Table 7: Background estimation of misidentified backgrounds in $D_s^-\pi^+$ and $D^-\pi^+$ fits. The column Had. frac. is the hadronisation fraction relative to B^0 mesons. Gen. level is the Generator level cut efficiency and Rec. and strip. is the reconstruction and stripping efficiency, as described in Section 3.5. Rel. offline sel. stands for the relative offline selection efficiency, the efficiency of applying all offline kinematic cuts to the MC samples, as listed in Section 3.3, relative to either the $B_s^0 \to D_s^-\pi^+$ or $B^0 \to D^-\pi^+$ signal efficiency. PID is the probability of (mis)identifying the decay as final-state particles of either $D_s^-\pi^+$ or $D^-\pi^+$. Rel. yield is the yield of the decay divided by the yield of either the $B_s^0 \to D_s^-\pi^+$ or $B^0 \to D^-\pi^+$ signal.

4.4 Combinatorial background study

In the beginning of this chapter, the difference between random and true D_s^- combinatorial background is explained. To be able to constrain the combinatorial background in the mass fit with $D_s^-\pi^+$ candidates, it is useful to split it. To split the combinatorial background between random and true D_s^- combinatorial, a two-dimensional fit is needed. Beside $D_s^-\pi^+$ mass fit, a fit of the $K^-K^+\pi^-$ mass is made. These fits are done simultaneously and share all the background and signal yields.

Fig. 11 shows the invariant mass plot of the D_s^- candidates, with all components displayed in the legend. In the $K^-K^+\pi^-$ invariant mass fit, the shape of the random D_s^- combinatorial background is described by an exponential function, while the true D_s^- combinatorial background, the $B_s^0 \to D_s^-\pi^+$ and $B^0 \to D_s^+\pi^-$ signal shapes and the partially reconstructed backgrounds are modelled with a double Crystal Ball (DCB) function, which is defined in Appendix B and further explained in Section 5.1. The parameters of the DCB distribution are obtained from the $B_s^0 \to D_s^-\pi^+$ MC fit in the $K^-K^+\pi^-$ invariant mass. In fits to data, the widths σ_1 and σ_2 are left free with a fixed ratio. The shapes of the misidentified backgrounds ($B^0 \to D^-\pi^+$, $B_s^0 \to D_s^-K^+$, and $\Lambda_b^0 \to \Lambda_c^+\pi^-$) are modelled by background templates, as explained in Section 4.2.

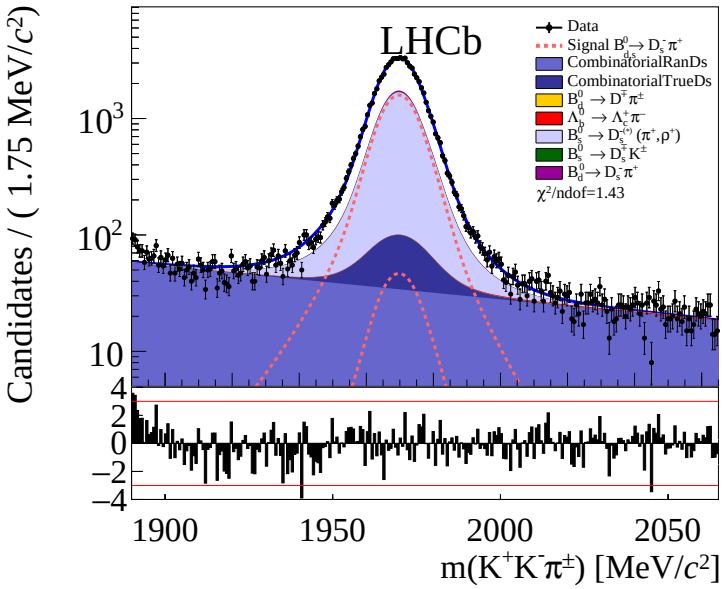

Figure 11: Fit to the $K^-K^+\pi^-$ invariant mass using Run 1 data. The vertical axis is displayed in logarithmic scale.

As can be seen in Fig. 11, the random D_s^- combinatorial background does not show a peaking structure, because it is composed of random combinations of $K^-K^+\pi^-$. A wide range of $m(K^-K^+\pi^-)$ makes the random D_s^- combinatorial background easier to constrain by the fit. However, naively changing the mass window is not sensible; there might be structures of other decays in the sidebands. This means that these decays should either be included in the fit or cut out. In Section 4.5 the sidebands of D_s^- are studied to check whether it is feasible to expand the mass window.

In the invariant mass window of the $D_s^-\pi^+$ candidates the random D_s^- combinatorial

background is modelled with an exponential distribution. This follows from results of the D_s^- sideband study in Section 4.5. Thanks to the two-dimensional fit, the yield of this background is well-constrained.

The true D_s^- combinatorial background is harder to constrain from the fit. In the two-dimensional fit to the $D_s^-\pi^+$ and $K^-K^+\pi^-$ invariant mass, the true D_s^- combinatorial background overlaps with other backgrounds. The true D_s^- combinatorial background in the D_s^- mass fit is described by the $B_s^0 \to D_s^-\pi^+$ signal shape with a separate factor R to scale the widths σ_1 and σ_2, while keeping their ratio fixed. In the B_s^0 mass fit the true D_s^- combinatorial background is described by an exponential plus a constant,

$$f(m, p_1, f_1) \propto f_1 e^{p_1 m} + (1 - f_1). \tag{19}$$

This shape is chosen based on a comparison between fits with the true D_s^- combinatorial described by an exponential, an exponential plus a constant, and a double exponential distribution. The exponential distribution was not able to result in stable fits, while the double exponential converged with one of the exponential parameters almost zero, making it almost an exponential plus constant distribution.

4.5 Peaking backgrounds from other B decays

A sideband study is done to check whether it is feasible to expand the D_s^- mass window, in order to constrain the random D_s^- combinatorial background. Also, the contribution of other B decays, not containing a D_s^- meson, can be estimated. The available range of $m(K^-K^+\pi^-)$ is from 1885 to 2065 MeV/c^2. Within this range, two sideband regions are defined: the lower sideband from 1885 to 1890 MeV/c^2 and the upper sideband from 2030 to 2065 MeV/c^2. All three D_s^- decay modes, as defined in Section 3.3, and both mass regions are studied separately. This results in the $D_s^-\pi^+$ invariant mass fits in Figs. 12 and 14 for the lower and upper sideband, respectively.

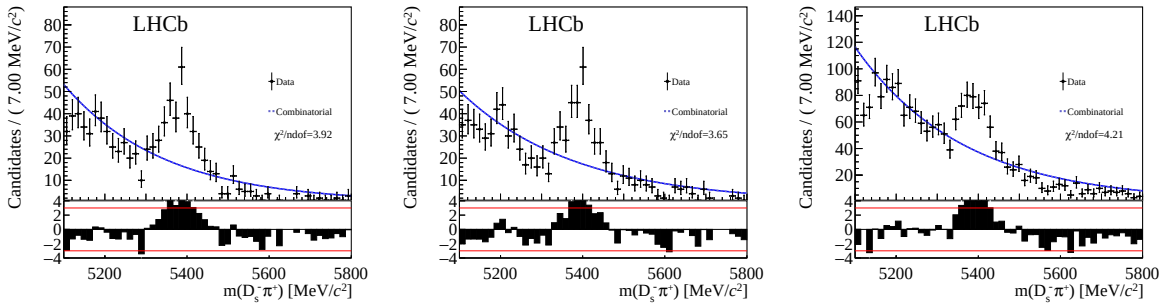

(a) $\phi\pi^-$ (b) $K^{*0}K^-$ (c) non-resonant

Figure 12: Fits to the $D_s^-\pi^+$ invariant mass, selecting only the lower D_s^- sideband ([1885,1890] MeV/c^2) and selecting the three D_s^- decay modes separately. These fits are made with Run 1 data.

In Fig. 12 a clear peak is visible around 5400 MeV/c^2, in all three D_s^- modes. Since a variable is used that uses a constrained D_s^- invariant mass to calculate the B_s^0 mass, the mass peak is shifted with respect to the unconstrained B_s^0 mass. Using the invariant mass from combining all four final-state particles without constraints, the mass peak shifts

to the left. A Gaussian distribution is fitted to the this peak on top of an exponential distribution, representing the combinatorial background. The resulting fit and parameters are shown in Fig. 13 and Table 8, where p_1 is the parameter of the exponential distribution and the mean μ and width σ are the parameters of the Gaussian distribution.

The observed peak is caused by genuine $D^- \to K^-K^+\pi^-$ decays. In the lower tail in Fig. 11 an increase in events is visible. This is a tail of $D^- \to K^-K^+\pi^-$ decays, which peaks around the D^- mass of $(1869 \pm 0.09)\,\mathrm{MeV}/c^2$. The branching fraction $\mathcal{B}(D^- \to K^-K^+\pi^-) = (9.96 \pm 0.26) \times 10^{-3}$ is comparable in size to $\mathcal{B}(D_s^- \to K^-K^+\pi^-) = (5.45 \pm 0.17) \times 10^{-3}$, the signal peak [2].

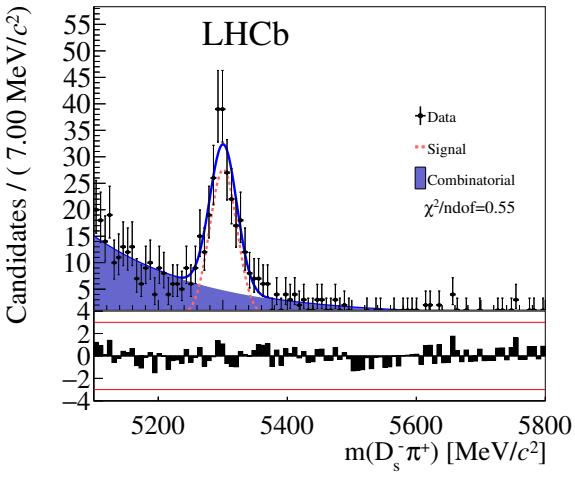

Figure 13: Mass fit of $D_s^-\pi^+$ candidates of Run 1 $\phi\pi^-$ data in the lower D_s^- sideband ranging from 1885 to 1890 MeV/c^2.

Parameter	Fit result
μ	5300.8 ± 1.98
σ	21.06 ± 1.98
p_1	$(-5.67 \pm 0.36) \times 10^{-3}$
N_{Signal}	208.1 ± 18.2
$N_{\mathrm{Combinatorial}}$	368.9 ± 22.2

Table 8: Fit results corresponding to the fit in Fig. 13.

These results do not agree with the B^0 mass of $(5279.62 \pm 0.15)\,\mathrm{MeV}/c^2$, which would correspond to $B^0 \to D^-\pi^+$ ($D^- \to K^-K^+\pi^-$). However, only a part of the right tail is included in the data, which explains the shift of the mean to above the B^0 mass.

Thus, the lower sideband of the invariant mass histogram of $K^-K^+\pi^-$ candidates contains a background coming from genuine $D^- \to K^-K^+\pi^-$ decays. To remove these events, the $K^-K^+\pi^-$ invariant mass is required to be above $1930\,\mathrm{MeV}/c^2$, far from the D^- mass.

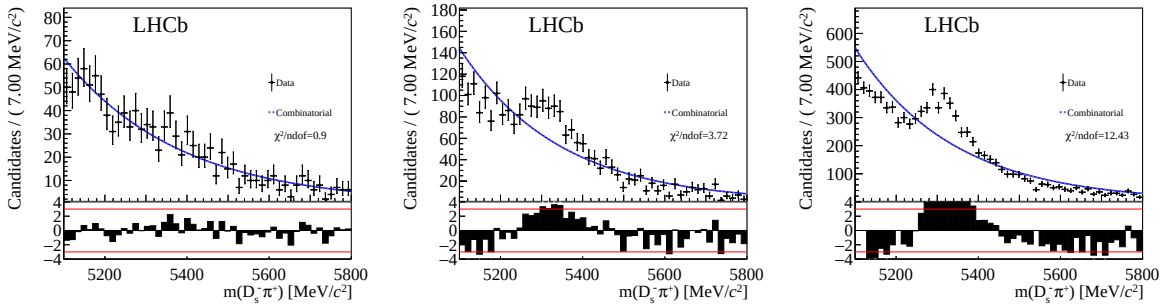

(a) $\phi\pi^-$ (b) $K^{*0}K^-$ (c) non-resonant

Figure 14: Fits to the Run 1 $D_s^-\pi^+$ invariant mass selecting only the upper D_s^- sideband ([2030,2065] MeV/c^2) and selecting the three D_s^- decay modes separately. These fits are made with Run 1 data.

In the $D_s^-\pi^+$ mass using only the upper D_s^- sideband (see Fig. 14), we see a clear difference between the three D_s^- modes. The $\phi\pi^-$ mode in Fig. 14a shows good agreement with an exponential distribution. This means that the upper sideband in the $\phi\pi^-$ mode is dominated by random D_s^- combinatorial background and we can expand the range of the D_s^- invariant mass up to 2065 MeV/c^2 for $\phi\pi^-$.

The other D_s^- modes, $K^{*0}K^-$ and non-resonant, do not follow an exponential distribution and show a peaking structure around 5300 MeV/c^2. This means that another background is present. To check whether this could be misidentified $B^0 \to D^-\pi^+$ or $\Lambda_b^0 \to \Lambda_c^+\pi^-$ events, the D^- and Λ_c^+ vetoes, defined in Section 3.3, are tightened. Instead of applying a strong PID cut for events with a D_s^- candidate around the D^- or Λ_c^+ mass (in the corresponding mass hypotheses), these events are removed. This also cuts away a lot of signal, so using these cuts outside of this D_s^- sideband study is not considered. The stricter D^- veto cuts away a big part of the peaks from Figs. 14b and 14c. This means that a large part of this peak is coming from misidentified $B^0 \to D^-\pi^+$ events. The stricter Λ_c^+ veto, on the other hand, does not cut away much data. After these stricter cuts, a peaking structure remains visible for the $K^{*0}K^-$ mode and to a lesser extent also for the non-resonant mode. Applying other cuts regarding PID, lifetime, vertex separation, or a veto for misidentified $D_s^- \to K^-\pi^+\pi^-$ events also do not reduce this peak.

Taking this unexplained structure into account, the decision is made to only use the $\phi\pi^-$ mode in this analysis. The behaviour of this mode in the D_s^- sidebands is as expected, and is described by an exponential distribution.

5 Signal shape

As shown in Section 1.2 and Fig. 3, the signal peak originating from $B_s^0 \to D_s^- \pi^+$, on the right side of $B^0 \to D_s^+ \pi^-$, dominates the invariant mass fit and overlaps the $B^0 \to D_s^+ \pi^-$ signal peak. Therefore, it is essential to understand the shape of $B_s^0 \to D_s^- \pi^+$ to be able to determine the yield of $B^0 \to D_s^+ \pi^-$ decays correctly. The signal shape of $B^0 \to D^- \pi^+$ is also studied in this analysis. In the first place because $B^0 \to D^- \pi^+$ is used as the normalisation channel in this analysis. Moreover, the signal peak of $B^0 \to D^- \pi^+$ is very clean compared to $B_s^0 \to D_s^- \pi^+$. This allows us to get some parameters directly from the data fit.

The strategy to determine the signal shape of $B_s^0 \to D_s^- \pi^+$ is to first study several probability density functions (PDFs), which are discussed in Section 5.1. After choosing a suitable PDF, fits to MC samples of both $B^0 \to D^- \pi^+$ and $B_s^0 \to D_s^- \pi^+$ decays are made. The difference between the signal shape fits of these two decays is studied in detail, in particular the left tail parameters. This can be found in Section 5.2. Fits to the $B^0 \to D^- \pi^+$ data are done, using parameters from the MC, while letting some of them free. The difference between MC and data is used together with the difference between $B^0 \to D^- \pi^+$ and $B_s^0 \to D_s^- \pi^+$, to constrain the signal shape used in the $B_s^0 \to D_s^- \pi^+$ data fit.

5.1 Determining the probability density function

Since the $B_s^0 \to D_s^- \pi^+$ signal is much larger than the $B^0 \to D_s^+ \pi^-$ signal, it is important to describe the this signal as accurately as possible. To do this, four PDFs are considered to describe the signal shape of $B_s^0 \to D_s^- \pi^+$ and $B^0 \to D^- \pi^+$:

Double Crystal Ball (DCB) The DCB distribution consists of two Crystal Ball functions with a common mean. A double Crystal Ball function is a PDF with a Gaussian core and exponential tails on either side. By adding two exponential tails to a Gaussian distribution, it is possible to describe the detector resolution and radiative losses of the $B_{(s)}^0$ or $D_{(s)}^-$ meson decays.

Ipatia The Ipatia function is a PDF with exponential tails like a DCB, but the core follows a hyperbolic distribution rather than a Gaussian, to take per-event uncertainties on the measured mass into account [42].

Ipatia plus Gaussian (IpGa) A Gaussian can be added to the Ipatia distribution, to give more freedom to the core of the distribution. The Ipatia and Gaussian share their mean.

Ipatia plus Johnson SU (IpJo) To add more freedom to the core of the invariant mass distribution, a Johnson SU function is added to the Ipatia function. The Johnson SU function is a function with highly asymmetric tails [43]. The combination of the Johnson SU function and an Ipatia is also used as signal shape in Ref. [44].

The definitions of the Gaussian, the Crystal Ball, the Ipatia, and the Johnson SU distributions can be found in Appendix B.

To get an idea of how these PDFs perform, all four are fitted to Run 1 MC of $B^0 \to D^- \pi^+$ and $B_s^0 \to D_s^- \pi^+$. In Fig. 15 the fits to $B^0 \to D^- \pi^+$ MC are presented in a

mass histogram with the $D^-\pi^+$ invariant mass ranging from 5000 to 6000 MeV/c^2. In order to have an indication of how good the fit is per region, a pull diagram is displayed underneath the fit. Furthermore, a reduced χ^2 is calculated to give an estimate of the global goodness of the fit. All parameters in these fits are left free, except the Ipatia parameters β and ζ, which are set to zero.

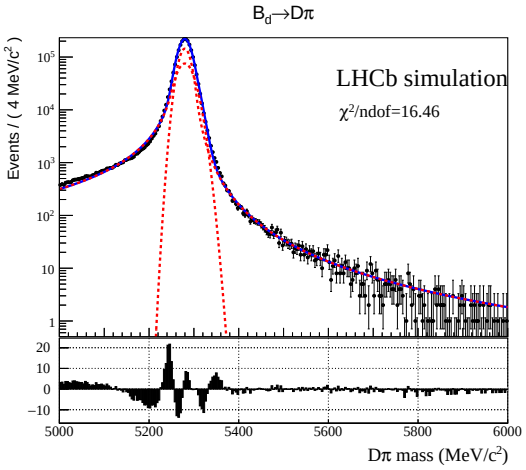

(a) Double Crystal Ball

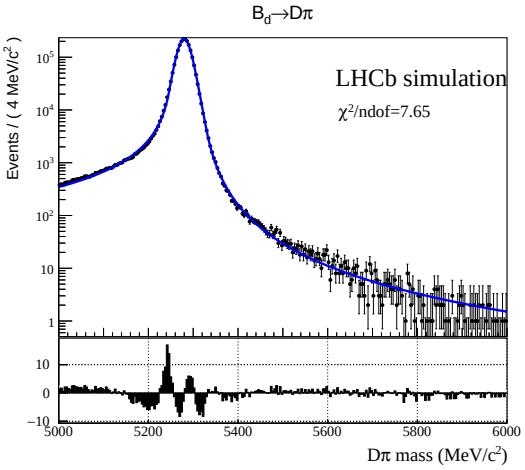

(b) Ipatia

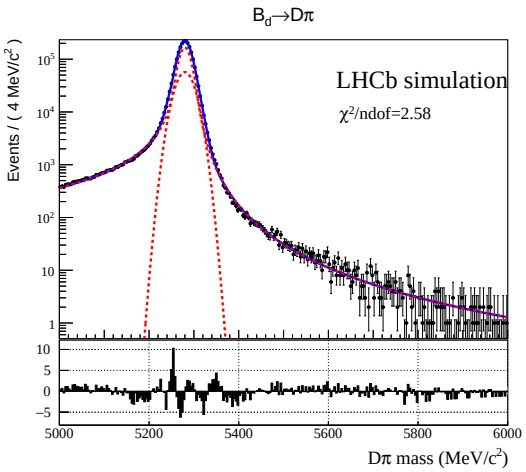

(c) Ipatia plus Gaussian

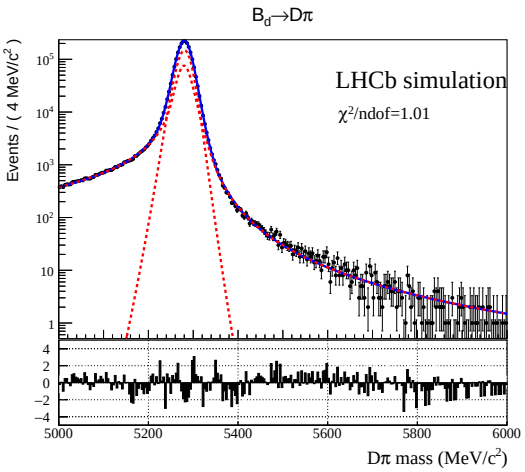

(d) Ipatia plus Johnson SU

Figure 15: Fits to the Run 1 $B^0 \to D^-\pi^+$ Monte Carlo sample with various probability density functions, as explained in the text.

In Fig. 15a a fit using a double Crystal Ball function is shown. This fit has a sizeable pattern in the pull diagram near the peak of the distribution. Just left of the peak, a disagreement between the fitted PDF and the MC of more than 20 standard deviations (20σ) is observed. Other, more complex functions are used to improve the result of the fit. An Ipatia distribution is used in Fig. 15b. This fit has a better reduced χ^2 than the DCB, but has the same pattern in the pull left of the peak. In Fig. 15c the fit is done with an IpGa. The fit agrees better with data, but not not sufficiently, as a 10σ deviation is observed in the pull. Finally, an IpJo is used to fit the MC signal. Fitting this function gives a PDF that agrees with data very well, based on both the pull diagram and the

reduced χ^2. Based on the fits to $B^0 \to D^- \pi^+$ MC, an IpJo is the PDF chosen to model the signal. The fitted parameters of the four fits in Fig. 15 can be found in Appendix A.1.

The PDFs described above are also used in fits to $B_s^0 \to D_s^- \pi^+$ MC. Like the fit to $B^0 \to D^- \pi^+$ MC, all parameters except β and ζ are floating and the invariant mass ranges from 5000 to 6000 MeV/c^2. The results of these fits are shown in Fig. 16.

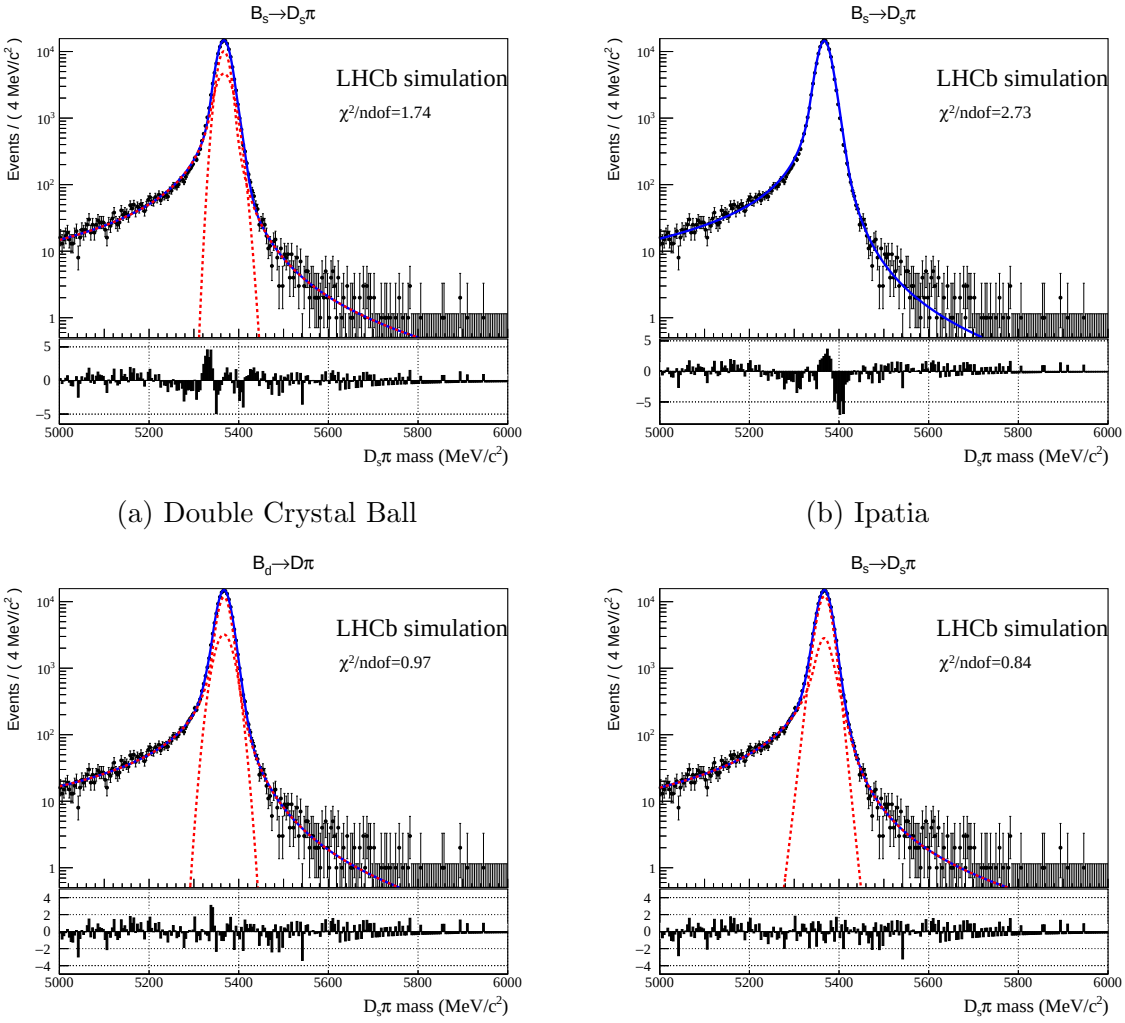

(a) Double Crystal Ball

(b) Ipatia

(c) Ipatia plus Gaussian

(d) Ipatia plus Johnson SU

Figure 16: Fits to the Run 1 $B_s^0 \to D_s^- \pi^+$ Monte Carlo sample with various probability density functions.

The fits to $B_s^0 \to D_s^- \pi^+$ MC in Fig. 16 show better agreement between the fitted PDF and the MC than fits to $B^0 \to D^- \pi^+$ MC. Statistically, this is expected, as the number of events in the $B_s^0 \to D_s^- \pi^+$ MC is smaller than in $B^0 \to D^- \pi^+$ MC. The fits using the DCB and Ipata distribution (Fig. 16a and 16b) show a sizeable pattern in the pull around the peak of the distribution. The IpGa and the IpJo distributions show a better agreement between MC and the fitted PDF, based on both the pull diagram and the reduced χ^2. Appendix A.3 shows the fit parameters belonging to the fits in Fig. 16.

Combining the results of the fits to $B^0 \to D^- \pi^+$ and $B_s^0 \to D_s^- \pi^+$ MC, a decision is made to use the IpJo as signal shape PDF. This PDF is used to describe the $B^0 \to D^- \pi^+$

signal, the $B_s^0 \to D_s^- \pi^+$ signal, as well as the $B^0 \to D_s^+ \pi^-$ signal. The $B^0 \to D_s^+ \pi^-$ signal shape is defined to be the same as the $B_s^0 \to D_s^- \pi^+$ shape, except it is shifted to the left by $87.26\,\text{MeV}/c^2$, which equals the difference between the B^0 and B_s^0 masses [2].

5.2 Shapes from Monte Carlo

The next step is to use the IpJo function to fit the MC, in order to extract shape parameters that are usable in the fits to data. In doing this, the focus is on the left tail of the distribution. This tail is caused by the emission of photons and is often called the *radiative tail*. Studying the left tail of the PDF of the signal shape is important, since the left tail is much larger than the right tail of the signal. On top of that, the $B^0 \to D_s^+ \pi^-$ signal is on the left side of $B_s^0 \to D_s^- \pi^+$, and is therefore sensitive to its shape. The Ipatia part of the IpJo distribution is dominating in both tails, while the Johnson SU part of the distribution is dominating in the peak of the distribution. This means that the Ipatia parameters, in particular a_1 and n_1, are most important regarding the left tail of the distribution. A large correlation between a_1 and n_1 makes it necessary to fix one of them and leave the other free. Because of the number of free parameters together with the large correlation between a_1 and n_1, the value of n_1 is fixed to 1.25, empirically based on preliminary fit results in MC. Fixing n_1 makes it possible to compare the left tail of the distribution based on the value of a_1.

One observation while fitting the $B^0 \to D^- \pi^+$ MC is that the fitted Run 1 distribution does not agree with the 2011 and 2012 distributions. This is shown by using the parameters from the Run 1 fit and superimposing them on the 2011 and 2012 MC, as can be seen Fig. 17. This is possibly caused by the difference in centre-of-mass energy between 2011 and 2012, $\sqrt{s} = 7\,\text{TeV}$ and $\sqrt{s} = 8\,\text{TeV}$. The number of events also makes the fit very sensitive to small differences. This difference is not observed between 2015 and 2016 MC, which are both simulated using a centre-of-mass energy of $\sqrt{s} = 13\,\text{TeV}$, nor in $B_s^0 \to D_s^- \pi^+$ MC, which has fewer events. Because of this difference between 2011 and 2012, $B^0 \to D^- \pi^+$ fits of these years are done separately, while having only one fit for Run 2 and for $B_s^0 \to D_s^- \pi^+$.

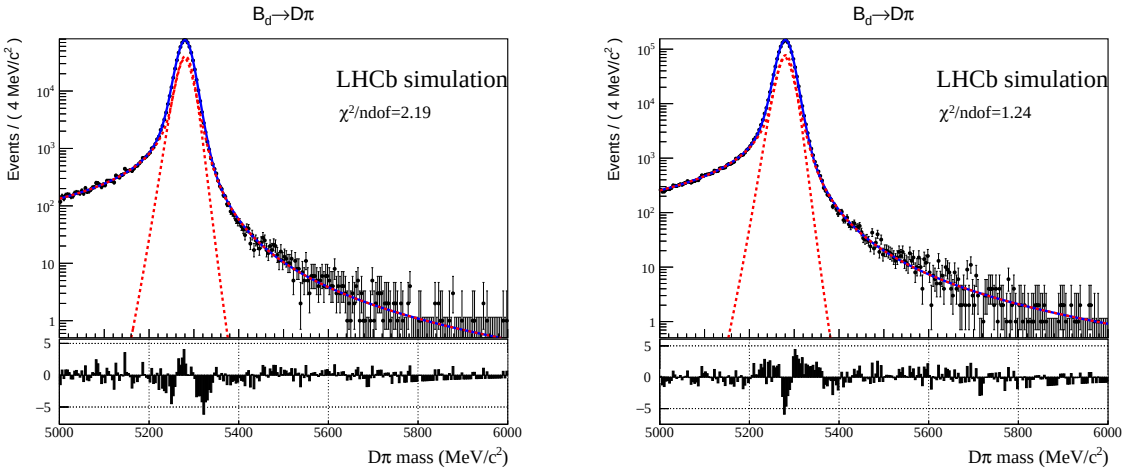

(a) 2011 (b) 2012

Figure 17: Fit results of Run 1 Monte Carlo superimposed on 2011 and 2012 Monte Carlo.

Using a fixed value of n_1, fits are done to 2011, 2012, and Run 2 $B^0 \to D^-\pi^+$ MC, as can be seen in Fig. 18. In these fits all parameters are floating, except n_1, β, and ζ.

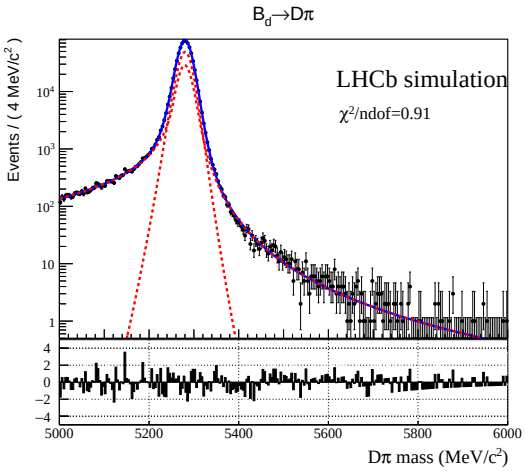

(a) 2011

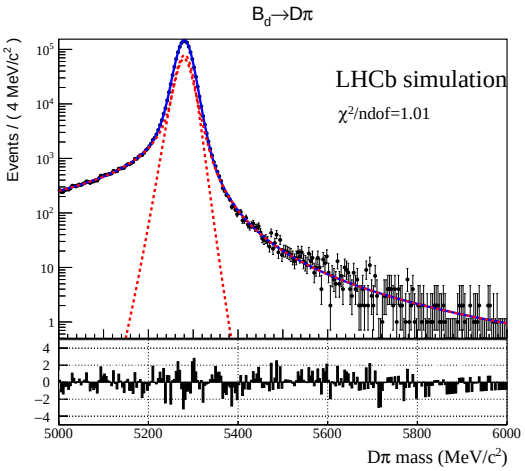

(b) 2012

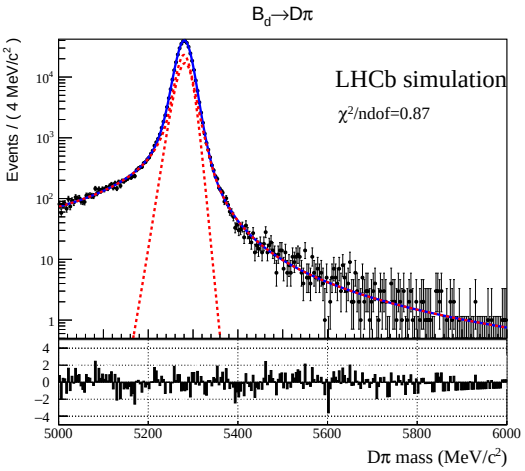

(c) Run 2

Figure 18: IpJo fits to 2011, 2012, and Run 2 $B^0 \to D^-\pi^+$ Monte Carlo.

The fits to $B_s^0 \to D_s^-\pi^+$ MC are done for both Run 1 and Run 2 and can be found in Fig. 19. All parameters were left floating, except n_1, β, and ζ. The resulting fitted parameters can be found in Tables 26 and 27 of Appendix A.3.

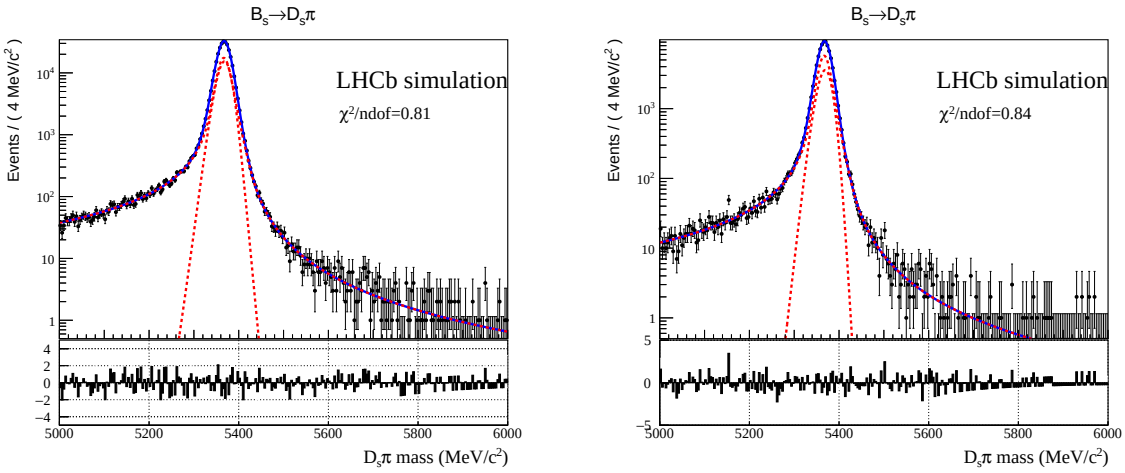

(a) Run 1 (b) Run 2

Figure 19: IpJo fits to Run 1 and Run 2 $B_s^0 \to D_s^- \pi^+$ Monte Carlo.

The final MC fits to both $B_s^0 \to D_s^- \pi^+$ and $B^0 \to D^- \pi^+$ in Fig. 18 and 19 show good agreement between the fitted PDF and MC.

5.3 Fits to data

Using the MC fits described in Section 5.2, a signal shape is defined for $B^0 \to D^- \pi^+$, which is used in $D^- \pi$ data fits. Like the MC fits, the data fit of Run 1 is split between 2011 and 2012. However, the 2011 and 2012 fits are done simultaneously, sharing some parameters. The signal shape parameter a_1 is shared between the fits to make it easier to compare it with both the Run 2 and the MC fits, and to improve the stability of the fit. The backgrounds share their parameters between the fits, while having a separate yield. The misidentified backgrounds however, share their yield relative to the yield of $B^0 \to D^- \pi^+$.

To be able to adjust for the differences between data and MC, several signal shape parameters are left free in the fit. These parameters are the mean, a_1, σ_I, σ_J, ν and τ. In the data, the misidentified backgrounds $B^0 \to D^- K^+$, $\Lambda_b^0 \to \Lambda_c^+ \pi^-$ and $B_s^0 \to D_s^- \pi^+$, and the partially reconstructed backgrounds $B^0 \to D^- \rho^+$ and $B^0 \to D^{*-} \pi^+$ are modelled using templates from MC, as explained in Section 4.2. The combinatorial background is modelled with an exponential plus a constant,

$$f(m, p_1, f_1) \propto f_1 e^{p_1 m} + (1 - f_1), \tag{20}$$

in which m is the invariant mass, f_1 is the fraction between the exponents, and p_1 is the parameter belonging to the exponent. An exponential plus constant is chosen after comparing it with fits that use a double exponential function to describe the combinatorial background. Since the fits that used a double exponential function fitted one of the exponential parameters to be almost zero, an exponential plus constant is chosen. The resulting fits can be found in Fig. 20 and the corresponding fit parameters are shown in Appendix A.2.

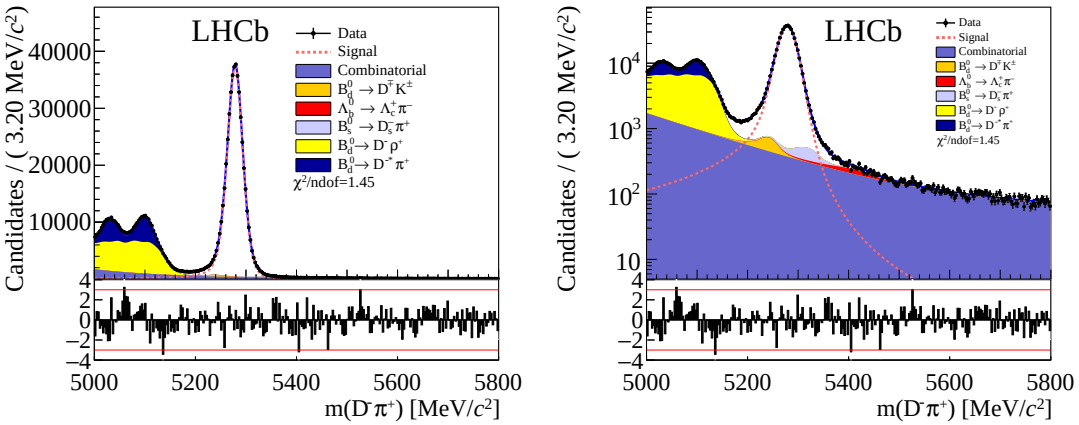

(a) Run 1

(b) Run 1 (logarithmic vertical axis)

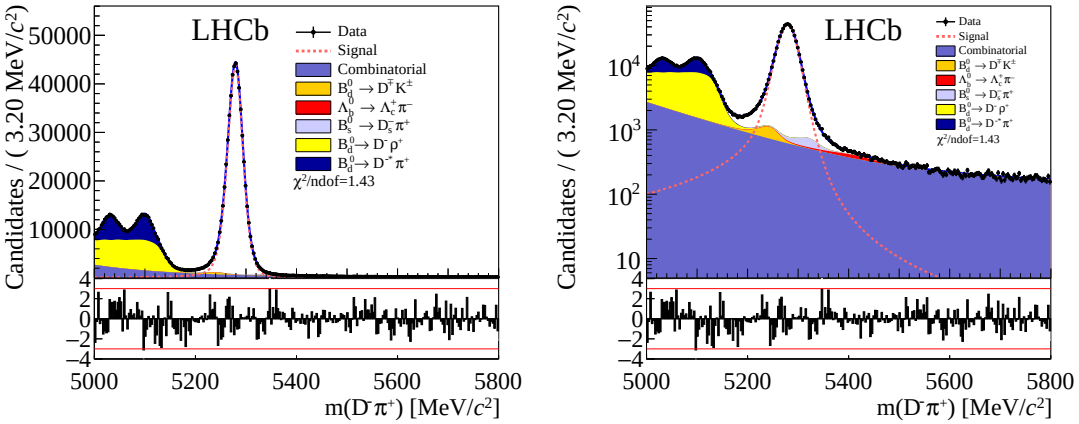

(c) Run 2

(d) Run 2 (logarithmic vertical axis)

Figure 20: Fits to the $B^0 \to D^-\pi^+$ signal in the Run 1 and Run 2 $D^-\pi^+$ data.

After obtaining the results from the $B^0 \to D^-\pi^+$ and $B^0_s \to D^-_s\pi^+$ fits in MC and the $B^0 \to D^-\pi^+$ fit in data, it is possible to compare the left tail of the PDFs, by comparing the values of a_1 from the fit. Tables 9 and 10 show a comparison of the results of the MC and data fits in $B^0 \to D^-\pi^+$ and $B^0_s \to D^-_s\pi^+$. Highlighted in bold is the value of a_1, which is chosen as a constraint for $B^0_s \to D^-_s\pi^+$ data, based on the results from the other fits. The resulting values of a_1 in the fits of Run 1 and Run 2 show very good agreement, while the a_1 values in MC and data differ. Based on the fit results summarised in Tables 9 and 10, an a_1 value of 1.3 ± 0.1 is chosen for the $B^0_s \to D^-_s\pi^+$ shape in both Run 1 and Run 2 data. The uncertainty of ± 0.1 is chosen to cover the differences observed in the MC between Run 1 and Run 2. To constrain this value, a GC is added to the likelihood function of $D^-_s\pi^+$ fit.

	$B^0 \to D^-\pi^+$		$B_s^0 \to D_s^-\pi^+$
	2011	2012	Run 1
MC	1.52 ± 0.10	1.55 ± 0.08	1.58 ± 0.24
Data	1.308 ± 0.017		$\mathbf{1.3 \pm 0.1}$

Table 9: Comparison of the parameter a_1 in Run 1 results. A value of 1.3 is chosen for the $B_s^0 \to D_s^-\pi^+$ data with an error of 0.1. This value is highlighted in bold.

	$B^0 \to D^-\pi^+$	$B_s^0 \to D_s^-\pi^+$
MC	1.58 ± 0.12	1.55 ± 0.20
Data	1.282 ± 0.026	$\mathbf{1.3 \pm 0.1}$

Table 10: Comparison of the parameter a_1 in Run 2 results. A value of 1.3 is chosen for the $B_s^0 \to D_s^-\pi^+$ data with an error of 0.1. This value is highlighted in bold.

6 Signal yield from mass fit

Finally, after determining the signal shape of $B_s^0 \to D_s^- \pi^+$ it is possible to make a $D_s^- \pi^+$ mass fit. As seen in the previous Section, a_1 is Gaussian constrained to 1.3 ± 0.1. The partially reconstructed and misidentified backgrounds are described by templates, as described in Section 4.2. The combinatorial background is split in true and random D_s^- combinatorial background, as defined in Section 4.4. Using the estimated relative misidentified background yield from Section 4.3, a GC is used to constrain the misidentified backgrounds, except the $B^0 \to D^- \pi^+$ decay, which is fixed in the fit. The other yields, *i.e.* from the signals, partially reconstructed and combinatorial backgrounds, are free in the fit. To fit the $B_s^0 \to D_s^- \pi^+$ signal shape, an IpJo is used, while leaving the widths σ_I and σ_J, the mean, and the parameter ν free in the fit. Fig. 21 shows the results of the fits.

The fits from Fig. 21 result in a $B^0 \to D_s^+ \pi^-$ yield of 1035 ± 118 and 1648 ± 157 for Run 1 and Run 2, respectively. All the fitted parameters for the corresponding fits can be found in Appendix A.4.

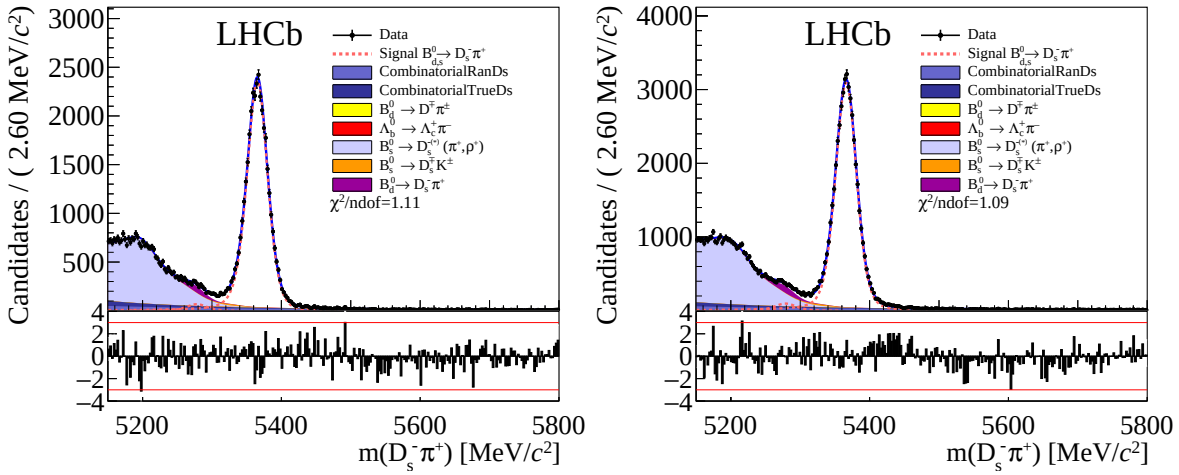

(a) Run 1

(b) Run 2

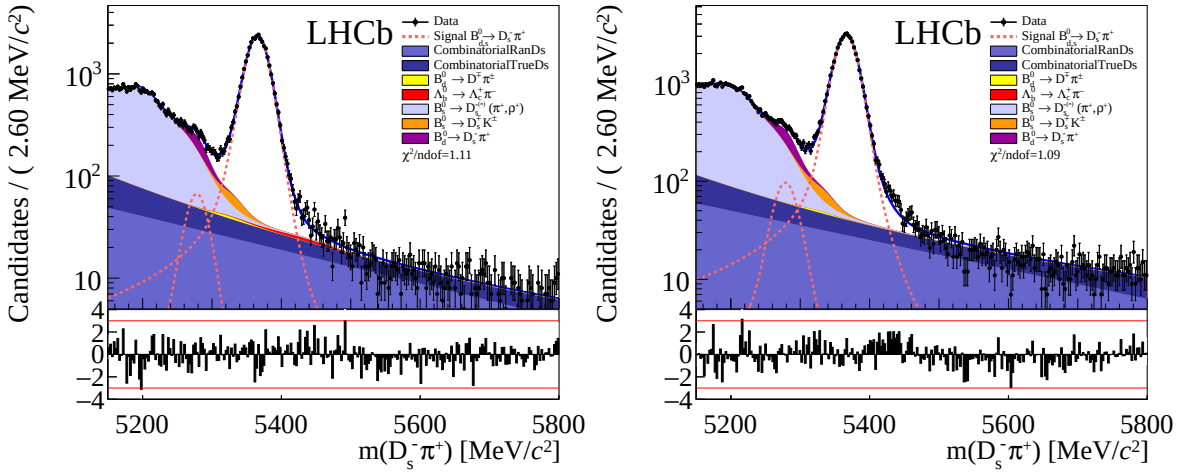

(c) Run 1 (logarithmic vertical axis)

(d) Run 2 (logarithmic vertical axis)

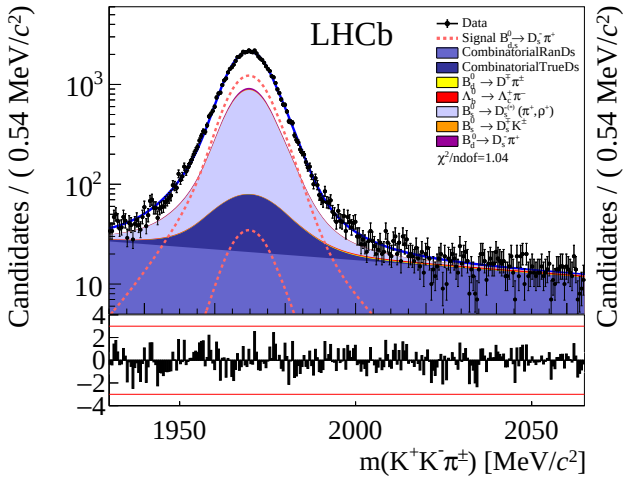

(e) Run 1 (logarithmic vertical axis)

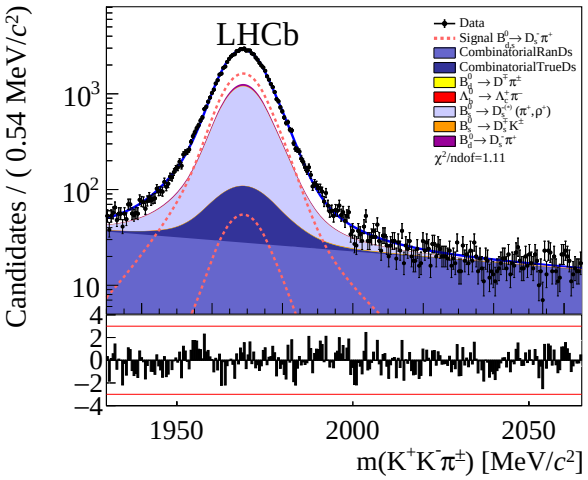

(f) Run 2 (logarithmic vertical axis)

Figure 21: Two-dimensional fits to Run 1 and Run 2 $D_s^- \pi^+$ data. The fits are simultaneously done to both the $D_s^- \pi^+$ mass and the $K^- K^+ \pi^-$ mass.

7 Systematic uncertainties and consistency checks

7.1 Systematic uncertainties

In physics, systematic uncertainties describe uncertainties not being of a statistical nature. These uncertainties can originate from an imperfect calibrated measurement apparatus, assumptions in the experiment, and the model used in the analysis.

The magnitude of the systematic uncertainties is not determined in this thesis. However, possible sources of systematic uncertainties are listed below.

L0 trigger efficiency In the process of taking data, a selection is made by the L0 trigger, as explained in Section 3.1. In this selection, a difference in detection efficiency arises between pions and kaons, which is not implemented in simulation. Since the ratio of $B^0 \to D_s^+\pi^-$ and $B^0 \to D^-\pi^+$ is measured, the difference manifests itself when triggering on the D^- and D_s^- mesons.

Offline selection efficiency The efficiencies of the $B^0 \to D_s^+\pi^-$ and $B^0 \to D^-\pi^+$ signals are calculated from MC samples. A difference in the distributions of some variables between MC and data can affect these efficiencies. Therefore, this way of estimating the offline selection efficiency brings a systematic uncertainty to the analysis.

PID efficiency To determine the $B^0 \to D_s^+\pi^-$ and $B^0 \to D^-\pi^+$ signal efficiency it is crucial to take the PID efficiency into account. This is done using PID reweighting histograms, as described in Section 3.3. Estimating the PID efficiencies by using simulations and reweighting histograms brings a systematic uncertainty.

Combinatorial background This analysis has a lot of attention for the combinatorial background. To constrain it, a two-dimensional fit is made in the $D_s^-\pi^+$ fit. This results in a well-constrained random D_s^- combinatorial background. However, the true D_s^- combinatorial background manifests itself around the peak of the D_s^- mass and its invariant mass is for a large part similar to the partially reconstructed backgrounds. As described in Section 4.4, the true D_s^- combinatorial background is described by an exponential plus a constant in the $D_s^-\pi^+$ invariant mass and by a DCB with a free width in the $K^-K^+\pi^-$ invariant mass. In the $D^-\pi^+$ invariant mass fit the combinatorial background is also described by an exponential plus a constant. These choices are found to be the most optimal, but they might bring a systematic uncertainty.

Constraining misidentified backgrounds All the misidentified backgrounds in this analysis are either fixed or Gaussian constrained. This is done based on simulations as well as external inputs like branching fractions, hadronisation fractions, and PID calibration histograms. To account for the uncertainty this brings the misidentified backgrounds are allowed to vary by a GC, except the fixed $B^0 \to D^-\pi^+$ background in the $D_s^-\pi^+$ fit, due to its small number of estimated events. Nevertheless, systematic uncertainties can still be present, when the estimation of the number of events is too far off.

Backgrounds templates As explained in Section 4.2, the partially reconstructed and misidentified backgrounds are described by RooKeys PDFs. These PDFs are

constructed from simulated data. The smoothness of these PDFs is described by the parameter ρ. If the value of ρ is fixed to a certain value, it is possible that the PDF is too detailed and follows statistical fluctuations, or it can be not detailed enough to describe the background well. Therefore, fixing ρ to a certain value brings a systematic uncertainty.

7.2 Consistency check: magnet polarity

To check the consistency and stability of the invariant mass fits, fits are done to magnet down (*MagDown*) and magnet up (*MagUp*) data separately. The yields determined by these fits should be compatible with the combined fit, if the fit is stable.

Fig. 22 shows this consistency check of the $D^-\pi^+$ invariant mass fit, while the fitted parameters can be found in Appendix A.5. The yields of the $B^0 \to D^-\pi^+$ signal are compatible with the combined fit. On top of this, the other parameters of this fit are also in agreement with the other magnet polarity.

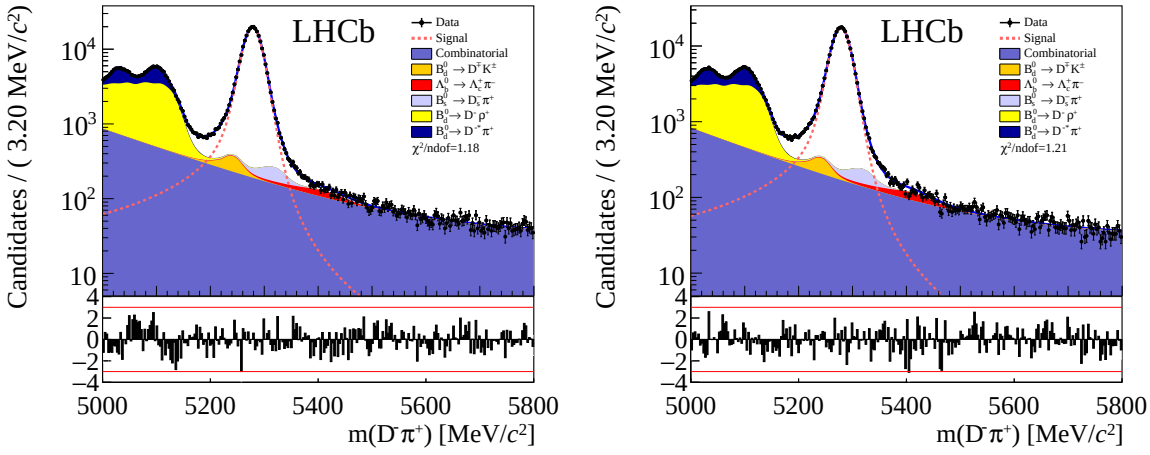

(a) Run 1 *MagDown*

(b) Run 1 *MagUp*

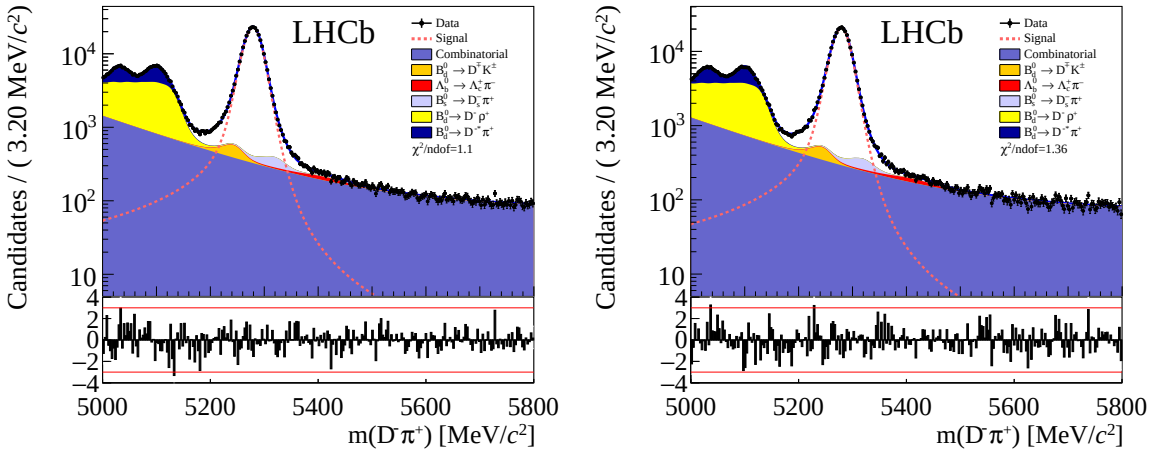

(c) Run 2 *MagDown*

(d) Run 2 *MagUp*

Figure 22: Consistency check comparing the $D^-\pi^+$ fit between both magnet polarities in Run 1 and Run 2.

Figs. 23 and 24 show the magnet polarity consistency check for the two-dimensional $D_s^-\pi^+$ mass fit. The corresponding parameters can be found in Appendix A.6. The yields of the $B^0 \to D_s^+\pi^-$ and $B_s^0 \to D_s^-\pi^+$ signals are compatible with the combined fit. The true D_s^- combinatorial and the partially reconstructed backgrounds, however, turn out not to be compatible between the magnet polarities. Fig. 24 shows clearly how the partially reconstructed and true D_s^- combinatorial background are very correlated, without affecting the signal yields.

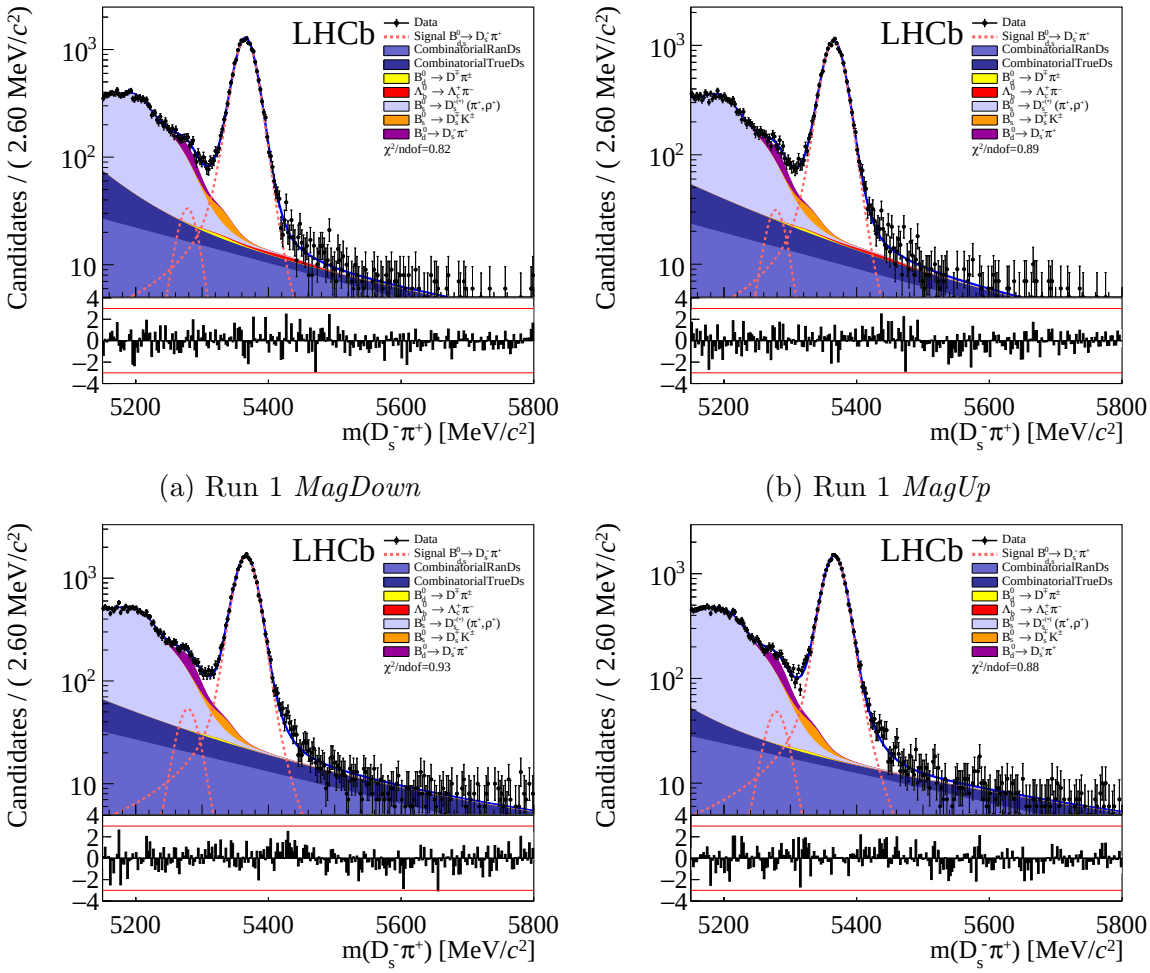

(a) Run 1 *MagDown*

(b) Run 1 *MagUp*

(c) Run 2 *MagDown*

(d) Run 2 *MagUp*

Figure 23: Consistency check comparing the $D_s^-\pi^+$ invariant mass fits between both magnet polarities in Run 1 and Run 2.

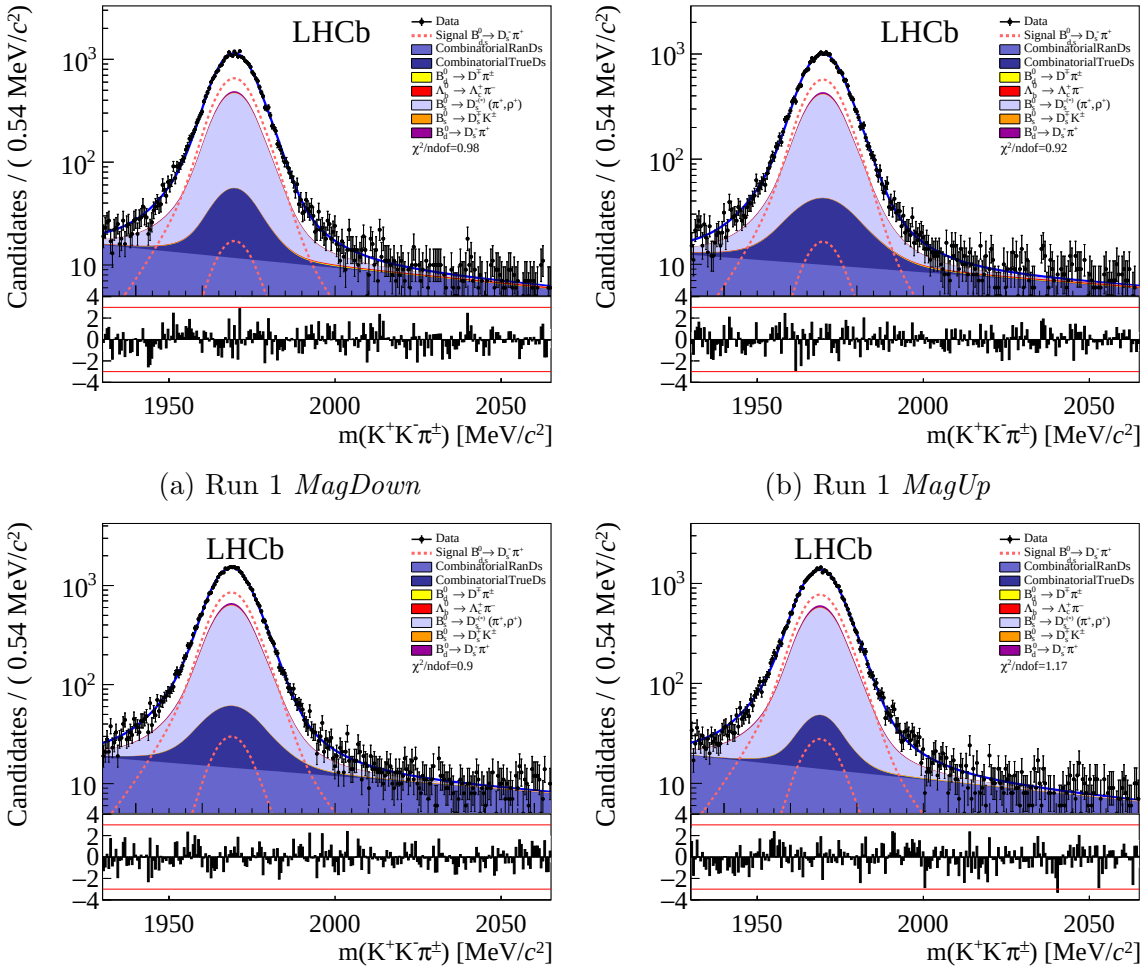

(a) Run 1 *MagDown* (b) Run 1 *MagUp*

(c) Run 2 *MagDown* (d) Run 2 *MagUp*

Figure 24: Consistency check comparing the $K^-K^+\pi^-$ invariant mass fits between both magnet polarities in Run 1 and Run 2.

8 Branching fraction and interpretation

As formulated in Section 1.2 the branching fraction of $B^0 \to D_s^+\pi^-$ can be calculated using

$$\mathcal{B}(B^0 \to D_s^+\pi^-) = \mathcal{B}(B^0 \to D^-\pi^+)\frac{\epsilon_{B^0\to D^-\pi^+}}{\epsilon_{B^0\to D_s^+\pi^-}}\frac{N_{B^0\to D_s^+\pi^-}}{N_{B^0\to D^-\pi^+}}\frac{\mathcal{B}(D^- \to K^+\pi^-\pi^-)}{\mathcal{B}(D_s^- \to K^-K^+\pi^-)}, \tag{21}$$

where the efficiencies $\epsilon_{B^0\to D^-\pi^+}$ and $\epsilon_{B^0\to D_s^+\pi^-}$ are calculated using MC, and the yields $N_{B^0\to D_s^+\pi^-}$ and $N_{B^0\to D^-\pi^+}$ are obtained from mass fits. These quantities are obtained for Run 1 and Run 2 separately, resulting in two branching fractions, which are combined. Table 11 shows the $B^0 \to D_s^+\pi^-$ and $B^0 \to D^-\pi^+$ signal efficiencies, from Section 3.5, and yields, from Sections 5.3 and 6.

	Run 1	Run 2
$\epsilon_{B^0\to D_s^+\pi^-}$ (%)	0.1534 ± 0.0010	0.2014 ± 0.0012
$\epsilon_{B^0\to D^-\pi^+}$ (%)	0.3569 ± 0.0020	0.4368 ± 0.0010
$N_{B^0\to D_s^+\pi^-}$	1035 ± 118	1648 ± 157
$N_{B^0\to D^-\pi^+}$	501356 ± 1094	584975 ± 1540

Table 11: Results of $B^0 \to D_s^+\pi^-$ and $B^0 \to D^-\pi^+$ signal efficiencies and yields.

Filling in the values from Table 11 into Eq. (21) results in the branching fractions

$$\mathcal{B}(B^0 \to D_s^+\pi^-) = (19.9 \pm 2.3\,(\text{stat}) \pm 1.4\,(\mathcal{B})) \cdot 10^{-6} \quad \text{(Run 1)}, \tag{22}$$
$$\mathcal{B}(B^0 \to D_s^+\pi^-) = (25.4 \pm 2.4\,(\text{stat}) \pm 1.7\,(\mathcal{B})) \cdot 10^{-6} \quad \text{(Run 2)}, \tag{23}$$
$$\mathcal{B}(B^0 \to D_s^+\pi^-) = (23.1 \pm 1.7\,(\text{stat}) \pm 1.6\,(\mathcal{B})) \cdot 10^{-6} \quad \text{(Combined)}, \tag{24}$$

where (stat) stands for the statistical uncertainty and $(\mathcal{B})$ for the error from using branching fractions from the PDG. A small tension between the Run 1 and Run 2 branching fractions is visible, but this is not significant (1.7σ). Therefore, the Run 1 and Run 2 results are compatible with each other, and are combined in Eq. (24). Previous measurements of BaBar [5], Belle [6] and their average [2] agree very well with the branching fraction found in this analysis,

$$\mathcal{B}(B^0 \to D_s^+\pi^-) = (25 \pm 4 \pm 2) \cdot 10^{-6} \quad \text{(BaBar)}, \tag{25}$$
$$\mathcal{B}(B^0 \to D_s^+\pi^-) = (19.9 \pm 2.6 \pm 1.8) \cdot 10^{-6} \quad \text{(Belle)}, \tag{26}$$
$$\mathcal{B}(B^0 \to D_s^+\pi^-) = (21.6 \pm 2.6) \cdot 10^{-6} \quad \text{(Combined)}. \tag{27}$$

The branching fraction calculated in this analysis the most precise measurement so far, not taking into account systematic uncertainties. Combining the $B^0 \to D_s^+\pi^-$ branching fraction from this analysis with previous measurements of Belle and BaBar gives a new world average of

$$\mathcal{B}(B^0 \to D_s^+\pi^-) = (22.4 \pm 1.7) \cdot 10^{-6}. \tag{28}$$

8.1 Implications for $|V_{ub}|$ and $|a_{\mathrm{NF}}|$

As seen in Eq. (5) from Section 1.1.1, the branching fraction of $B^0 \to D_s^+\pi^-$ is dependent on both $|a_{\mathrm{NF}}|$ and $|V_{ub}|$. Using our result for $\mathcal{B}(B^0 \to D_s^+\pi^-)$, is it possible to probe the product $|a_{\mathrm{NF}}||V_{ub}|$. Other external inputs needed for probing $|a_{\mathrm{NF}}||V_{ub}|$ are the form factor $F(B^0 \to \pi^-)$, the decay constant f_{D_s}, and the CKM-element $|V_{cs}|$. The form factor is obtained using Refs. [45, 46],

$$F(B^0 \to \pi^-)|_{q^2=m^2_{D_s^-}} = 0.333 \pm 0.026, \tag{29}$$

the decay constant is taken from Ref. [47]

$$f_{D_s} = 0.2498 \pm 0.0003\,\mathrm{GeV}, \tag{30}$$

and finally $|V_{cs}|$ is taken from the PDG [2]

$$|V_{cs}| = 0.997 \pm 0.017. \tag{31}$$

Using these external CKM and QCD parameters, the the product of $|V_{ub}|$ and the non-factorisation constant $|a_{\mathrm{NF}}|$ are calculated. Using the current world average [2], the combined Run 1 and Run 2 result and the new world average of $\mathcal{B}(B^0 \to D_s^+\pi^-)$, respectively, it is found that

$$|V_{ub}||a_{\mathrm{NF}}| = (3.33 \pm 0.20\,(\mathcal{B}) \pm 0.26\,(\mathrm{ext})) \cdot 10^{-3} \quad \text{(current wold average)}, \tag{32}$$
$$|V_{ub}||a_{\mathrm{NF}}| = (3.34 \pm 0.17\,(\mathcal{B}) \pm 0.27\,(\mathrm{ext})) \cdot 10^{-3} \quad \text{(this analysis)}, \tag{33}$$
$$|V_{ub}||a_{\mathrm{NF}}| = (3.33 \pm 0.13\,(\mathcal{B}) \pm 0.26\,(\mathrm{ext})) \cdot 10^{-3} \quad \text{(new world average)}, \tag{34}$$

where $(\mathcal{B})$ is the uncertainty on the $B^0 \to D_s^+\pi^-$ branching fraction and (ext) is the uncertainty on the external CKM and QCD parameters, dominated by the uncertainty on the form factor. The determination of $|V_{ub}||a_{\mathrm{NF}}|$ using this analysis is more precise than and consistent with the current world average. In Fig. 25, $|a_{\mathrm{NF}}||V_{ub}|$ is visualised.

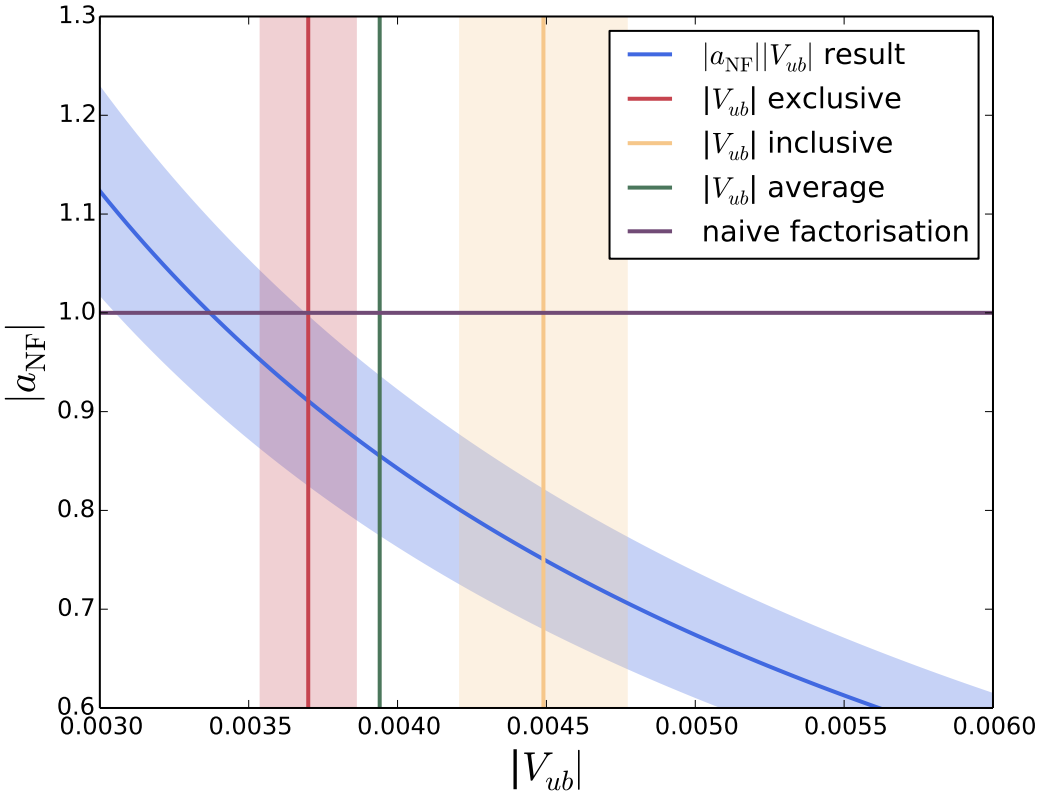

Figure 25: Result of the determination of $|a_{\rm NF}||V_{ub}|$. The blue line represents the result in Eq. (33), while the three vertical lines are the exclusive and inclusive measurements of $|V_{ub}|$, and average value of $|V_{ub}|$. The horizontal line at $|a_{\rm NF}| = 1.0$ represents naive factorisation. The error bands represent a confidence level of 68%. For the average value of $|V_{ub}|$ and naive factorisation, the error bands are not shown.

Determining the value of either $|a_{\rm NF}|$ or $|V_{ub}|$ from Eq. (33) is not possible without the external input of $|V_{ub}|$ or $|a_{\rm NF}|$. Therefore, an expression for the non-factorisable effects $|a_{\rm NF}|$ is obtained using the average value of $|V_{ub}|$, as given in Section 1.1,

$$|a_{\rm NF}| = 0.86 \pm 0.04\,(\mathcal{B}) \pm 0.07\,(\text{ext}) \pm 0.08\,(V_{ub}), \tag{35}$$

where (V_{ub}) is the uncertainty on $|V_{ub}|$. The main uncertainty on $|a_{\rm NF}|$ is caused by the form factor and $|V_{ub}|$, while the uncertainty from $\mathcal{B}(B^0 \to D_s^+\pi^-)$ is about 5%. This value of $|a_{\rm NF}|$ is in agreement with naive factorisation. To be able to claim a deviation from unity, smaller uncertainties on the form factor and $|V_{ub}|$ are needed.

It is not possible to probe $|V_{ub}|$ using the computed $|a_{\rm NF}|$ result, since it required external input for $|V_{ub}|$. However, because our value of $|a_{\rm NF}|$ is compatible with naive factorisation, $|V_{ub}|$ can be estimated by assuming naive factorisation, $|a_{\rm NF}| = 1.0 \pm 0.2$, where the uncertainty is estimated from the difference between the computed value of $|a_{\rm NF}|$ and naive factorisation. The resulting value of $|V_{ub}|$ is

$$|V_{ub}| = (3.37 \pm 0.17\,(\mathcal{B}) \pm 0.27\,(\text{ext}) \pm 0.67\,(a_{\rm NF})) \cdot 10^{-3}, \tag{36}$$

where $(\mathcal{B})$ is the uncertainty on $\mathcal{B}(B^0 \to D_s^+\pi^-)$, (ext) is the uncertainty on external CKM and QCD inputs and $(a_{\rm NF})$ is the uncertainty on naive factorisation. This value is closer to exclusive than inclusive $|V_{ub}|$ measurements, but is compatible with both, due to large uncertainties.

8.2 Determination of $r_{D\pi}$

As mentioned in Section 1.1, the branching fraction of $B^0 \to D_s^+\pi^-$ can be used to determine the parameter $r_{D\pi}$,

$$r_{D\pi} = \tan\theta_c \frac{f_{D^+}}{f_{D_s}} \sqrt{\frac{\mathcal{B}(B^0 \to D_s^+\pi^-)}{\mathcal{B}(B^0 \to D^-\pi^+)}}. \tag{37}$$

The tangent of the Cabibbo angle θ_c is obtained from the PDG [2],

$$\tan\theta_c = \frac{|V_{us}|}{|V_{ud}|} = 0.2302 \pm 0.0005, \tag{38}$$

while the fraction of the decay constants f_{D_s} and f_{D^+} is taken from Ref. [47],

$$\frac{f_{D_s}}{f_{D^+}} = 1.1749 \pm 0.0011. \tag{39}$$

Inserting the measured branching fraction of $B^0 \to D_s^+\pi^-$, the tangent of θ_c, and the fractions between the decay constants f_{D_s} and f_{D^+} into Eq. (37) gives

$$r_{D\pi} = 0.0188 \pm 0.0008 \pm 0.0038, \tag{40}$$

where the first uncertainty comes from the inputs of Eq. (37), and the second uncertainty comes from possible non-factorisable SU(3)-breaking effects, estimated to be 20% as suggested by Ref. [4]. This is more precise than and consistent with Ref. [44],

$$r_{D\pi} = 0.0182 \pm 0.0012 \pm 0.0036. \tag{41}$$

8.3 Production rate ratio dependence on collision energy

Since the $B_s^0 \to D_s^-\pi^+$ and $B^0 \to D^-\pi^+$ signals are studied in this analysis for both Run 1 and Run 2, see Section 5, they can be used to study the dependence of the ratio of the fragmentation fractions f_s/f_d on the centre-of-mass energy at the LHC. The ratio f_s/f_d is the production rate of B_s^0 mesons compared to B^0 mesons. Using the efficiency-corrected yields of the $B_s^0 \to D_s^-\pi^+$ and $B^0 \to D^-\pi^+$ signals, the fraction of f_s/f_d in Run 1 and Run 2 is made,

$$\frac{f_s/f_d|_{\sqrt{s}=13\,\text{TeV}}}{f_s/f_d|_{\sqrt{s}=7/8\,\text{TeV}}} = \frac{(N_{B_s^0\to D_s^-\pi^+}\epsilon_{B^0\to D^-\pi^+})/(N_{B^0\to D^-\pi^+}\epsilon_{B_s^0\to D_s^-\pi^+})|_{\sqrt{s}=13\,\text{TeV}}}{(N_{B_s^0\to D_s^-\pi^+}\epsilon_{B^0\to D^-\pi^+})/(N_{B^0\to D^-\pi^+}\epsilon_{B_s^0\to D_s^-\pi^+})|_{\sqrt{s}=7/8\,\text{TeV}}}. \tag{42}$$

Table 12 shows the yields and efficiencies of the $B_s^0 \to D_s^-\pi^+$ and $B^0 \to D^-\pi^+$ signals obtained in this analysis. Note that the PID efficiency of $B_s^0 \to D_s^-\pi^+$ is assumed to be the same as $B^0 \to D_s^+\pi^-$.

	Run 1	Run 2
$\epsilon_{B_s^0\to D_s^-\pi^+}$ (%)	0.1598 ± 0.0006	0.2069 ± 0.0008
$\epsilon_{B^0\to D^-\pi^+}$ (%)	0.3569 ± 0.0020	0.4368 ± 0.0010
$N_{B_s^0\to D_s^-\pi^+}$	36606 ± 238	49021 ± 313
$N_{B^0\to D^-\pi^+}$	500842 ± 1167	584929 ± 1619

Table 12: Results of $B_s^0 \to D_s^-\pi^+$ and $B^0 \to D^-\pi^+$ signal efficiencies and yields.

Inserting the values of Table 12 into Eq. (42) gives

$$\frac{f_s/f_d|_{\sqrt{s}=13\,\text{TeV}}}{f_s/f_d|_{\sqrt{s}=7/8\,\text{TeV}}} = 1.085 \pm 0.014. \tag{43}$$

The value of f_s/f_d is significantly higher in Run 2 than in Run 1. This means that a higher centre-of-mass energy results in a higher number of B_s^0 mesons produced compared to B^0 mesons.

This is also observed in Ref. [7], where the ratio of the efficiency corrected $B_s^0 \to J/\psi\,\phi$ and $B^+ \to J/\psi\,K^+$ decays is used, resulting in

$$\frac{f_s/f_d|_{\sqrt{s}=13\,\text{TeV}}}{f_s/f_d|_{\sqrt{s}=7\,\text{TeV}}} = 1.068 \pm 0.046. \tag{44}$$

This is in agreement with Eq. (43), but has a large uncertainty, making the fragmentation fraction of Run 2 compatible with Run 1. The result of this analysis, however, *is* significantly deviating from 1.0, making it possible to state that the fragmentation fraction is dependent on the collision energy.

9 Conclusion

In this analysis a branching fraction measurement of $B^0 \to D_s^+\pi^-$ is performed. The $B^0 \to D_s^+\pi^-$ decay is described by a single tree diagram and probes the $b \to u$ quark transition $|V_{ub}|$ and non-factorisable effects $|a_{\rm NF}|$. Measuring the $B^0 \to D_s^+\pi^-$ signal yield is challenging, due to a large number of background events and the tail of the $B_s^0 \to D_s^-\pi^+$ signal around the $B^0 \to D_s^+\pi^-$ signal peak. Therefore, the $B_s^0 \to D_s^-\pi^+$ signal shape and the backgrounds are studied in detail. After studying different signal shapes, an Ipatia plus a Johnson SU function is chosen to describe the $B_s^0 \to D_s^-\pi^+$ and $B^0 \to D^-\pi^+$ signal. The left tail parameters of this signal shape are investigated and constrained for the $B_s^0 \to D_s^-\pi^+$ shape. The combinatorial background is split between randomly combined pions and true D_s^- mesons, and pions combined with a D_s^- meson resulting from randomly combined $K^+K^-\pi^+$ candidates. The random D_s^- combinatorial background is found to be described by an exponential distribution and constrained by doing a two-dimensional fit in both the B_s^0 and D_s^- invariant mass. This analysis is done for both 2011 and 2012 (Run 1), and 2015 and 2016 (Run 2) data.

Finally, the $B^0 \to D_s^+\pi^-$ branching fraction is presented for Run 1 and Run 2 separately. Combining this branching fraction between all the years yields

$$\mathcal{B}(B^0 \to D_s^+\pi^-) = (23.1 \pm 2.3) \cdot 10^{-6}, \tag{45}$$

which is the most precise measurement of $\mathcal{B}(B^0 \to D_s^+\pi^-)$, not taking into account systematic uncertainties, and in agreement with the world average. Using this branching fraction the product of $|V_{ub}|$ and the non-factorisation constant $|a_{\rm NF}|$ is determined,

$$|V_{ub}||a_{\rm NF}| = (3.34 \pm 0.32) \cdot 10^{-3}. \tag{46}$$

Using the average value of $|V_{ub}|$, as given in the PDG, the non-factorisable effects are determined,

$$|a_{\rm NF}| = 0.86 \pm 0.11, \tag{47}$$

which is compatible with naive factorisation. Assuming naive factorisation, $|V_{ub}|$ is also determined, but due to large uncertainties mostly on factorisation it is not possible to deliver a competitive measurement of $|V_{ub}|$.

Using the measurement of $\mathcal{B}(B^0 \to D_s^+\pi^-)$, the parameter $r_{D\pi}$, which is required for studying CP asymmetries in $B^0 \to D^\mp\pi^\pm$ decays, is determined to be

$$r_{D\pi} = 0.0188 \pm 0.0008 \pm 0.0038. \tag{48}$$

Finally, the dependence of f_s/f_d on centre-of-mass energy is studied. It is found that f_s/f_d is significantly higher in Run 2 than in Run 1,

$$\frac{f_s/f_d|_{\sqrt{s}=13\,\text{TeV}}}{f_s/f_d|_{\sqrt{s}=7/8\,\text{TeV}}} = 1.085 \pm 0.014. \tag{49}$$

Thus, more B_s^0 mesons relative to B^0 mesons are produced at a higher centre-of-mass energy.

9.1 Outlook

Although it seems this analysis is fully finished, some things can be added or improved in the future. First of all, assigning systematic uncertainties is necessary. A list of possible systematic uncertainties can be found in Section 7.

On top of this, new MC samples are requested to be produced, since the current ones contain some bugs. One of them is the so-called TISTOS bug [48], which is expected not to have a large impact on this analysis. After this bug was discovered, the production of nTuples stopped and this resulted in the lack of $B_s^0 \to D_s^- K^+$, $\Lambda_b^0 \to \Lambda_c^+ \pi^-$ and $B_s^0 \to D_s^{*-} \pi^+$ 2016 MC nTuples. In this analysis, this is solved by using 2015 MC for the missing 2016 MC. However, since the $B_s^0 \to D_s^{*-} \pi^+$ decay is a partially reconstructed background that is present directly under the $B^0 \to D_s^+ \pi^-$ signal, it is important to describe it as good as possible. An MC sample of 2016 can help with this.

Additionally, quantifying the ratio between the yields of partially reconstructed backgrounds is useful in order to constrain these partially reconstructed backgrounds. This can be done in a similar way as in Section 4.3.

Future analyses are expected to further reduce the uncertainty on $\mathcal{B}(B^0 \to D_s^+ \pi^-)$. In particular a measurement by the new B-Factory Belle II would be promising.

Appendices

A Fit parameters

A.1 Fit parameters of $B^0 \to D^-\pi^+$ Monte Carlo

Parameter number	Parameter name	Fitted value	Initial value
0	$DCB\_BeautyMass\_alpha1\_combData\_Signal\_both\_kpipi\_run1$	1.567 ± 0.016	1.6 ± 0
1	$DCB\_BeautyMass\_alpha2\_combData\_Signal\_both\_kpipi\_run1$	-2.034 ± 0.020	-2.0 ± 0
2	$DCB\_BeautyMass\_frac\_combData\_Signal\_both\_kpipi\_run1$	0.4527 ± 0.0086	0.5 ± 0
3	$DCB\_BeautyMass\_n1\_combData\_Signal\_both\_kpipi\_run1$	1.623 ± 0.017	1.6 ± 0
4	$DCB\_BeautyMass\_n2\_combData\_Signal\_both\_kpipi\_run1$	2.394 ± 0.039	2.4 ± 0
5	$DCB\_BeautyMass\_sigma1\_combData\_Signal\_both\_kpipi\_run1$	18.96 ± 0.12	19.0 ± 0
6	$DCB\_BeautyMass\_sigma2\_combData\_Signal\_both\_kpipi\_run1$	12.880 ± 0.067	13.0 ± 0
7	$Signal\_BeautyMass\_mean\_combData\_Signal\_both\_kpipi\_run1$	5279.720 ± 0.013	$(5.28 \pm 0)e+03$

Table 13: Double Crystal Ball fit parameters of fit to $B^0 \to D^-\pi^+$ signal MC between 5000 and 6000 GeV/c^2.

Parameter number	Parameter name	Fitted value	Initial value
0	$Ipatia\_BeautyMass\_a1\_combData\_Signal\_both\_kpipi\_run1$	2.0156 ± 0.0068	1.8 ± 0
1	$Ipatia\_BeautyMass\_a2\_combData\_Signal\_both\_kpipi\_run1$	2.924 ± 0.026	2.5 ± 0
2	$Ipatia\_BeautyMass\_l\_combData\_Signal\_both\_kpipi\_run1$	-3.490 ± 0.038	-2.0 ± 0
3	$Ipatia\_BeautyMass\_mean\_combData\_Signal\_both\_kpipi\_run1$	5279.766 ± 0.012	$(5.28 \pm 0)e+03$
4	$Ipatia\_BeautyMass\_n1\_combData\_Signal\_both\_kpipi\_run1$	1.3744 ± 0.0093	1.5 ± 0
5	$Ipatia\_BeautyMass\_n2\_combData\_Signal\_both\_kpipi\_run1$	2.329 ± 0.030	2.2 ± 0
6	$Ipatia\_BeautyMass\_sigma\_combData\_Signal\_both\_kpipi\_run1$	17.110 ± 0.028	17.0 ± 0

Table 14: Ipatia fit parameters of fit to $B^0 \to D^-\pi^+$ signal MC between 5000 and 6000 GeV/c^2.

Parameter number	Parameter name	Fitted value	Initial value
0	$IpatiaPlusGaussian\_BeautyMass\_a1\_combData\_Signal\_both\_kpipi\_run1$	1.777 ± 0.016	1.8 ± 0
1	$IpatiaPlusGaussian\_BeautyMass\_a2\_combData\_Signal\_both\_kpipi\_run1$	2.109 ± 0.026	2.5 ± 0
2	$IpatiaPlusGaussian\_BeautyMass\_fracI\_combData\_Signal\_both\_kpipi\_run1$	0.692 ± 0.010	0.7 ± 0
3	$IpatiaPlusGaussian\_BeautyMass\_l\_combData\_Signal\_both\_kpipi\_run1$	-6.44 ± 0.38	-5.0 ± 0
4	$IpatiaPlusGaussian\_BeautyMass\_mean\_combData\_Signal\_both\_kpipi\_run1$	5279.899 ± 0.013	$(5.28 \pm 0)e+03$
5	$IpatiaPlusGaussian\_BeautyMass\_n1\_combData\_Signal\_both\_kpipi\_run1$	1.370 ± 0.012	1.5 ± 0
6	$IpatiaPlusGaussian\_BeautyMass\_n2\_combData\_Signal\_both\_kpipi\_run1$	2.614 ± 0.032	2.5 ± 0
7	$IpatiaPlusGaussian\_BeautyMass\_sigmaG\_combData\_Signal\_both\_kpipi\_run1$	18.76 ± 0.15	19.0 ± 0
8	$IpatiaPlusGaussian\_BeautyMass\_sigmaI\_combData\_Signal\_both\_kpipi\_run1$	14.255 ± 0.093	14.0 ± 0

Table 15: Ipatia Plus Gaussian fit parameters of fit to $B^0 \to D^-\pi^+$ signal MC between 5000 and 6000 GeV/c^2.

Parameter number	Parameter name	Fitted value	Initial value
0	*IpatiaPlusJohnsonSU_BeautyMass_a1_combData_Signal_both_kpipi_run1*	1.211 ± 0.085	1.211801 ± 0
1	*IpatiaPlusJohnsonSU_BeautyMass_a2_combData_Signal_both_kpipi_run1*	2.73 ± 0.16	2.728039 ± 0
2	*IpatiaPlusJohnsonSU_BeautyMass_fracI_combData_Signal_both_kpipi_run1*	0.377 ± 0.030	0.377421 ± 0
3	*IpatiaPlusJohnsonSU_BeautyMass_l_combData_Signal_both_kpipi_run1*	-1.704 ± 0.088	-1.705064 ± 0
4	*IpatiaPlusJohnsonSU_BeautyMass_mean_combData_Signal_both_kpipi_run1*	5279.573 ± 0.017	$(5.279572874 \pm 0)e+03$
5	*IpatiaPlusJohnsonSU_BeautyMass_n1_combData_Signal_both_kpipi_run1*	1.338 ± 0.021	1.337512 ± 0
6	*IpatiaPlusJohnsonSU_BeautyMass_n2_combData_Signal_both_kpipi_run1*	2.374 ± 0.066	2.374238 ± 0
7	*IpatiaPlusJohnsonSU_BeautyMass_nu_combData_Signal_both_kpipi_run1*	-0.325 ± 0.038	-0.325333 ± 0
8	*IpatiaPlusJohnsonSU_BeautyMass_sigmaI_combData_Signal_both_kpipi_run1*	22.98 ± 0.88	22.97069 ± 0
9	*IpatiaPlusJohnsonSU_BeautyMass_sigmaJ_combData_Signal_both_kpipi_run1*	15.824 ± 0.071	15.824744 ± 0
10	*IpatiaPlusJohnsonSU_BeautyMass_tau_combData_Signal_both_kpipi_run1*	0.397 ± 0.012	0.396891 ± 0

Table 16: Ipatia Plus Johnson SU fit parameters of fit to $B^0 \to D^- \pi^+$ signal MC between 5000 and 6000 GeV/c^2.

Parameter number	Parameter name	Fitted value	Initial value
0	*IpatiaPlusJohnsonSU_BeautyMass_a1_combData_Signal_both_kpipi_2011*	1.515 ± 0.072	1.5 ± 0
1	*IpatiaPlusJohnsonSU_BeautyMass_a2_combData_Signal_both_kpipi_2011*	1.982 ± 0.079	2.74 ± 0
2	*IpatiaPlusJohnsonSU_BeautyMass_fracI_combData_Signal_both_kpipi_2011*	0.403 ± 0.048	0.5 ± 0
3	*IpatiaPlusJohnsonSU_BeautyMass_l_combData_Signal_both_kpipi_2011*	-3.00 ± 0.49	-1.8 ± 0
4	*IpatiaPlusJohnsonSU_BeautyMass_mean_combData_Signal_both_kpipi_2011*	5279.608 ± 0.026	$(5.2795 \pm 0)e+03$
5	*IpatiaPlusJohnsonSU_BeautyMass_n2_combData_Signal_both_kpipi_2011*	2.684 ± 0.062	2.46 ± 0
6	*IpatiaPlusJohnsonSU_BeautyMass_nu_combData_Signal_both_kpipi_2011*	-0.221 ± 0.027	-0.46 ± 0
7	*IpatiaPlusJohnsonSU_BeautyMass_sigmaI_combData_Signal_both_kpipi_2011*	17.63 ± 0.65	20.7 ± 0
8	*IpatiaPlusJohnsonSU_BeautyMass_sigmaJ_combData_Signal_both_kpipi_2011*	16.20 ± 0.23	16.0 ± 0
9	*IpatiaPlusJohnsonSU_BeautyMass_tau_combData_Signal_both_kpipi_2011*	0.454 ± 0.013	0.4 ± 0

Table 17: Final fit parameters of fit to $B^0 \to D^- \pi^+$ signal 2011 MC between 5000 and 6000 GeV/c^2.

Parameter number	Parameter name	Fitted value	Initial value
0	*IpatiaPlusJohnsonSU_BeautyMass_a1_combData_Signal_both_kpipi_2012*	1.550 ± 0.081	1.5 ± 0
1	*IpatiaPlusJohnsonSU_BeautyMass_a2_combData_Signal_both_kpipi_2012*	2.75 ± 0.15	2.74 ± 0
2	*IpatiaPlusJohnsonSU_BeautyMass_fracI_combData_Signal_both_kpipi_2012*	0.492 ± 0.048	0.5 ± 0
3	*IpatiaPlusJohnsonSU_BeautyMass_l_combData_Signal_both_kpipi_2012*	-1.97 ± 0.10	-1.8 ± 0
4	*IpatiaPlusJohnsonSU_BeautyMass_mean_combData_Signal_both_kpipi_2012*	5279.539 ± 0.019	$(5.2795 \pm 0)e+03$
5	*IpatiaPlusJohnsonSU_BeautyMass_n2_combData_Signal_both_kpipi_2012*	2.435 ± 0.065	2.46 ± 0
6	*IpatiaPlusJohnsonSU_BeautyMass_nu_combData_Signal_both_kpipi_2012*	-0.411 ± 0.077	-0.46 ± 0
7	*IpatiaPlusJohnsonSU_BeautyMass_sigmaI_combData_Signal_both_kpipi_2012*	20.87 ± 0.60	20.7 ± 0
8	*IpatiaPlusJohnsonSU_BeautyMass_sigmaJ_combData_Signal_both_kpipi_2012*	16.11 ± 0.10	16.0 ± 0
9	*IpatiaPlusJohnsonSU_BeautyMass_tau_combData_Signal_both_kpipi_2012*	0.411 ± 0.018	0.4 ± 0

Table 18: Final fit parameters of fit to $B^0 \to D^- \pi^+$ signal 2012 MC between 5000 and 6000 GeV/c^2.

Parameter number	Parameter name	Fitted value	Initial value
0	*IpatiaPlusJohnsonSU_BeautyMass_a1_combData_Signal_both_kpipi_run2*	1.58 ± 0.12	1.58 ± 0
1	*IpatiaPlusJohnsonSU_BeautyMass_a2_combData_Signal_both_kpipi_run2*	2.97 ± 0.21	2.97 ± 0
2	*IpatiaPlusJohnsonSU_BeautyMass_fracI_combData_Signal_both_kpipi_run2*	0.593 ± 0.066	0.59 ± 0
3	*IpatiaPlusJohnsonSU_BeautyMass_l_combData_Signal_both_kpipi_run2*	-1.73 ± 0.12	-1.7 ± 0
4	*IpatiaPlusJohnsonSU_BeautyMass_mean_combData_Signal_both_kpipi_run2*	5279.736 ± 0.032	$(5.2797 \pm 0)e+03$
5	*IpatiaPlusJohnsonSU_BeautyMass_n2_combData_Signal_both_kpipi_run2*	1.979 ± 0.099	1.98 ± 0
6	*IpatiaPlusJohnsonSU_BeautyMass_nu_combData_Signal_both_kpipi_run2*	-0.87 ± 0.31	-0.87 ± 0
7	*IpatiaPlusJohnsonSU_BeautyMass_sigmaI_combData_Signal_both_kpipi_run2*	21.8 ± 1.1	21.8 ± 0
8	*IpatiaPlusJohnsonSU_BeautyMass_sigmaJ_combData_Signal_both_kpipi_run2*	16.34 ± 0.18	16.3 ± 0
9	*IpatiaPlusJohnsonSU_BeautyMass_tau_combData_Signal_both_kpipi_run2*	0.360 ± 0.037	0.36 ± 0

Table 19: Final fit parameters of fit to $B^0 \to D^- \pi^+$ signal Run 2 MC between 5000 and 6000 GeV/c^2.

A.2 Fit parameters of $D^-\pi^+$ fit

Parameter number	Parameter name	Fitted value	Initial value
0	$CombBkg\_BeautyMass\_cB2\_both\_kpipi\_run1$	-0.006001 ± 0.000098	-0.0061035 ± 0
1	$CombBkg\_BeautyMass\_frac\_both\_kpipi\_run1$	0.1486 ± 0.0054	0.25319 ± 0
2	$Signal\_BeautyMass\_a1\_both\_kpipi\_run1$	1.308 ± 0.017	1.4 ± 0
3	$Signal\_BeautyMass\_mean\_both\_all\_2011$	5277.848 ± 0.069	$(5.277505519 \pm 0)e+03$
4	$Signal\_BeautyMass\_mean\_both\_all\_2012$	5277.765 ± 0.088	$(5.277542923 \pm 0)e+03$
5	$Signal\_BeautyMass\_nu\_both\_kpipi\_2011$	-0.69 ± 0.15	-0.561962 ± 0
6	$Signal\_BeautyMass\_nu\_both\_kpipi\_2012$	-0.70 ± 0.55	-0.386332 ± 0
7	$Signal\_BeautyMass\_sigmaI\_both\_kpipi\_2011$	23.72 ± 0.39	20.115929 ± 0
8	$Signal\_BeautyMass\_sigmaI\_both\_kpipi\_2012$	23.14 ± 0.35	20.515388 ± 0
9	$Signal\_BeautyMass\_sigmaJ\_both\_kpipi\_2011$	16.59 ± 0.20	15.8412 ± 0
10	$Signal\_BeautyMass\_sigmaJ\_both\_kpipi\_2012$	16.07 ± 0.40	16.148366 ± 0
11	$Signal\_BeautyMass\_tau\_both\_kpipi\_2011$	0.290 ± 0.027	0.360295 ± 0
12	$Signal\_BeautyMass\_tau\_both\_kpipi\_2012$	0.296 ± 0.084	0.417146 ± 0
13	$nBd2DRho\_both\_kpipi\_2011\_Evts$	69954 ± 724	80000 ± 0
14	$nBd2DRho\_both\_kpipi\_2012\_Evts$	165177 ± 1262	160000 ± 0
15	$nBd2DstPi\_both\_kpipi\_2011\_Evts$	29851 ± 609	60000 ± 0
16	$nBd2DstPi\_both\_kpipi\_2012\_Evts$	77635 ± 982	120000 ± 0
17	$nCombBkg\_both\_kpipi\_2011\_Evts$	26865 ± 542	30000 ± 0
18	$nCombBkg\_both\_kpipi\_2012\_Evts$	74077 ± 1206	60000 ± 0
19	$nSig\_both\_kpipi\_2011\_Evts$	143575 ± 477	150000 ± 0
20	$nSig\_both\_kpipi\_2012\_Evts$	357781 ± 894	300000 ± 0
21	$relYield\_Bd2DK$	0.0097 ± 0.0010	0.0091 ± 0.0011
22	$relYield\_Bs2DsPi$	0.0080 ± 0.0018	0.00770 ± 0.00090
23	$relYield\_Lb2LcPi$	0.00382 ± 0.00050	0.0122 ± 0.0016

Table 20: Final fit parameters of fit to Run 1 $D^-\pi^+$ data.

Parameter number	Parameter name	Fitted value	Initial value
0	$CombBkg\_BeautyMass\_cB2\_both\_kpipi\_run2$	-0.006093 ± 0.000094	-0.0061035 ± 0
1	$CombBkg\_BeautyMass\_frac\_both\_kpipi\_run2$	0.2231 ± 0.0056	0.25319 ± 0
2	$Signal\_BeautyMass\_a1\_both\_kpipi\_run2$	1.282 ± 0.026	1.4 ± 0
3	$Signal\_BeautyMass\_mean\_both\_kpipi\_run2$	5278.156 ± 0.047	$(5.277736 \pm 0)e+03$
4	$Signal\_BeautyMass\_nu\_both\_kpipi\_run2$	-0.423 ± 0.032	-0.87306 ± 0
5	$Signal\_BeautyMass\_sigmaI\_both\_kpipi\_run2$	27.31 ± 0.44	21.757 ± 0
6	$Signal\_BeautyMass\_sigmaJ\_both\_kpipi\_run2$	16.57 ± 0.18	16.339 ± 0
7	$Signal\_BeautyMass\_tau\_both\_kpipi\_run2$	0.387 ± 0.014	0.35962 ± 0
8	$nBd2DRho\_both\_kpipi\_run2\_Evts$	260278 ± 2199	300000 ± 0
9	$nBd2DstPi\_both\_kpipi\_run2\_Evts$	132140 ± 1490	132000 ± 0
10	$nCombBkg\_both\_kpipi\_run2\_Evts$	167996 ± 2340	120000 ± 0
11	$nSig\_both\_kpipi\_run2\_Evts$	584975 ± 1540	700000 ± 0
12	$relYield\_Bd2DK$	0.0118 ± 0.0013	0.0099 ± 0.0012
13	$relYield\_Bs2DsPi$	0.00796 ± 0.00094	0.0079 ± 0.0010
14	$relYield\_Lb2LcPi$	0.00415 ± 0.00040	0.00400 ± 0.00050

Table 21: Final fit parameters of fit to Run 2 $D^-\pi^+$ data.

A.3 Fit parameters of $B_s^0 \to D_s^- \pi^+$ Monte Carlo signal

Parameter number	Parameter name	Fitted value	Initial value
0	$DCB\_BeautyMass\_alpha1\_combData\_Signal\_both\_all\_2011$	1.53 ± 0.11	1.657 ± 0
1	$DCB\_BeautyMass\_alpha2\_combData\_Signal\_both\_all\_2011$	-2.165 ± 0.073	-2.063 ± 0
2	$DCB\_BeautyMass\_frac\_combData\_Signal\_both\_all\_2011$	0.409 ± 0.048	0.499 ± 0
3	$DCB\_BeautyMass\_n1\_combData\_Signal\_both\_all\_2011$	1.337 ± 0.075	1.518 ± 0
4	$DCB\_BeautyMass\_n2\_combData\_Signal\_both\_all\_2011$	2.68 ± 0.24	2.3 ± 0
5	$DCB\_BeautyMass\_sigma1\_combData\_Signal\_both\_all\_2011$	10.83 ± 0.44	18.74 ± 0
6	$DCB\_BeautyMass\_sigma2\_combData\_Signal\_both\_all\_2011$	16.68 ± 0.43	12.23 ± 0
7	$Signal\_BeautyMass\_mean\_combData\_Signal\_both\_all\_2011$	5367.53 ± 0.12	$(5.36753 \pm 0)e+03$

Table 22: Double Crystal Ball fit parameters of fit to $B_s^0 \to D_s^- \pi^+$ signal MC between 5000 and 6000 GeV/c^2.

Parameter number	Parameter name	Fitted value	Initial value
0	$Ipatia\_BeautyMass\_a1\_combData\_Signal\_both\_all\_2011$	2.085 ± 0.022	2.005 ± 0
1	$Ipatia\_BeautyMass\_a2\_combData\_Signal\_both\_all\_2011$	3.11 ± 0.11	3.07 ± 0
2	$Ipatia\_BeautyMass\_l\_combData\_Signal\_both\_all\_2011$	-3.20 ± 0.10	-3.47 ± 0
3	$Ipatia\_BeautyMass\_mean\_combData\_Signal\_both\_all\_2011$	5367.084 ± 0.098	$(5.3671 \pm 0)e+03$
4	$Ipatia\_BeautyMass\_n1\_combData\_Signal\_both\_all\_2011$	1.279 ± 0.025	1.365 ± 0
5	$Ipatia\_BeautyMass\_n2\_combData\_Signal\_both\_all\_2011$	2.26 ± 0.14	2.26 ± 0
6	$Ipatia\_BeautyMass\_sigma\_combData\_Signal\_both\_all\_2011$	16.467 ± 0.097	16.871 ± 0

Table 23: Ipatia fit parameters of fit to $B_s^0 \to D_s^- \pi^+$ signal MC between 5000 and 6000 GeV/c^2.

Parameter number	Parameter name	Fitted value	Initial value
0	$IpatiaPlusGaussian\_BeautyMass\_a1\_combData\_Signal\_both\_all\_2011$	1.81 ± 0.17	1.775 ± 0
1	$IpatiaPlusGaussian\_BeautyMass\_a2\_combData\_Signal\_both\_all\_2011$	2.17 ± 0.24	2.14 ± 0
2	$IpatiaPlusGaussian\_BeautyMass\_fracI\_combData\_Signal\_both\_all\_2011$	0.65 ± 0.11	0.685 ± 0
3	$IpatiaPlusGaussian\_BeautyMass\_l\_combData\_Signal\_both\_all\_2011$	-6.8 ± 3.7	-6.2 ± 0
4	$IpatiaPlusGaussian\_BeautyMass\_mean\_combData\_Signal\_both\_all\_2011$	5367.22 ± 0.11	$(5.36722 \pm 0)e+03$
5	$IpatiaPlusGaussian\_BeautyMass\_n1\_combData\_Signal\_both\_all\_2011$	1.282 ± 0.089	1.343 ± 0
6	$IpatiaPlusGaussian\_BeautyMass\_n2\_combData\_Signal\_both\_all\_2011$	2.45 ± 0.27	2.65 ± 0
7	$IpatiaPlusGaussian\_BeautyMass\_sigmaG\_combData\_Signal\_both\_all\_2011$	17.5 ± 1.2	18.55 ± 0
8	$IpatiaPlusGaussian\_BeautyMass\_sigmaI\_combData\_Signal\_both\_all\_2011$	13.44 ± 0.73	14.0 ± 0

Table 24: Ipatia Plus Gaussian fit parameters of fit to $B_s^0 \to D_s^- \pi^+$ signal MC between 5000 and 6000 GeV/c^2.

Parameter number	Parameter name	Fitted value	Initial value
0	$IpatiaPlusJohnsonSU\_BeautyMass\_a1\_combData\_Signal\_both\_all\_2011$	0.40 ± 0.18	1.682 ± 0
1	$IpatiaPlusJohnsonSU\_BeautyMass\_a2\_combData\_Signal\_both\_all\_2011$	2.24 ± 0.51	2.75 ± 0
2	$IpatiaPlusJohnsonSU\_BeautyMass\_fracI\_combData\_Signal\_both\_all\_2011$	0.100 ± 0.025	0.539 ± 0
3	$IpatiaPlusJohnsonSU\_BeautyMass\_l\_combData\_Signal\_both\_all\_2011$	-1.84 ± 0.93	-2.34 ± 0
4	$IpatiaPlusJohnsonSU\_BeautyMass\_mean\_combData\_Signal\_both\_all\_2011$	5366.80 ± 0.13	$(5.36684 \pm 0)e+03$
5	$IpatiaPlusJohnsonSU\_BeautyMass\_n1\_combData\_Signal\_both\_all\_2011$	1.93 ± 0.29	1.21 ± 0
6	$IpatiaPlusJohnsonSU\_BeautyMass\_n2\_combData\_Signal\_both\_all\_2011$	1.96 ± 0.63	2.41 ± 0
7	$IpatiaPlusJohnsonSU\_BeautyMass\_nu\_combData\_Signal\_both\_all\_2011$	-0.316 ± 0.079	-0.4 ± 0
8	$IpatiaPlusJohnsonSU\_BeautyMass\_sigmaI\_combData\_Signal\_both\_all\_2011$	40.2 ± 7.7	18.59 ± 0
9	$IpatiaPlusJohnsonSU\_BeautyMass\_sigmaJ\_combData\_Signal\_both\_all\_2011$	15.22 ± 0.17	16.21 ± 0
10	$IpatiaPlusJohnsonSU\_BeautyMass\_tau\_combData\_Signal\_both\_all\_2011$	0.422 ± 0.026	0.437 ± 0

Table 25: Ipatia Plus JohnsonSU fit parameters of fit to $B_s^0 \to D_s^- \pi^+$ signal MC between 5000 and 6000 GeV/c^2.

Parameter number	Parameter name	Fitted value	Initial value
0	$IpatiaPlusJohnsonSU\_BeautyMass\_a1\_combData\_Signal\_both\_phipi\_run1$	1.58 ± 0.24	1.67 ± 0
1	$IpatiaPlusJohnsonSU\_BeautyMass\_a2\_combData\_Signal\_both\_phipi\_run1$	3.04 ± 0.24	3.062313 ± 0
2	$IpatiaPlusJohnsonSU\_BeautyMass\_fracI\_combData\_Signal\_both\_phipi\_run1$	0.55 ± 0.12	0.558356 ± 0
3	$IpatiaPlusJohnsonSU\_BeautyMass\_l\_combData\_Signal\_both\_phipi\_run1$	-1.77 ± 0.24	-2.031128 ± 0
4	$IpatiaPlusJohnsonSU\_BeautyMass\_mean\_combData\_Signal\_both\_phipi\_run1$	5366.695 ± 0.034	$(5.366716218 \pm 0)e+03$
5	$IpatiaPlusJohnsonSU\_BeautyMass\_n2\_combData\_Signal\_both\_phipi\_run1$	1.98 ± 0.11	2.018611 ± 0
6	$IpatiaPlusJohnsonSU\_BeautyMass\_nu\_combData\_Signal\_both\_phipi\_run1$	-0.68 ± 0.42	-0.647593 ± 0
7	$IpatiaPlusJohnsonSU\_BeautyMass\_sigmaI\_combData\_Signal\_both\_phipi\_run1$	20.9 ± 2.0	19.669586 ± 0
8	$IpatiaPlusJohnsonSU\_BeautyMass\_sigmaJ\_combData\_Signal\_both\_phipi\_run1$	15.37 ± 0.19	14.995451 ± 0
9	$IpatiaPlusJohnsonSU\_BeautyMass\_tau\_combData\_Signal\_both\_phipi\_run1$	0.345 ± 0.056	0.341644 ± 0

Table 26: Final fit parameters of fit to $B_s^0 \to D_s^- \pi^+$ signal Run 1 MC between 5000 and 6000 GeV/c^2.

Parameter number	Parameter name	Fitted value	Initial value
0	$IpatiaPlusJohnsonSU\_BeautyMass\_a1\_combData\_Signal\_both\_phipi\_run2$	1.55 ± 0.20	1.67 ± 0
1	$IpatiaPlusJohnsonSU\_BeautyMass\_a2\_combData\_Signal\_both\_phipi\_run2$	3.02 ± 0.25	3.062313 ± 0
2	$IpatiaPlusJohnsonSU\_BeautyMass\_fracI\_combData\_Signal\_both\_phipi\_run2$	0.632 ± 0.099	0.558356 ± 0
3	$IpatiaPlusJohnsonSU\_BeautyMass\_l\_combData\_Signal\_both\_phipi\_run2$	-1.66 ± 0.20	-2.031128 ± 0
4	$IpatiaPlusJohnsonSU\_BeautyMass\_mean\_combData\_Signal\_both\_phipi\_run2$	5366.923 ± 0.064	$(5.366716218 \pm 0)e+03$
5	$IpatiaPlusJohnsonSU\_BeautyMass\_n2\_combData\_Signal\_both\_phipi\_run2$	1.90 ± 0.15	2.018611 ± 0
6	$IpatiaPlusJohnsonSU\_BeautyMass\_nu\_combData\_Signal\_both\_phipi\_run2$	-1.5 ± 1.4	-0.647593 ± 0
7	$IpatiaPlusJohnsonSU\_BeautyMass\_sigmaI\_combData\_Signal\_both\_phipi\_run2$	21.5 ± 1.9	19.669586 ± 0
8	$IpatiaPlusJohnsonSU\_BeautyMass\_sigmaJ\_combData\_Signal\_both\_phipi\_run2$	15.49 ± 0.32	14.995451 ± 0
9	$IpatiaPlusJohnsonSU\_BeautyMass\_tau\_combData\_Signal\_both\_phipi\_run2$	0.276 ± 0.088	0.341644 ± 0

Table 27: Final fit parameters of fit to $B_s^0 \to D_s^- \pi^+$ signal Run 2 MC between 5000 and 6000 GeV/c^2.

A.4 Fit parameters of $D_s^- \pi^+$ fit

Parameter number	Parameter name	Fitted value	Initial value
0	$CombBkgRanDs\_BeautyMass\_cB\_both\_phipi\_run1$	-0.00380 ± 0.00013	-0.0035132 ± 0
1	$CombBkgRanDs\_CharmMass\_cB\_both\_phipi\_run1$	-0.00618 ± 0.00055	-0.0057273 ± 0
2	$CombBkgTrueDs\_BeautyMass\_cB1\_both\_phipi\_run1$	-0.0085 ± 0.0015	-0.030873 ± 0
3	$CombBkgTrueDs\_BeautyMass\_frac\_both\_phipi\_run1$	0.833 ± 0.042	0.654 ± 0
4	$CombBkgTrueDs\_CharmMass\_R\_both\_phipi\_run1$	1.65 ± 0.18	1.0 ± 0
5	$Signal\_BeautyMass\_a1\_both\_phipi\_run1$	1.397 ± 0.073	1.30 ± 0.10
6	$Signal\_BeautyMass\_mean\_both\_phipi\_run1$	5364.87 ± 0.12	$(5.364695 \pm 0)e+03$
7	$Signal\_BeautyMass\_nu\_both\_phipi\_run1$	-0.45 ± 0.13	-0.68277 ± 0
8	$Signal\_BeautyMass\_sigmaI\_both\_phipi\_run1$	22.05 ± 0.71	20.935 ± 0
9	$Signal\_BeautyMass\_sigmaJ\_both\_phipi\_run1$	16.68 ± 0.33	15.373 ± 0
10	$Signal\_CharmMass\_R\_both\_phipi\_run1$	1.0446 ± 0.0052	1.0 ± 0
11	$Signal\_CharmMass\_mean\_both\_phipi\_run1$	1969.704 ± 0.029	$(1.968933 \pm 0)e+03$
12	$g1\_f1\_frac\_both\_all\_run1$	0.655 ± 0.018	0.5 ± 0
13	$nBd2DsPi\_both\_phipi\_run1\_Evts$	1035 ± 118	1000 ± 0
14	$nBs2DsDsstPiRho\_both\_phipi\_run1\_Evts$	23854 ± 446	30000 ± 0
15	$nCombBkgRanDs\_both\_phipi\_run1\_Evts$	4534 ± 145	30000 ± 0
16	$nCombBkgTrueDs\_both\_phipi\_run1\_Evts$	2729 ± 482	30000 ± 0
17	$nSig\_both\_phipi\_run1\_Evts$	36606 ± 238	30000 ± 0
18	$relYield\_Bs2DsK$	0.00863 ± 0.00099	0.0090 ± 0.0010
19	$relYield\_Lb2LcPi$	0.00247 ± 0.00033	0.00197 ± 0.00034

Table 28: Final fit parameters of fit to Run 1 $D_s^- \pi^+$ data.

Parameter number	Parameter name	Fitted value	Initial value
0	$CombBkgRanDs\_BeautyMass\_cB\_both\_phipi\_run2$	-0.00345 ± 0.00011	-0.0035132 ± 0
1	$CombBkgRanDs\_CharmMass\_cB\_both\_phipi\_run2$	-0.00684 ± 0.00048	-0.0057273 ± 0
2	$CombBkgTrueDs\_BeautyMass\_cB1\_both\_phipi\_run2$	-0.0084 ± 0.0016	-0.030873 ± 0
3	$CombBkgTrueDs\_BeautyMass\_frac\_both\_phipi\_run2$	0.714 ± 0.071	0.654 ± 0
4	$CombBkgTrueDs\_CharmMass\_R\_both\_phipi\_run2$	1.43 ± 0.13	1.0 ± 0
5	$Signal\_BeautyMass\_a1\_both\_phipi\_run2$	1.173 ± 0.074	1.30 ± 0.10
6	$Signal\_BeautyMass\_mean\_both\_phipi\_run2$	5365.757 ± 0.098	$(5.364923 \pm 0)e+03$
7	$Signal\_BeautyMass\_nu\_both\_phipi\_run2$	-0.35 ± 0.14	-1.5146 ± 0
8	$Signal\_BeautyMass\_sigmaI\_both\_phipi\_run2$	28.0 ± 1.0	21.54 ± 0
9	$Signal\_BeautyMass\_sigmaJ\_both\_phipi\_run2$	15.37 ± 0.22	15.491 ± 0
10	$Signal\_CharmMass\_R\_both\_phipi\_run2$	1.0477 ± 0.0049	1.0 ± 0
11	$Signal\_CharmMass\_mean\_both\_phipi\_run2$	1968.835 ± 0.025	$(1.969071 \pm 0)e+03$
12	$g1\_f1\_frac\_both\_all\_run2$	0.658 ± 0.016	0.5 ± 0
13	$nBd2DsPi\_both\_phipi\_run2\_Evts$	1648 ± 157	1250 ± 0
14	$nBs2DsDsstPiRho\_both\_phipi\_run2\_Evts$	32746 ± 555	30000 ± 0
15	$nCombBkgRanDs\_both\_phipi\_run2\_Evts$	5941 ± 157	6000 ± 0
16	$nCombBkgTrueDs\_both\_phipi\_run2\_Evts$	3324 ± 695	3500 ± 0
17	$nSig\_both\_phipi\_run2\_Evts$	49021 ± 313	45000 ± 0
18	$relYield\_Bs2DsK$	0.0099 ± 0.0011	0.0096 ± 0.0011
19	$relYield\_Lb2LcPi$	0.000283 ± 0.000040	0.000270 ± 0.000040

Table 29: Final fit parameters of fit to Run 2 $D_s^- \pi^+$ data.

A.5 Magnet Polarity check $D^-\pi^+$ fit

Parameter number	Parameter name	Fitted value	Initial value
0	$CombBkg\_BeautyMass\_cB2\_both\_kpipi\_run1$	-0.00595 ± 0.00018	-0.0061035 ± 0
1	$CombBkg\_BeautyMass\_frac\_both\_kpipi\_run1$	0.155 ± 0.011	0.25319 ± 0
2	$Signal\_BeautyMass\_a1\_both\_kpipi\_run1$	1.295 ± 0.027	1.4 ± 0
3	$Signal\_BeautyMass\_mean\_both\_all\_2011$	5277.863 ± 0.081	$(5.277505519 \pm 0)e+03$
4	$Signal\_BeautyMass\_mean\_both\_all\_2012$	5277.720 ± 0.061	$(5.277542923 \pm 0)e+03$
5	$Signal\_BeautyMass\_nu\_both\_kpipi\_2011$	-0.66 ± 0.19	-0.561962 ± 0
6	$Signal\_BeautyMass\_nu\_both\_kpipi\_2012$	-0.66 ± 0.13	-0.386332 ± 0
7	$Signal\_BeautyMass\_sigmaI\_both\_kpipi\_2011$	24.15 ± 0.63	20.115929 ± 0
8	$Signal\_BeautyMass\_sigmaI\_both\_kpipi\_2012$	23.13 ± 0.47	20.515388 ± 0
9	$Signal\_BeautyMass\_sigmaJ\_both\_kpipi\_2011$	16.31 ± 0.35	15.8412 ± 0
10	$Signal\_BeautyMass\_sigmaJ\_both\_kpipi\_2012$	16.11 ± 0.29	16.148366 ± 0
11	$Signal\_BeautyMass\_tau\_both\_kpipi\_2011$	0.291 ± 0.037	0.360295 ± 0
12	$Signal\_BeautyMass\_tau\_both\_kpipi\_2012$	0.302 ± 0.028	0.417146 ± 0
13	$nBd2DRho\_down\_kpipi\_2011\_Evts$	41388 ± 697	80000 ± 0
14	$nBd2DRho\_down\_kpipi\_2012\_Evts$	85689 ± 1184	160000 ± 0
15	$nBd2DstPi\_down\_kpipi\_2011\_Evts$	17593 ± 549	60000 ± 0
16	$nBd2DstPi\_down\_kpipi\_2012\_Evts$	37862 ± 820	120000 ± 0
17	$nCombBkg\_down\_kpipi\_2011\_Evts$	15009 ± 568	30000 ± 0
18	$nCombBkg\_down\_kpipi\_2012\_Evts$	36326 ± 1196	60000 ± 0
19	$nSig\_down\_kpipi\_2011\_Evts$	84551 ± 381	150000 ± 0
20	$nSig\_down\_kpipi\_2012\_Evts$	180957 ± 676	300000 ± 0
21	$relYield\_Bd2DK$	0.0093 ± 0.0011	0.0091 ± 0.0011
22	$relYield\_Bs2DsPi$	0.00783 ± 0.00090	0.00770 ± 0.00090
23	$relYield\_Lb2LcPi$	0.00459 ± 0.00076	0.0122 ± 0.0016

Table 30: Magnet polarity check Run 1 $D^-\pi^+$ *MagDown*.

Parameter number	Parameter name	Fitted value	Initial value
0	$CombBkg\_BeautyMass\_cB2\_both\_kpipi\_run1$	-0.00627 ± 0.00019	-0.0061035 ± 0
1	$CombBkg\_BeautyMass\_frac\_both\_kpipi\_run1$	0.162 ± 0.010	0.25319 ± 0
2	$Signal\_BeautyMass\_a1\_both\_kpipi\_run1$	1.278 ± 0.027	1.4 ± 0
3	$Signal\_BeautyMass\_mean\_both\_all\_2011$	5277.84 ± 0.10	$(5.277505519 \pm 0)e+03$
4	$Signal\_BeautyMass\_mean\_both\_all\_2012$	5277.815 ± 0.062	$(5.277542923 \pm 0)e+03$
5	$Signal\_BeautyMass\_nu\_both\_kpipi\_2011$	-0.71 ± 0.23	-0.561962 ± 0
6	$Signal\_BeautyMass\_nu\_both\_kpipi\_2012$	-0.77 ± 0.54	-0.386332 ± 0
7	$Signal\_BeautyMass\_sigmaI\_both\_kpipi\_2011$	23.10 ± 0.68	20.115929 ± 0
8	$Signal\_BeautyMass\_sigmaI\_both\_kpipi\_2012$	23.30 ± 0.40	20.515388 ± 0
9	$Signal\_BeautyMass\_sigmaJ\_both\_kpipi\_2011$	17.00 ± 0.39	15.8412 ± 0
10	$Signal\_BeautyMass\_sigmaJ\_both\_kpipi\_2012$	15.94 ± 0.22	16.148366 ± 0
11	$Signal\_BeautyMass\_tau\_both\_kpipi\_2011$	0.286 ± 0.044	0.360295 ± 0
12	$Signal\_BeautyMass\_tau\_both\_kpipi\_2012$	0.278 ± 0.020	0.417146 ± 0
13	$nBd2DRho\_up\_kpipi\_2011\_Evts$	28855 ± 577	80000 ± 0
14	$nBd2DRho\_up\_kpipi\_2012\_Evts$	80367 ± 1189	160000 ± 0
15	$nBd2DstPi\_up\_kpipi\_2011\_Evts$	12247 ± 458	60000 ± 0
16	$nBd2DstPi\_up\_kpipi\_2012\_Evts$	39549 ± 799	120000 ± 0
17	$nCombBkg\_up\_kpipi\_2011\_Evts$	11199 ± 456	30000 ± 0
18	$nCombBkg\_up\_kpipi\_2012\_Evts$	36008 ± 1247	60000 ± 0
19	$nSig\_up\_kpipi\_2011\_Evts$	59303 ± 304	150000 ± 0
20	$nSig\_up\_kpipi\_2012\_Evts$	177651 ± 669	300000 ± 0
21	$relYield\_Bd2DK$	0.0093 ± 0.0011	0.0091 ± 0.0011
22	$relYield\_Bs2DsPi$	0.00801 ± 0.00088	0.00770 ± 0.00090
23	$relYield\_Lb2LcPi$	0.00533 ± 0.00077	0.0122 ± 0.0016

Table 31: Magnet polarity check Run 1 $D^-\pi^+$ *MagUp*.

Parameter number	Parameter name	Fitted value	Initial value
0	$CombBkg\_BeautyMass\_cB2\_both\_kpipi\_run2$	-0.00610 ± 0.00013	-0.0061035 ± 0
1	$CombBkg\_BeautyMass\_frac\_both\_kpipi\_run2$	0.2224 ± 0.0076	0.25319 ± 0
2	$Signal\_BeautyMass\_a1\_both\_kpipi\_run2$	1.269 ± 0.033	1.4 ± 0
3	$Signal\_BeautyMass\_mean\_both\_kpipi\_run2$	5278.165 ± 0.054	$(5.277736 \pm 0)e+03$
4	$Signal\_BeautyMass\_nu\_both\_kpipi\_run2$	-0.408 ± 0.043	-0.87306 ± 0
5	$Signal\_BeautyMass\_sigmaI\_both\_kpipi\_run2$	27.40 ± 0.56	21.757 ± 0
6	$Signal\_BeautyMass\_sigmaJ\_both\_kpipi\_run2$	16.53 ± 0.22	16.339 ± 0
7	$Signal\_BeautyMass\_tau\_both\_kpipi\_run2$	0.381 ± 0.018	0.35962 ± 0
8	$nBd2DRho\_down\_kpipi\_run2\_Evts$	135996 ± 1636	300000 ± 0
9	$nBd2DstPi\_down\_kpipi\_run2\_Evts$	69293 ± 1090	132000 ± 0
10	$nCombBkg\_down\_kpipi\_run2\_Evts$	88644 ± 1744	120000 ± 0
11	$nSig\_down\_kpipi\_run2\_Evts$	307127 ± 1007	700000 ± 0
12	$relYield\_Bd2DK$	0.0109 ± 0.0012	0.0099 ± 0.0012
13	$relYield\_Bs2DsPi$	0.00785 ± 0.00097	0.0079 ± 0.0010
14	$relYield\_Lb2LcPi$	0.00394 ± 0.00044	0.00400 ± 0.00050

Table 32: Magnet polarity check Run 2 $D^-\pi^+$ *MagDown*.

Parameter number	Parameter name	Fitted value	Initial value
0	$CombBkg\_BeautyMass\_cB2\_both\_kpipi\_run2$	-0.00609 ± 0.00013	-0.0061035 ± 0
1	$CombBkg\_BeautyMass\_frac\_both\_kpipi\_run2$	0.2231 ± 0.0080	0.25319 ± 0
2	$Signal\_BeautyMass\_a1\_both\_kpipi\_run2$	1.290 ± 0.037	1.4 ± 0
3	$Signal\_BeautyMass\_mean\_both\_kpipi\_run2$	5278.096 ± 0.057	$(5.277736 \pm 0)e+03$
4	$Signal\_BeautyMass\_nu\_both\_kpipi\_run2$	-0.441 ± 0.043	-0.87306 ± 0
5	$Signal\_BeautyMass\_sigmaI\_both\_kpipi\_run2$	27.03 ± 0.61	21.757 ± 0
6	$Signal\_BeautyMass\_sigmaJ\_both\_kpipi\_run2$	16.77 ± 0.25	16.339 ± 0
7	$Signal\_BeautyMass\_tau\_both\_kpipi\_run2$	0.404 ± 0.019	0.35962 ± 0
8	$nBd2DRho\_up\_kpipi\_run2\_Evts$	124327 ± 1567	300000 ± 0
9	$nBd2DstPi\_up\_kpipi\_run2\_Evts$	62541 ± 1050	132000 ± 0
10	$nCombBkg\_up\_kpipi\_run2\_Evts$	79703 ± 1671	120000 ± 0
11	$nSig\_up\_kpipi\_run2\_Evts$	278310 ± 939	700000 ± 0
12	$relYield\_Bd2DK$	0.0109 ± 0.0012	0.0099 ± 0.0012
13	$relYield\_Bs2DsPi$	0.00805 ± 0.00097	0.0079 ± 0.0010
14	$relYield\_Lb2LcPi$	0.00429 ± 0.00044	0.00400 ± 0.00050

Table 33: Magnet polarity check Run 2 $D^-\pi^+$ *MagUp*.

A.6 Magnet Polarity Check $D_s^-\pi^+$ fit

Parameter number	Parameter name	Fitted value	Initial value
0	$CombBkgRanDs\_BeautyMass\_cB\_both\_phipi\_run1$	-0.00379 ± 0.00016	-0.0035132 ± 0
1	$CombBkgRanDs\_CharmMass\_cB\_both\_phipi\_run1$	-0.00736 ± 0.00069	-0.0057273 ± 0
2	$CombBkgTrueDs\_BeautyMass\_cB1\_both\_phipi\_run1$	-0.0156 ± 0.0063	-0.030873 ± 0
3	$CombBkgTrueDs\_BeautyMass\_frac\_both\_phipi\_run1$	0.810 ± 0.071	0.654 ± 0
4	$CombBkgTrueDs\_CharmMass\_R\_both\_phipi\_run1$	1.14 ± 0.21	1.0 ± 0
5	$Signal\_BeautyMass\_a1\_both\_phipi\_run1$	1.344 ± 0.083	1.30 ± 0.10
6	$Signal\_BeautyMass\_mean\_both\_phipi\_run1$	5364.79 ± 0.15	$(5.364695 \pm 0)e+03$
7	$Signal\_BeautyMass\_nu\_both\_phipi\_run1$	-0.41 ± 0.17	-0.68277 ± 0
8	$Signal\_BeautyMass\_sigmaI\_both\_phipi\_run1$	22.2 ± 1.0	20.935 ± 0
9	$Signal\_BeautyMass\_sigmaJ\_both\_phipi\_run1$	16.42 ± 0.42	15.373 ± 0
10	$Signal\_CharmMass\_R\_both\_phipi\_run1$	1.0507 ± 0.0089	1.0 ± 0
11	$Signal\_CharmMass\_mean\_both\_phipi\_run1$	1969.650 ± 0.039	$(1.968933 \pm 0)e+03$
12	$g1\_f1\_frac\_both\_all\_run1$	0.687 ± 0.039	0.5 ± 0
13	$nBd2DsPi\_down\_phipi\_run1\_Evts$	513 ± 86	1000 ± 0
14	$nBs2DsDsstPiRho\_down\_phipi\_run1\_Evts$	12344 ± 399	30000 ± 0
15	$nCombBkgRanDs\_down\_phipi\_run1\_Evts$	2485 ± 92	30000 ± 0
16	$nCombBkgTrueDs\_down\_phipi\_run1\_Evts$	1436 ± 459	30000 ± 0
17	$nSig\_down\_phipi\_run1\_Evts$	19634 ± 194	30000 ± 0
18	$relYield\_Bs2DsK$	0.00881 ± 0.00099	0.0090 ± 0.0010
19	$relYield\_Lb2LcPi$	0.00219 ± 0.00033	0.00197 ± 0.00034

Table 34: Magnet polarity check Run 1 $D_s^-\pi^+$ *MagDown*.

Parameter number	Parameter name	Fitted value	Initial value
0	$CombBkgRanDs\_BeautyMass\_cB\_both\_phipi\_run1$	-0.00380 ± 0.00018	-0.0035132 ± 0
1	$CombBkgRanDs\_CharmMass\_cB\_both\_phipi\_run1$	-0.00547 ± 0.00078	-0.0057273 ± 0
2	$CombBkgTrueDs\_BeautyMass\_cB1\_both\_phipi\_run1$	-0.0085 ± 0.0017	-0.030873 ± 0
3	$CombBkgTrueDs\_BeautyMass\_frac\_both\_phipi\_run1$	0.867 ± 0.048	0.654 ± 0
4	$CombBkgTrueDs\_CharmMass\_R\_both\_phipi\_run1$	1.66 ± 0.20	1.0 ± 0
5	$Signal\_BeautyMass\_a1\_both\_phipi\_run1$	1.374 ± 0.082	1.30 ± 0.10
6	$Signal\_BeautyMass\_mean\_both\_phipi\_run1$	5365.02 ± 0.17	$(5.364695 \pm 0)e+03$
7	$Signal\_BeautyMass\_nu\_both\_phipi\_run1$	-0.42 ± 0.18	-0.68277 ± 0
8	$Signal\_BeautyMass\_sigmaI\_both\_phipi\_run1$	22.6 ± 1.2	20.935 ± 0
9	$Signal\_BeautyMass\_sigmaJ\_both\_phipi\_run1$	16.71 ± 0.53	15.373 ± 0
10	$Signal\_CharmMass\_R\_both\_phipi\_run1$	1.0465 ± 0.0077	1.0 ± 0
11	$Signal\_CharmMass\_mean\_both\_phipi\_run1$	1969.769 ± 0.042	$(1.968933 \pm 0)e+03$
12	$g1\_f1\_frac\_both\_all\_run1$	0.649 ± 0.027	0.5 ± 0
13	$nBd2DsPi\_up\_phipi\_run1\_Evts$	490 ± 81	1000 ± 0
14	$nBs2DsDsstPiRho\_up\_phipi\_run1\_Evts$	11061 ± 313	30000 ± 0
15	$nCombBkgRanDs\_up\_phipi\_run1\_Evts$	2174 ± 93	30000 ± 0
16	$nCombBkgTrueDs\_up\_phipi\_run1\_Evts$	1540 ± 348	30000 ± 0
17	$nSig\_up\_phipi\_run1\_Evts$	17083 ± 158	30000 ± 0
18	$relYield\_Bs2DsK$	0.00880 ± 0.00099	0.0090 ± 0.0010
19	$relYield\_Lb2LcPi$	0.00226 ± 0.00033	0.00197 ± 0.00034

Table 35: Magnet polarity check Run 1 $D_s^-\pi^+$ *MagUp*.

Parameter number	Parameter name	Fitted value	Initial value
0	$CombBkgRanDs\_BeautyMass\_cB\_both\_phipi\_run2$	-0.00359 ± 0.00015	-0.0035132 ± 0
1	$CombBkgRanDs\_CharmMass\_cB\_both\_phipi\_run2$	-0.00623 ± 0.00065	-0.0057273 ± 0
2	$CombBkgTrueDs\_BeautyMass\_cB1\_both\_phipi\_run2$	-0.0085 ± 0.0016	-0.030873 ± 0
3	$CombBkgTrueDs\_BeautyMass\_frac\_both\_phipi\_run2$	0.735 ± 0.082	0.654 ± 0
4	$CombBkgTrueDs\_CharmMass\_R\_both\_phipi\_run2$	1.47 ± 0.14	1.0 ± 0
5	$Signal\_BeautyMass\_a1\_both\_phipi\_run2$	1.259 ± 0.086	1.30 ± 0.10
6	$Signal\_BeautyMass\_mean\_both\_phipi\_run2$	5365.62 ± 0.13	$(5.364923 \pm 0)e+03$
7	$Signal\_BeautyMass\_nu\_both\_phipi\_run2$	-0.46 ± 0.19	-1.5146 ± 0
8	$Signal\_BeautyMass\_sigmaI\_both\_phipi\_run2$	27.4 ± 1.3	21.54 ± 0
9	$Signal\_BeautyMass\_sigmaJ\_both\_phipi\_run2$	15.40 ± 0.31	15.491 ± 0
10	$Signal\_CharmMass\_R\_both\_phipi\_run2$	1.0441 ± 0.0066	1.0 ± 0
11	$Signal\_CharmMass\_mean\_both\_phipi\_run2$	1968.784 ± 0.034	$(1.969071 \pm 0)e+03$
12	$g1\_f1\_frac\_both\_all\_run2$	0.652 ± 0.023	0.5 ± 0
13	$nBd2DsPi\_down\_phipi\_run2\_Evts$	897 ± 112	1250 ± 0
14	$nBs2DsDsstPiRho\_down\_phipi\_run2\_Evts$	17015 ± 381	30000 ± 0
15	$nCombBkgRanDs\_down\_phipi\_run2\_Evts$	3116 ± 108	6000 ± 0
16	$nCombBkgTrueDs\_down\_phipi\_run2\_Evts$	1953 ± 478	3500 ± 0
17	$nSig\_down\_phipi\_run2\_Evts$	25578 ± 209	45000 ± 0
18	$relYield\_Bs2DsK$	0.0097 ± 0.0011	0.0096 ± 0.0011
19	$relYield\_Lb2LcPi$	0.000277 ± 0.000040	0.000270 ± 0.000040

Table 36: Magnet polarity check Run 2 $D_s^-\pi^+$ *MagDown*.

Parameter number	Parameter name	Fitted value	Initial value
0	$CombBkgRanDs\_BeautyMass\_cB\_both\_phipi\_run2$	-0.00326 ± 0.00015	-0.0035132 ± 0
1	$CombBkgRanDs\_CharmMass\_cB\_both\_phipi\_run2$	-0.00794 ± 0.00062	-0.0057273 ± 0
2	$CombBkgTrueDs\_BeautyMass\_cB1\_both\_phipi\_run2$	-0.0153 ± 0.0097	-0.030873 ± 0
3	$CombBkgTrueDs\_BeautyMass\_frac\_both\_phipi\_run2$	0.56 ± 0.32	0.654 ± 0
4	$CombBkgTrueDs\_CharmMass\_R\_both\_phipi\_run2$	1.03 ± 0.18	1.0 ± 0
5	$Signal\_BeautyMass\_a1\_both\_phipi\_run2$	1.178 ± 0.097	1.30 ± 0.10
6	$Signal\_BeautyMass\_mean\_both\_phipi\_run2$	5365.84 ± 0.14	$(5.364923 \pm 0)e+03$
7	$Signal\_BeautyMass\_nu\_both\_phipi\_run2$	-0.35 ± 0.19	-1.5146 ± 0
8	$Signal\_BeautyMass\_sigmaI\_both\_phipi\_run2$	30.2 ± 1.5	21.54 ± 0
9	$Signal\_BeautyMass\_sigmaJ\_both\_phipi\_run2$	15.14 ± 0.27	15.491 ± 0
10	$Signal\_CharmMass\_R\_both\_phipi\_run2$	1.0582 ± 0.0062	1.0 ± 0
11	$Signal\_CharmMass\_mean\_both\_phipi\_run2$	1968.892 ± 0.036	$(1.969071 \pm 0)e+03$
12	$g1\_f1\_frac\_both\_all\_run2$	0.672 ± 0.027	0.5 ± 0
13	$nBd2DsPi\_up\_phipi\_run2\_Evts$	845 ± 123	1250 ± 0
14	$nBs2DsDsstPiRho\_up\_phipi\_run2\_Evts$	15852 ± 610	30000 ± 0
15	$nCombBkgRanDs\_up\_phipi\_run2\_Evts$	2920 ± 90	6000 ± 0
16	$nCombBkgTrueDs\_up\_phipi\_run2\_Evts$	1017 ± 777	3500 ± 0
17	$nSig\_up\_phipi\_run2\_Evts$	23493 ± 230	45000 ± 0
18	$relYield\_Bs2DsK$	0.0099 ± 0.0011	0.0096 ± 0.0011
19	$relYield\_Lb2LcPi$	0.000276 ± 0.000040	0.000270 ± 0.000040

Table 37: Magnet polarity check Run 2 $D_s^-\pi^+$ *MagUp*.

B Definitions of Probability density functions

Gausian function

$$f(m, \mu, \sigma) = \frac{1}{\sigma\sqrt{2\pi}} e^{-\frac{(m-\mu)^2}{2\sigma^2}}$$

Crystal Ball Function

$$f(m, \alpha, n, \mu, \sigma) \propto \cdot \begin{cases} \exp(-\frac{(x-\mu)^2}{2\sigma^2}), & \text{for } \frac{m-\mu}{\sigma} > -\alpha \\ A \cdot (B - \frac{x-\mu}{\sigma})^{-n}, & \text{for } \frac{m-\mu}{\sigma} \leq -\alpha \end{cases}$$

$$A = \left(\frac{n}{|\alpha|}\right)^n \cdot \exp\left(-\frac{|\alpha|^2}{2}\right)$$
$$B = \frac{n}{|\alpha|} - |\alpha|$$

Ipatia

$$h(m, \mu, \sigma, \lambda, \zeta, \beta) \propto ((m-\mu)^2 + A_\lambda^2(\zeta)\sigma^2)^{\frac{1}{2}\lambda - \frac{1}{4}} e^{\beta(m-\mu)} K_{\lambda-\frac{1}{2}}\left(\zeta\sqrt{1 + \left(\frac{m-\mu}{A_\lambda(\zeta)\sigma}\right)^2}\right)$$

$$H(m, \mu, \sigma, \lambda, \zeta, \beta, a_1, n_1, a_2, n2) \propto \begin{cases} h(m, \mu, \sigma, \lambda, \zeta, \beta), & \text{if } \frac{m-\mu}{\sigma} > -a_1 \text{ or } \frac{m-\mu}{\sigma} < a_2, \\ \frac{h(m-a_1\sigma, \mu, \sigma, \lambda, \zeta, \beta)}{\left(1 - m/\left(n\frac{h(m-a_1\sigma, \mu, \sigma, \lambda, \zeta, \beta)}{h'(m-a_1\sigma, \mu, \sigma, \lambda, \zeta, \beta)} - a_1\sigma\right)\right)^{n_1}}, & \text{if } \frac{m-\mu}{\sigma} \leq -a_1 \\ \frac{h(m-a_2\sigma, \mu, \sigma, \lambda, \zeta, \beta)}{\left(1 - m/\left(n\frac{h(m-a_2\sigma, \mu, \sigma, \lambda, \zeta, \beta)}{h'(m-a_2\sigma, \mu, \sigma, \lambda, \zeta, \beta)} - a_2\sigma\right)\right)^{n_2}}, & \text{if } \frac{m-\mu}{\sigma} \geq a_2. \end{cases}$$

Johnson SU

$$J(m, \mu, \sigma, \nu, \tau) \propto \frac{1}{2\pi c(\nu, \tau)\sigma} e^{-\frac{1}{2}r(m, \mu, \sigma, \nu, \tau)^2} \frac{1}{\tau\sqrt{z(m, \mu, \sigma, \nu, \tau)^2 + 1}}$$

$$w = e^{\tau^2}$$
$$\omega = -\nu\tau$$
$$c = \frac{1}{\sqrt{\frac{1}{2}(w-1)(w\cosh 2\omega + 1)}}$$
$$z = \frac{m - (\mu + c + \sigma\sqrt{w}\sinh\omega)}{c\sigma}$$
$$r = -\nu + \frac{\sinh z^{-1}}{\tau}$$

C Particle identification reweighing histograms

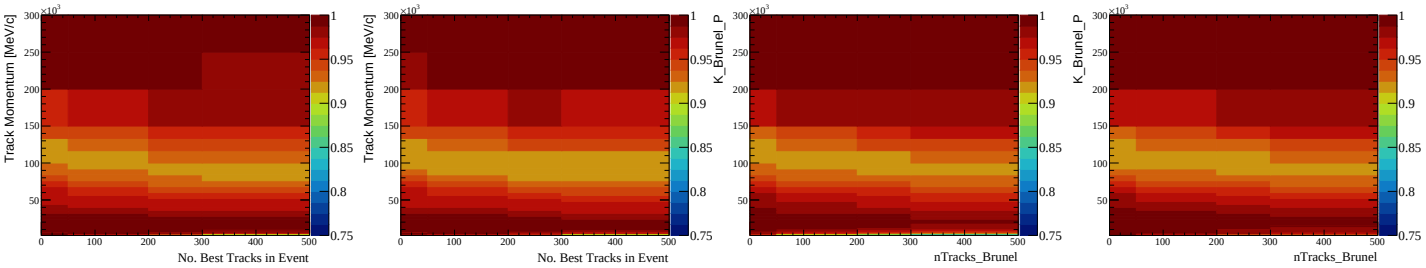

(a) 2012 *MagDown* (b) 2012 *MagUp* (c) 2016 *MagDown* (d) 2016 *MagUp*

Figure 26: PID reweighing histograms of $\mathrm{DLL}_{K\pi} > -2$ cut on kaons.

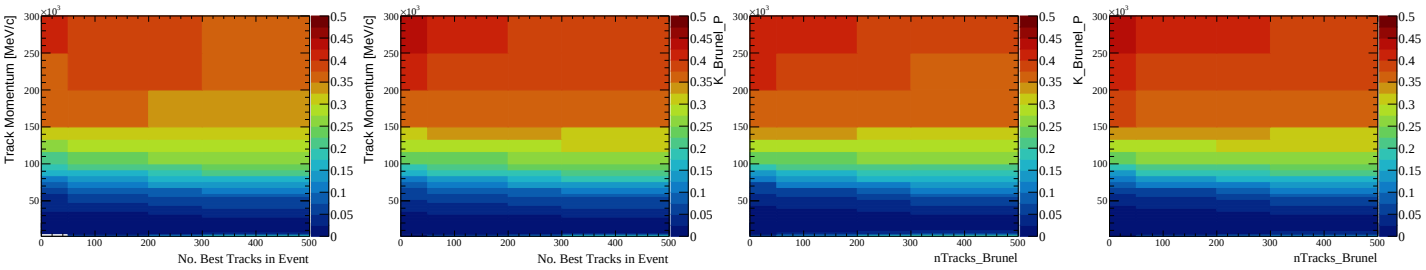

(a) 2012 *MagDown* (b) 2012 *MagUp* (c) 2016 *MagDown* (d) 2016 *MagUp*

Figure 27: PID reweighing histograms of $\mathrm{DLL}_{\mu\pi} < 0$ & $\mathrm{DLL}_{K\pi} < 0$ cut on kaons.

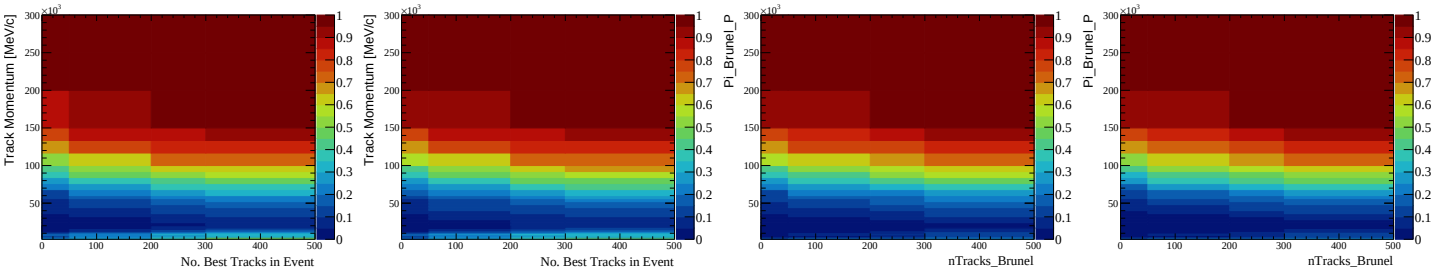

(a) 2012 *MagDown* (b) 2012 *MagUp* (c) 2016 *MagDown* (d) 2016 *MagUp*

Figure 28: PID reweighing histograms of $\mathrm{DLL}_{K\pi} > -2$ cut on pions.

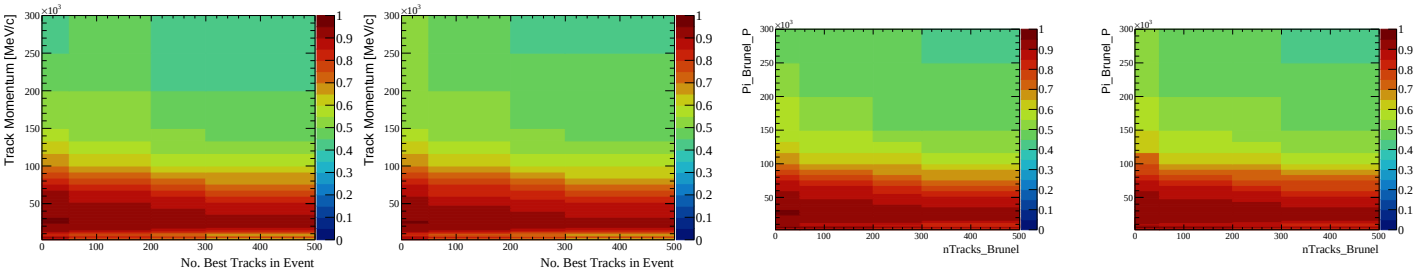

(a) 2012 *MagDown* (b) 2012 *MagUp* (c) 2016 *MagDown* (d) 2016 *MagUp*

Figure 29: PID reweighing histograms of $\mathrm{DLL}_{\mu\pi} < 0$ & $\mathrm{DLL}_{K\pi} < 0$ cut on pions.

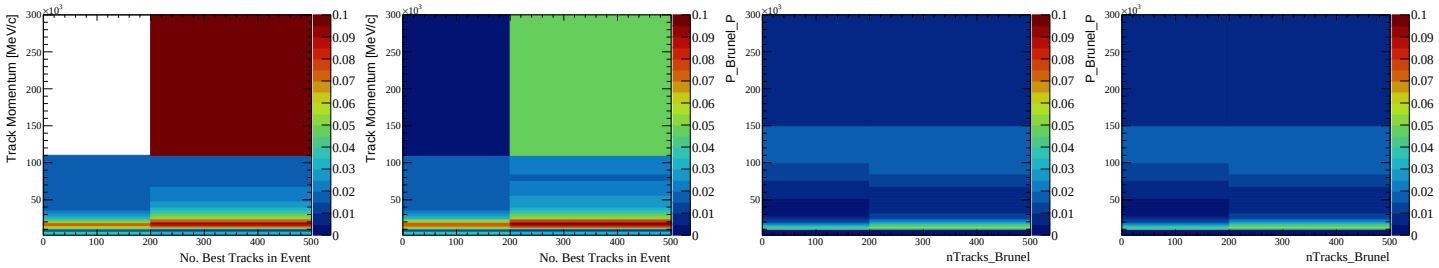

(a) 2012 *MagDown* (b) 2012 *MagUp* (c) 2016 *MagDown* (d) 2016 *MagUp*

Figure 30: PID reweighing histograms of $\mathrm{DLL}_{K\pi} > -2$ & $\mathrm{DLL}_{K\pi} - \mathrm{DLL}_{p\pi} > 5$ cut on protons.

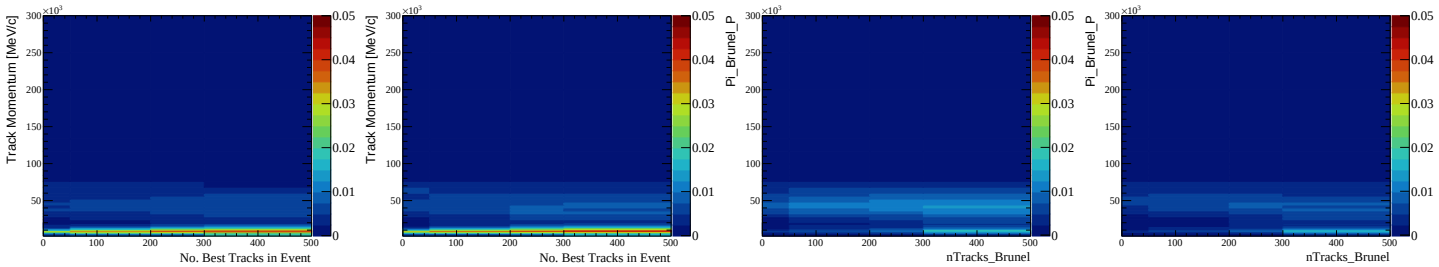

(a) 2012 *MagDown* (b) 2012 *MagUp* (c) 2016 *MagDown* (d) 2016 *MagUp*

Figure 31: PID reweighing histograms of $\mathrm{DLL}_{K\pi} > 10$ cut on pions.

D Background Templates

D.1 Background templates for $D_s^-\pi^+$ mass fits

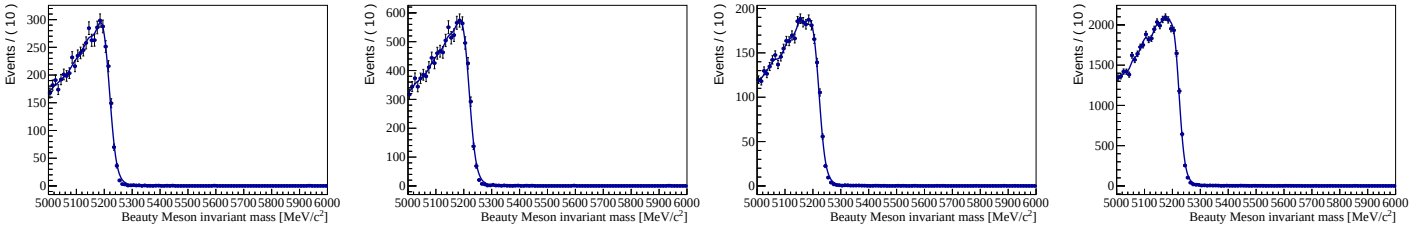

(a) 2011 (b) 2012 (c) 2015 (d) 2016

Figure 32: Background templates for $B_s^0 \to D_s^+\rho^-$.

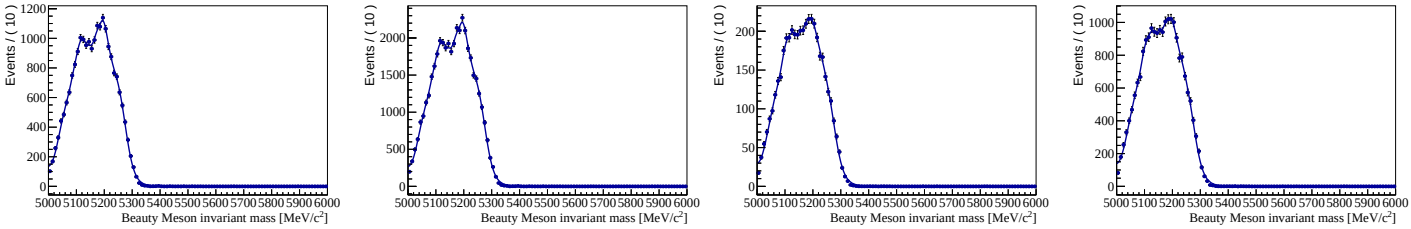

(a) 2011 (b) 2012 (c) 2015 (d) 2016

Figure 33: Background templates for $B_s^0 \to D_s^{*+}\pi^-$.

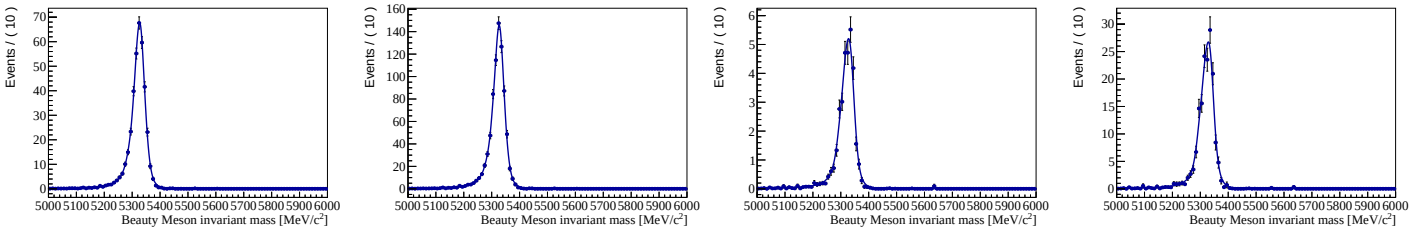

(a) 2011 (b) 2012 (c) 2015 (d) 2016

Figure 34: Background templates for $B_s^0 \to D_s^-K^+$.

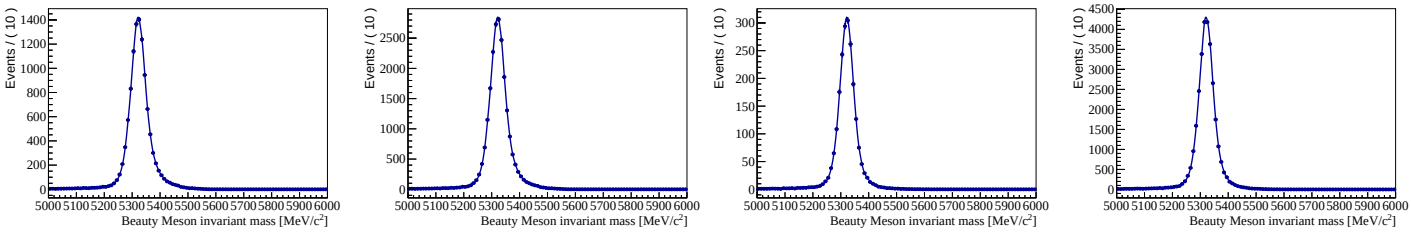

(a) 2011 (b) 2012 (c) 2015 (d) 2016

Figure 35: Background templates for $B^0 \to D^-\pi^+$.

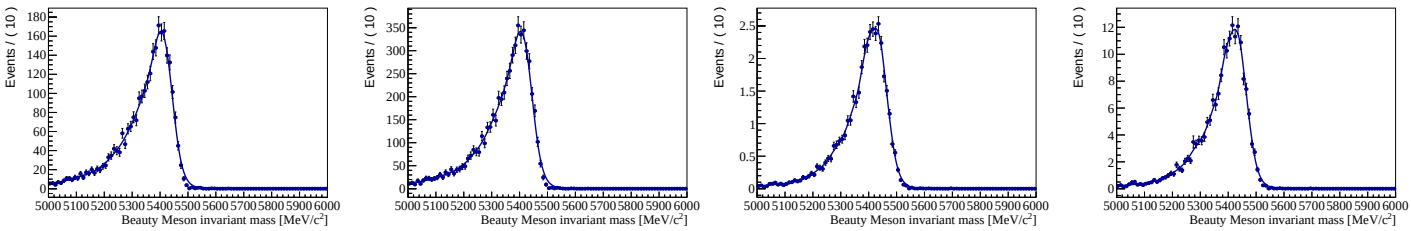

(a) 2011 (b) 2012 (c) 2015 (d) 2016

Figure 36: Background templates for $\Lambda_b^0 \to \Lambda_c^+\pi^+$.

D.2 Background templates for $K^-K^+\pi^-$ mass fits

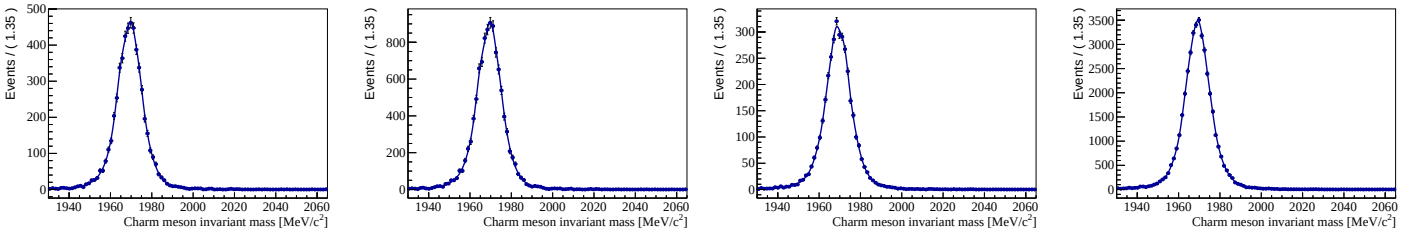

(a) 2011 (b) 2012 (c) 2015 (d) 2016

Figure 37: Background templates for $B_s^0 \to D_s^+ \rho^-$.

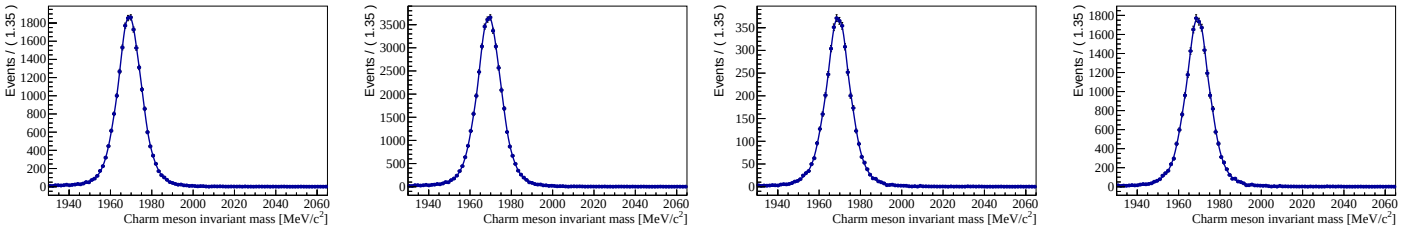

(a) 2011 (b) 2012 (c) 2015 (d) 2016

Figure 38: Background templates for $B_s^0 \to D_s^{*+}\pi^-$.

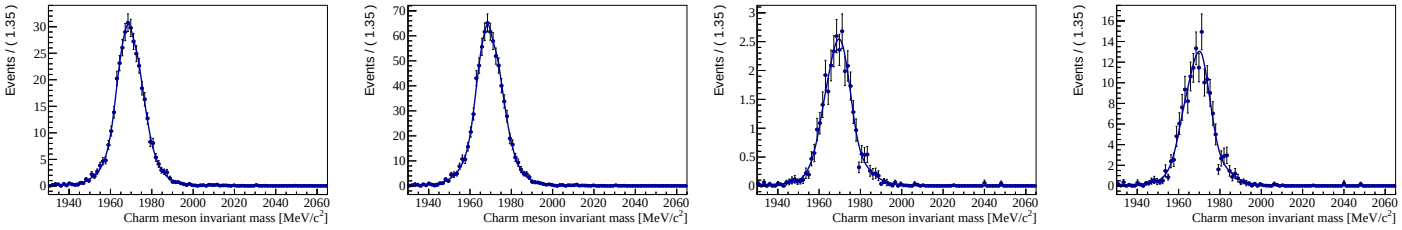

(a) 2011 (b) 2012 (c) 2015 (d) 2016

Figure 39: Background templates for $B_s^0 \to D_s^- K^+$.

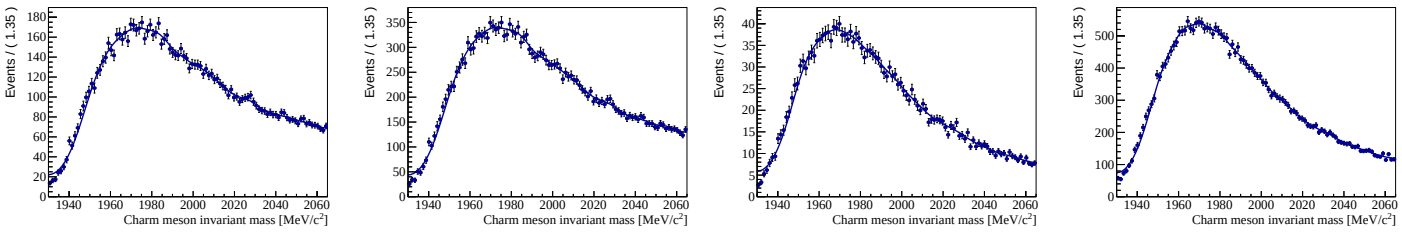

(a) 2011 (b) 2012 (c) 2015 (d) 2016

Figure 40: Background templates for $B^0 \to D^-\pi^+$.

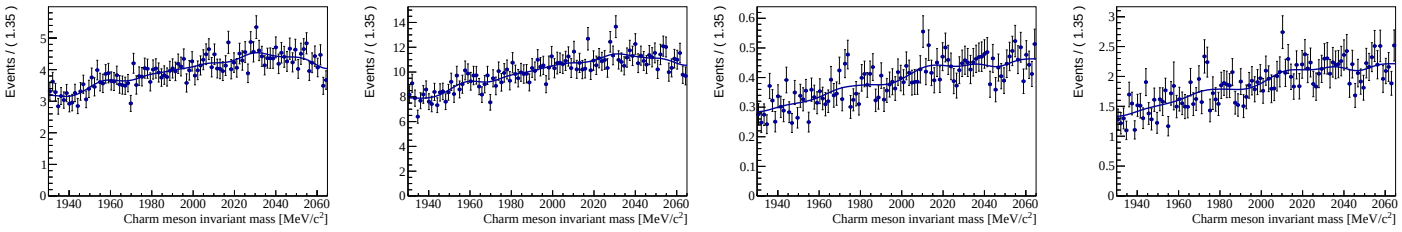

(a) 2011 (b) 2012 (c) 2015 (d) 2016

Figure 41: Background templates for $\Lambda_b^0 \to \Lambda_c^+\pi^+$.

D.3 Background templates for $D^-\pi^+$ mass fits

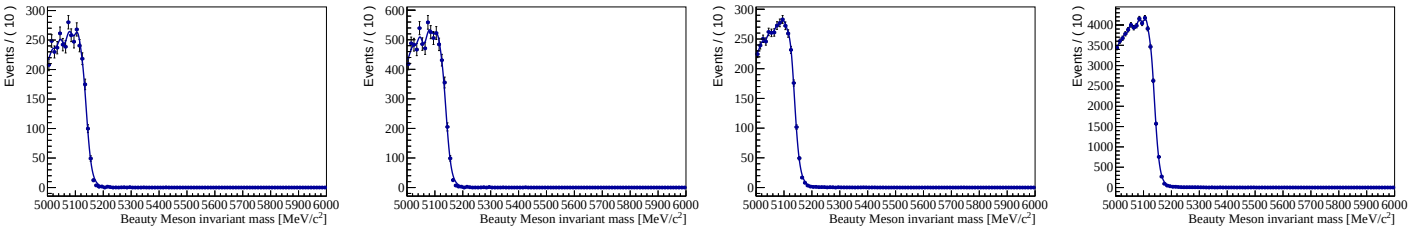

(a) 2011 (b) 2012 (c) 2015 (d) 2016

Figure 42: Background templates for $B^0 \to D^-\rho^+$.

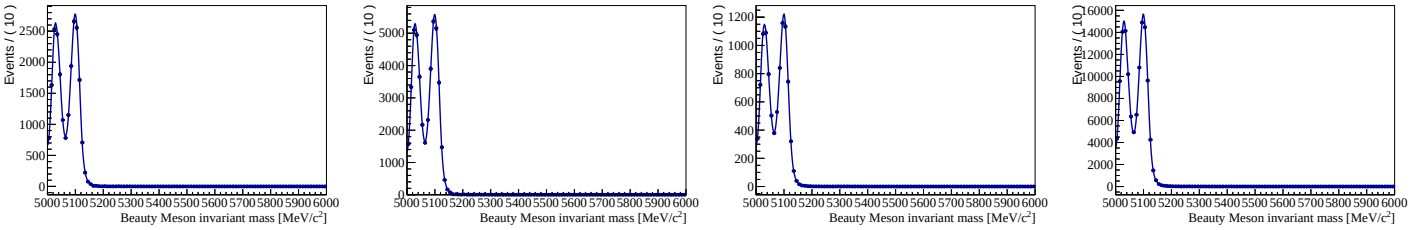

(a) 2011 (b) 2012 (c) 2015 (d) 2016

Figure 43: Background templates for $B^0 \to D^{*-}\pi^+$.

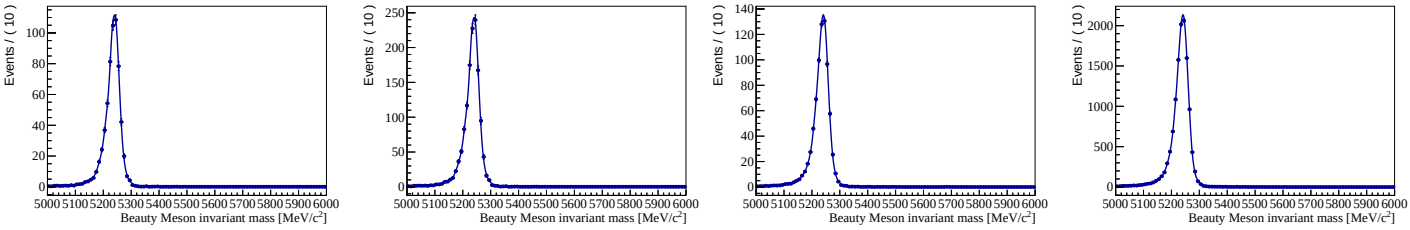

(a) 2011 (b) 2012 (c) 2015 (d) 2016

Figure 44: Background templates for $B^0 \to D^-K^+$.

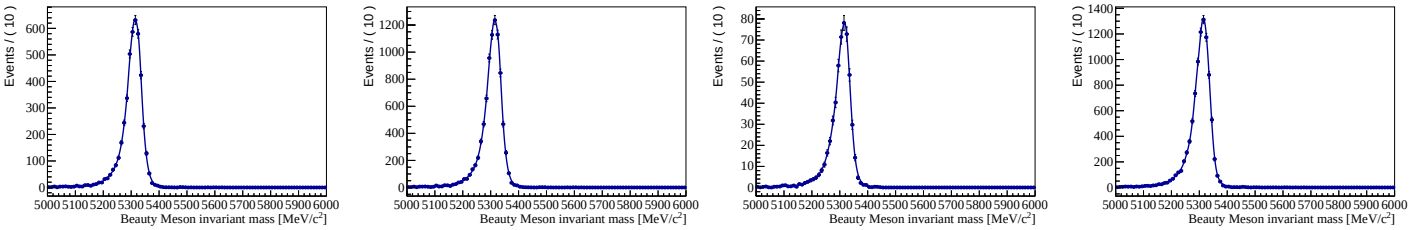

(a) 2011 (b) 2012 (c) 2015 (d) 2016

Figure 45: Background templates for $B^0 \to D^-\pi^+$.

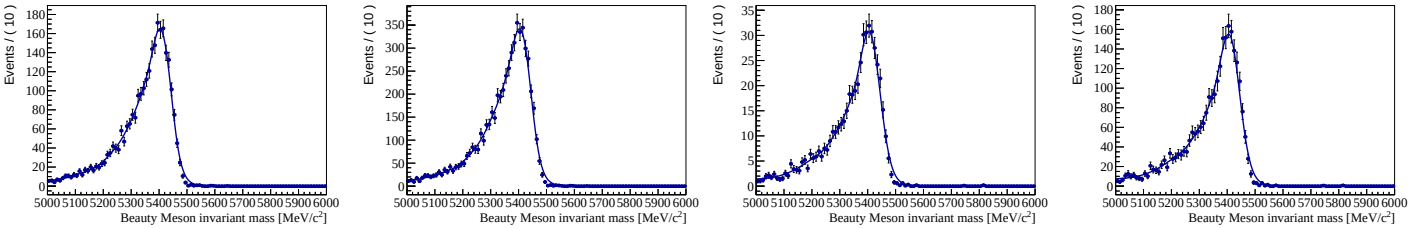

(a) 2011 (b) 2012 (c) 2015 (d) 2016

Figure 46: Background templates for $\Lambda_b^0 \to \Lambda_c^+\pi^+$.

Acknowledgements

During this Master Project I have had excellent supervision. First of all, I would like to thank my supervisor Niels Tuning for all his help. In the weekly meetings, you helped me a lot by coming up of new ideas and by discussing results. On top of that, I greatly appreciated your positivity. I also would like to thank Lennaert Bel. Thanks for always being open for questions, even when you were busy writing your PhD thesis. Also thanks for very quickly and thoroughly checking my thesis multiple times. This was very helpful. Also thanks for the adventurous car rides to CERN, during the StarterKit. Thanks to Sevda, who, as unofficial supervisor, greatly helped me to move on when I thought I was stuck during my analysis. Thank you for going through the cumbersome process of making and fixing MC nTuples, Michele. Also, I would like to thank my fellow Master Student Marinda. Doing a similar project as me, you were always nearby to ask anything. It was comforting that we were both going through the same kind of segmentation violations and other errors in `B2DXFitters` and `PIDCalib`. Thank you Mick, for your warm welcome at CERN. Your supervision during my stay at CERN helped me greatly. Also after my stay at CERN, you frequently came to my office to check how the analysis was going and to help. I want to thank Agnieszka, for helping me with `B2DXFitters` during my stay at CERN and also afterwards.
Thanks to the Nikhef LHCb group, for creating a good atmosphere to spend my Master Project. In particular, thanks to Marinda, Emma, Julius, Danny, Bo, and Robin for being great office mates.

References

[1] BaBar, B. Aubert *et al.*, *Measurement of the $B^0 \to \pi^- \ell^+ \nu$ form-factor shape and branching fraction, and determination of $|V_{ub}|$ with a loose neutrino reconstruction technique*, Phys. Rev. Lett. **98** (2007) 091801, arXiv:hep-ex/0612020.

[2] Particle Data Group, M. Tanabashi *et al.*, *Review of particle physics*, Phys. Rev. **D98** (2018) 030001.

[3] M. Beneke, *QCD factorization for exclusive, non-leptonic B decays*, arXiv preprint hep-ph/9910505 (1999).

[4] K. De Bruyn *et al.*, *Exploring $B_s \to D_s^{(*)\pm} K^\mp$ Decays in the Presence of a Sizable Width Difference $\Delta\Gamma_s$*, Nucl. Phys. **B868** (2013) 351, arXiv:1208.6463.

[5] BaBar, B. Aubert *et al.*, *Measurement of the Branching Fractions of the Rare Decays $B^0 \to D_s$ (*) + π^-, $B^0 \to D_s$ (*) + ρ^-, and $B^0 \to D_s$ (*) - $K^{(*)}$ +*, Phys. Rev. **D78** (2008) 032005, arXiv:0803.4296.

[6] Belle, A. Das *et al.*, *Measurements of Branching Fractions for $B^0 -> D_s^+ \pi^-$ and $\bar{B}^0 -> D_s^+ K^-$*, Phys. Rev. **D82** (2010) 051103, arXiv:1007.4619.

[7] LHCb, R. Aaij *et al.*, *Measurement of the $B_s^0 \to \mu^+\mu^-$ branching fraction and effective lifetime and search for $B^0 \to \mu^+\mu^-$ decays*, Phys. Rev. Lett. **118** (2017), no. 19 191801, arXiv:1703.05747.

[8] A. J. Bevan, *B Factories*, Comptes Rendus Physique **13** (2012) 145, arXiv:1202.0733.

[9] L. Evans and P. Bryant, *LHC Machine*, JINST **3** (2008), no. 08 S08001.

[10] ATLAS Collaboration, *Observation of a new particle in the search for the Standard Model Higgs boson with the ATLAS detector at the LHC*, arXiv preprint arXiv:1207.7214 (2012).

[11] CMS Collaboration, *Observation of a new boson at a mass of 125 GeV with the CMS experiment at the LHC*, Physics Letters B **716** (2012), no. 1 30.

[12] LHCb collaboration, A. A. Alves Jr. *et al.*, *The LHCb detector at the LHC*, JINST **3** (2008) S08005.

[13] LHCb collaboration, *LHCb VELO (VErtex LOcator): Technical Design Report*, CERN-LHCC-2001-011. LHCb-TDR-005.

[14] LHCb collaboration, *LHCb inner tracker: Technical Design Report*, CERN-LHCC-2002-029. LHCb-TDR-008.

[15] LHCb collaboration, *LHCb outer tracker: Technical Design Report*, CERN-LHCC-2001-024. LHCb-TDR-006.

[16] LHCb collaboration, *LHCb magnet: Technical Design Report*, CERN-LHCC-2000-007. LHCb-TDR-001.

[17] LHCb collaboration, R. Aaij *et al.*, *LHCb detector performance*, Int. J. Mod. Phys. **A30** (2015) 1530022, arXiv:1412.6352.

[18] LHCb collaboration, *LHCb RICH: Technical Design Report*, CERN-LHCC-2000-037. LHCb-TDR-003.

[19] LHCb collaboration, *LHCb calorimeters: Technical Design Report*, CERN-LHCC-2000-036. LHCb-TDR-002.

[20] LHCb collaboration, *LHCb muon system: Technical Design Report*, CERN-LHCC-2001-010. LHCb-TDR-004.

[21] LHCb collaboration, *LHCb trigger system: Technical Design Report*, CERN-LHCC-2003-031. LHCb-TDR-010.

[22] T. Head, *The LHCb trigger system*, JINST **9** (2014), no. 09 C09015.

[23] V. V. Gligorov, *A single track HLT1 trigger*, tech. rep., 2011.

[24] V. V. Gligorov, M. Williams, and C. Thomas, *The HLT inclusive B triggers*, tech. rep., 2011.

[25] M. H. Lieng, *An Inclusive ϕ Stream for the LHCb High Level Trigger, DC06 Analysis*, CERN-LHCb-2009-010. LHCb-2009-010.

[26] M. Frank *et al.*, *Deferred high level trigger in LHCb: a boost to CPU resource utilization*, J. Phys. Conf. Ser. **513** (2014) 012006.

[27] L. Breiman, J. H. Friedman, R. A. Olshen, and C. J. Stone, *Classification and regression trees*, Wadsworth international group, Belmont, California, USA, 1984.

[28] Y. Freund and R. E. Schapire, *A decision-theoretic generalization of on-line learning and an application to boosting*, J. Comput. Syst. Sci. **55** (1997) 119.

[29] LHCb collaboration, R. Aaij *et al.*, *Measurement of CP asymmetry in $B_s^0 \to D_s^{\mp} K^{\pm}$ decays*, JHEP **03** (2018) 059, arXiv:1712.07428.

[30] M. Pivk and F. R. Le Diberder, *sPlot: A statistical tool to unfold data distributions*, Nucl. Instrum. Meth. **A555** (2005) 356, arXiv:physics/0402083.

[31] T. Sjöstrand, S. Mrenna, and P. Skands, *A brief introduction to pythia 8.1*, Computer Physics Communications **178** (2008), no. 11 852.

[32] I. Belyaev *et al.*, *Handling of the generation of primary events in Gauss, the LHCb simulation framework*, J. Phys. Conf. Ser. **331** (2011) 032047.

[33] D. J. Lange, *The EvtGen particle decay simulation package*, Nucl. Instrum. Meth. **A462** (2001) 152.

[34] P. Golonka and Z. Was, *PHOTOS Monte Carlo: A precision tool for QED corrections in Z and W decays*, Eur. Phys. J. **C45** (2006) 97, arXiv:hep-ph/0506026.

[35] Geant4 collaboration, J. Allison *et al.*, *Geant4 developments and applications*, IEEE Trans. Nucl. Sci. **53** (2006) 270; Geant4 collaboration, S. Agostinelli *et al.*, *Geant4: A simulation toolkit*, Nucl. Instrum. Meth. **A506** (2003) 250.

[36] M. Clemencic *et al.*, *The LHCb simulation application, Gauss: Design, evolution and experience*, J. Phys. Conf. Ser. **331** (2011) 032023.

[37] L. Anderlini *et al.*, *The PIDCalib package*, CERN-LHCb-PUB-2016-021. LHCb-PUB-2016-021.

[38] W. Verkerke and D. P. Kirkby, *The roofit toolkit for data modeling,(2003)*, arXiv preprint physics/0306116 **111** (2016).

[39] K. Cranmer, *Kernel estimation in high-energy physics*, Computer Physics Communications **136** (2001), no. 3 198.

[40] LHCb collaboration, R. Aaij *et al.*, *Measurement of the fragmentation fraction ratio f_s/f_d and its dependence on B meson kinematics*, JHEP **04** (2013) 001, arXiv:1301.5286, f_s/f_d value updated in LHCb-CONF-2013-011.

[41] LHCb, R. Aaij *et al.*, *Study of the kinematic dependences of Λ_b^0 production in pp collisions and a measurement of the $\Lambda_b^0 \to \Lambda_c^+ \pi^-$ branching fraction*, JHEP **08** (2014) 143, arXiv:1405.6842.

[42] D. M. Santos and F. Dupertuis, *Mass distributions marginalized over per-event errors*, Nuclear Instruments and Methods in Physics Research Section A: Accelerators, Spectrometers, Detectors and Associated Equipment **764** (2014) 150.

[43] N. L. Johnson, *Systems of frequency curves generated by methods of translation*, Biometrika **36** (1949), no. 1/2 149.

[44] LHCb, R. Aaij *et al.*, *Measurement of CP violation in $B^0 \to D^{\mp}\pi^{\pm}$ decays*, arXiv:1805.03448.

[45] P. Ball and R. Zwicky, *New results on $B \to \pi, K, \eta$ decay formfactors from light-cone sum rules*, Phys. Rev. **D71** (2005) 014015, arXiv:hep-ph/0406232.

[46] P. Ball, *$|V_{ub}|$ from UTangles and $B^0 \to \pi^-\ell^+\nu$*, Phys. Lett. **B644** (2007) 38, arXiv:hep-ph/0611108.

[47] A. Bazavov *et al.*, *B- and D-meson leptonic decay constants from four-flavor lattice QCD*, arXiv:1712.09262.

[48] O. Lupton, *TISTOS problems in Run 2*, Presentation at LHCb Tuesday Meeting, 13 September, 2017.